



AN ABSTRACT OF THE DISSERTATION OF

Christopher C. Knutson for the degree of Doctor of Philosophy in Chemistry  
presented on October 20, 2011.

Title: The Chemistry and Device Applications of Amorphous Thin-Film  
Interfaces.

Abstract approved: \_\_\_\_\_

Douglas A. Keszler

Solid-state amorphous materials show amazing promise in thin-film electronics. The interface-to-bulk ratio of thin films makes interfacial chemistries of these systems of utmost importance. Thin films of amorphous metals, dielectrics and semiconductors have novel chemistries that are not only based upon their elemental constituent makeup, but also based upon the method with which the amorphous material is deposited and treated after deposition. The chemical attributes unique to amorphous, thin-film systems are defined primarily through the utilization of solution-processed aluminum oxide phosphate dielectric material and  $Zr_{40}Cu_{35}Al_{15}Ni_{10}$  metal. The chemical findings wrought via the observation of interactions between amorphous metal-dielectric systems are applied to semiconductor/insulator systems to illustrate the use of the same general chemical principles applying to diverse problems. Finally in the appendices, the systems are utilized to create extremely-thin tunneling electronic devices and optical metamaterials as well as innovative classroom material.

©Copyright by Christopher C. Knutson

October 20, 2011

All Rights Reserved

The Chemistry and Device Applications of Amorphous Thin-Film Interfaces

by

Christopher C. Knutson

A DISSERTATION

submitted to

Oregon State University

in partial fulfillment of  
the requirements for the  
degree of

Doctor of Philosophy

Presented October 20, 2011

Commencement June 2012

Doctor of Philosophy dissertation of Christopher C. Knutson presented on  
October 20, 2011.

APPROVED:

---

Major Professor, representing Chemistry

---

Chair of the Department of Chemistry

---

Dean of the Graduate School

I understand that my dissertation will become part of the permanent collection of Oregon State University libraries. My signature below authorizes release of my dissertation to any reader upon request.

---

Christopher C. Knutson, Author

## ACKNOWLEDGEMENTS

I would not be here were it not for my parents: Daph and Mary Knutson. My father gave me a sense of humor that perseveres through challenges, and a keen mechanical insight that has allowed me to combat unruly machinery. He showed me that refinement and hard work make most things fall within my reach. He was never a man of many words with me, but the experience of growth I have undergone during my progression through my thesis has brought us closer together by giving me a strong sense of accomplishment and a strong sense that many words do not necessarily mean as much as a little hard work.

My mother is my living example of strong organization and execution of responsibilities. She taught me to be considerate of others, and open to new ideas. Many of my collaborations would not have been possible had my mother not taught me to be open and flexible to the input of others, as well as stick up for my own when I can clearly back it up. Her strong sense of her duty in providing our society with quality movement forward will forever drive my endeavors, and her strength will forever inspire me.

My brother David taught me the patience to deal with input from others positively, and has offered me boundless morale. His sense of honor and duty carry through to me. Oddly, even though he does not think so, his ability to do math involving tessellation and repetition has been incredibly inspirational in my studies of crystalline materials. Although he uses his keen understanding of patterns to produce fine whips, the math

and organization used are ever present in my life in other arenas. Serendipitously, both of our methods of generating tessellations are apt at moving wave forms efficiently.

Some of my coworkers deserve mention for all of the help they have provided me. My predecessors Jeremy Anderson, Kai Jiang, Jason Stowers and Heather Platt have all offered me a great deal of guidance and help in the lab. Stephen Meyers has been especially helpful in my studies. His straightforward, no-nonsense method to answering questions has been specifically refreshing. Without their strong strides forward, I would not have had such a reliable base to stand on.

I regard a few of my coworkers as close personal friends, among them are Alan Telecky and Wei Wang. Alan has been inspirational in his demonstration of how to balance a burgeoning family, work and play. I look up to his ability to lead a balanced, healthy and fun life; plus, he is a heck of a left-fielder for the softball team. Wei is a special character whose willingness to adapt to a new culture and a new land have taught me countless lessons about having a positive attitude in a difficult and ever-changing world. Our conversations about differences have shown me how much I honor our similarities. I think I enjoy the way that Wei has managed to keep a child's eye throughout the development of his adult intellect. I have immensely enjoyed the unconventional learning experiences we have shared together, and look forward to lifelong friendships with them.

Cross-departmental collaboration has also been incredibly important to my graduate career, the most important of which being collaboration with the electrical engineers

from the group of Dr. J. F. Wager. Dr. Wager has shown me that engineers do chemistry and has taught me to teach chemistry to engineers by giving me the lexicon to do so. I now know that most of what I observe as chemical-mixing phenomena is known to engineers as non-ideality. Dr. Wager's students Rick Presley and Eric Sundholm have offered me both friendship and assistance in countless experiments; but one of his students has stood out as especially integral to my success in these studies. Bill Cowell is: a friend, a scholar, an engineer, a chieftain and a conundrum. He is often my muse, and regularly amusing; quite often we muse about how to best design our systems. Bill has shown me countless life lessons, mostly about being OCD and open-minded simultaneously. While the last sentence seems counterintuitive, because it is, somehow Bill manages to strike a balance. His insights are highly valued.

This work would not be possible if it were not for the strong support of Douglas Keszler, whose unending support and decasyllabic utterances have contained more logical reason than I may ever provide the scientific world. It has been a pleasure to work under this gentleman, learn from his chemical expertise and become a scientist through his tutelage. Dr. Keszler has taught me a true definition of trust. He has allowed me to apply myself largely as I see fit while simultaneously offering me continuous opportunity. I hope to mirror his dignity and forethought in the practice of chemistry in my future as a chemist. I'm only truly starting to understand the underlying genius beneath his research; but I have a wonderful understanding of those who research beneath him. I am glad to work for this man because I agree with the

fundamental insights driving the directions of his research, and so it has been a pleasure to come to work for him.

Finally, Erica Hanson has become integral to the maintenance of my sanity. Sanity has been crucial to this entire process, making her a crux pin of this machine. I cannot thank her enough for her level approach to this endeavor.

## CONTRIBUTION OF AUTHORS

Master E. William Cowell III is responsible for a large amount of electronic measurement in the cases of tunneling devices, and he is a major contributor to all theory herein. Dr. William Stickle of Hewlett Packard is responsible for all X-ray photoelectron spectroscopy. Ronald Kelley, Randy Burgess, and Peter Eschbach are responsible for the TEM membrane preparation and imaging in a majority of Chapters 2 and 3. Alan Telecky prepared and dispensed the HafSO<sub>x</sub> solution in Chapter 3. Passivated ZTSO/ZTO devices were produced and electronically tested by Rick Presley and Bao Yeh for Chapter 4. Ellipsometric characterization was carried out by Ram Ravichandran. Robert Kykyneshi aided in the execution and evaluation of the UV-visible spectroscopic measurements in Chapter 4. The modeling of passivation in Chapter 4 was carried out by J.F. Wager and John Robertson. Atomic layer depositions of films were carried out by Nasir Alimardani in Appendix 1.1. Optical reflection measurements for the metamaterials were carried out by Dr. Brady Gibbons, and modeling was done by Nick Kuhta in Appendix A.3. Matti Alemayehu, John Evan Davis, Milton Jackson, Brian Lessig, Logan Smith, and Jon David Sumega all carried out depositions and testing on devices and carried out a great deal of writing as well as revision of the manuscript in Appendix 2.1. David Johnson provided editing, funding and inspiration for both projects in Appendix 2. Douglas Keszler has been instrumental in all work herein.

## TABLE OF CONTENTS

	<u>Page</u>
<b>CHAPTER 1: INTRODUCTION TO AMORPHOUS MATERIALS IN THE THIN FILM.....</b>	<b>1</b>
Introduction to Amorphous Materials.....	2
Amorphous Oxides.....	3
Amorphous Oxide Insulators.....	5
Amorphous Oxide Semiconductors.....	6
Aqueous Solution Processing.....	8
References.....	9
 <b>CHAPTER 2: ORGANIZATIONAL CHEMICAL EFFECTS AND REAGENT LIMITATION OF REACTIONS IN AMORPHOUS METAL AND SOLUTION-PROCESSED, AMORPHOUS OXIDE THIN FILMS.....</b>	 <b>12</b>
Introduction.....	13
Experimental.....	14
Results and Discussion.....	16
Conclusions.....	30
References.....	33
 <b>CHAPTER 3: INTERFACE CHEMISTRIES IN NANOLAMINATES OF AMORPHOUS METALS AND AMORPHOUS OXIDES.....</b>	 <b>35</b>
Introduction.....	36
Experimental.....	42

## TABLE OF CONTENTS (Continued)

	<u>Page</u>
Results and Discussion.....	44
Conclusions.....	66
References.....	68
<b>CHAPTER 4: SPUTTER-COATED PASSIVATION OF ZINC TIN OXIDE.....</b>	<b>71</b>
Introduction.....	72
Experimental.....	87
Results and Discussion.....	91
Conclusions.....	102
References.....	103
<b>CONCLUSIONS.....</b>	<b>109</b>
<b>BIBLIOGRAPHY.....</b>	<b>110</b>
<b>APPENDICES.....</b>	<b>118</b>
Appendix A: Applications of Amorphous, Nanolaminated Materials...	119
A.1. Amorphous Metal/Oxide Nanolaminate.....	119
A.2. Advancing MIM Electronics: Amorphous Metal Electrodes.....	130
A.3. Engineering Anisotropic Dielectric Response Through Amorphous Laminate Structures.....	148

## TABLE OF CONTENTS (Continued)

	<u>Page</u>
Appendix B: Educational Outreach.....	173
B.1. Tunable dielectric thin films by aqueous, inorganic solution-based processing.....	173
B.2. A State-of-the-Art, Laboratory-Intensive, Guided-Inquiry- Based Graduate Research Course.....	187

## LIST OF FIGURES

<u>Figure</u>	<u>Page</u>
1.1	(a) Electron diffraction pattern for single-crystal silicon..... 3
2.1	(a) Low-resolution TEM image of a ZCAN/AlPO laminate..... 17
2.2	(a) XPS depth profile (using Ar <sup>+</sup> ) of oxidized material in 300°-annealed stack structure processed exactly the same as the structure in Figure 2.1(a)..... 20
2.3	(a) Low-resolution TEM image detailing a laminate with ZCAN depositions carried out as listed..... 24
2.4	Electron-beam annealed sample showing pockets of low density caused by heating and E-beam reduction of water present in the TEM membranes..... 26
2.5	(a) C <sub>60</sub> XPS depth profiles showing concentrations of oxidized species..... 28
3.1	(a)TEM micrograph of nanolaminated stucture with four layers of ZrCuNiAl amorphous metal separated by three layers of AlPO..... 45
3.2	(a) XPS depth profile of neutrally-charged metals from nanolaminated stucture with four bilayers of AlPO-topped ZrCuNiAl, topped with a schematic diagram labeling the component layers..... 47
3.3	(a)TEM micrograph of Cu-AlPO-ZrCuAlNi laminate with the direction of the XPS profile indicated on the image..... 51
3.4	(a) XPS profile of ZrCuNiAl deposited onto high-temperature annealed AlPO at 30 W..... 53
3.5	Labeled TEM micrograph of ZrCuAlNi-AlPO laminate utilizing AlPO precursors with different Al:P ratios with overlaid intensity profile of phosphate, phosphide and aluminum metal arranged for intuitive spatial overlap..... 54

## LIST OF FIGURES (Continued)

<u>Figure</u>		<u>Page</u>
3.6	(a) Labeled schematic diagram of ZrCuAlNi-AlPO-TiAl <sub>3</sub> laminate with inset electron diffraction taken from section of film displayed.....	56
3.7	(a)XPS depth profile of 100-nm HafSO <sub>x</sub> film.....	60
3.8	(a)Graph of Zirconium-photoelectron binding energies resolved from laminated structure.....	61
3.9	(a)TEM micrograph of ZrCuAlNi-ZircSO <sub>x</sub> laminated structure with XPS depth-profile overlay showing all oxidized metals present, as well as oxide and sulfide concentrations.....	62
3.10	(a)TEM micrograph of ZrCuAlNi-HafSO <sub>x</sub> laminated structure with XPS depth-profile overlay showing all oxidized metals present, as well as oxide and sulfide concentrations.....	64
4.1	Equilibrium energy band diagrams illustrating an undesirable passivation scheme.....	75
4.2	Equilibrium energy band diagrams illustrating a desirable passivation scheme.....	79
4.3	(Left) Low-resolution TEM image demonstrating an entire device stack.....	91
4.4	X-ray photoelectron spectroscopic depth profiles of atomic composition for: (a) an as-deposited ZTSO film in the device stack shown in 4.3. (b) a 400 °C annealed ZTSO device stack as shown in 4.3.....	92
4.5	X-ray diffraction patterns of a 200 nm film of ZTSO heated to various listed temperatures (in Celsius) with calculated SnO <sub>2</sub> (Cassiterite) and ZnO (Zincite) patterns included for reference.....	93
4.6	Ultraviolet and optical transmission and reflection data for 1.2 μm thick film of ZTSO upon 1 mm thick fused silica.....	94
4.7	Indirect band gap analysis of 1.20 micron film of ZTSO deposited upon fused silica.....	95

## LIST OF FIGURES (Continued)

4.8	Index of refraction (n) and extinction coefficient (k) for 100-nm ZTSO thin-film annealed to 400 °C.....	96
4.9	Plot of $(\alpha E)^{1/2}$ vs. photon energy showing regression from which the band gap is estimated using ellipsometry.....	97
4.10	Logarithm of the drain current versus the gate-source voltage, i.e., $\log(I_D) - V_{GS}$ transfer curve and average mobility curve of a ZTO TFT (i.e. the ZTO surface is exposed to air).....	98
4.11	Logarithm of the drain current versus the gate-source voltage, i.e., $\log(I_D) - V_{GS}$ transfer curve and average mobility measurements of post-passivated TFTs.....	99
4.12	Logarithm of the drain current versus the gate-source voltage, i.e., $\log(I_D) - V_{GS}$ transfer curve and average mobility measurements ZTSO capped, post 400 °C annealed TFTs.....	100
4.13	Logarithm of the drain current versus the gate-source voltage, i.e., $\log(I_D) - V_{GS}$ transfer curve and average mobility measurements of post-passivated, post 400 °C annealed, PECVD SiO <sub>2</sub> coated TFTs.....	101

## LIST OF TABLES

<u>Table</u>		<u>Page</u>
4.1	Energy band gap ( $E_G$ ), electron affinity ( $\chi$ ), charge neutrality level ( $\Phi_{\text{CNL}}$ ), and Gibbs free energy of formation (kcal/gm-atom) for selected oxides. $\chi$ and $\Phi_{\text{CNL}}$ are referenced to the vacuum level.....	106
4.2	High-frequency relative dielectric constant ( $\epsilon_{\infty R}$ ), interface parameter for a surface (S), and surface state density ( $D_{\text{SS}}$ ) for selected semiconductors and insulators.....	107
4.3	Interface parameter ( $S_{\text{PS}}$ ), interface dipole voltage ( $\Delta_{\text{PS}}$ ), and interface state density ( $D_{\text{PS}}$ ) for selected semiconductor/passivation layer combinations.....	108

## APPENDIX FIGURES

<u>Figure</u>	<u>Page</u>
A.1.1 (a) TEM micrograph of an AlPO/AMMF nanolaminate comprised of four 20 nm AlPO/AMMF bilayers.....	123
A.1.2 HAADF image of lower 2 bilayers.....	124
A.1.3 (a) XPS depth profile of Zr, O, Cu, Al, and Ni taken through the nanolaminate shown in Figure A.1.1b.....	126
A.1.4 Cover Art detailing XPS profile of Zr(0) and Zr(IV) in green and yellow respectively with inset electron diffraction displaying the amorphousness of the system.....	129
A.2.1 a) An AFM image of the surface of a 100-nm ZrCuAlNi amorphous metal film.....	134
A.2.2 TEM image of a symmetric MIM diode fabricated with M1 = ZrCuAlNi amorphous metal film, I = 10 nm Al <sub>2</sub> O <sub>3</sub> , M2 = ZrCuAlNi amorphous metal film.....	136
A.2.3 Current-voltage ( <i>I-V</i> ) curves of asymmetric MIM diodes fabricated with M1 = ZrCuAlNi amorphous metal film, I = Al <sub>2</sub> O <sub>3</sub> , and M2 = Al.....	140
A.2.4 . <i>I-V</i> curves for MIM diodes with M1 = ZrCuAlNi, M2 = Al, and I = ZrO <sub>2</sub> or AlPO + ZrO <sub>2</sub> .....	143
A.3.1 Graphical representation of the mathematical dispersion equations and resulting dispersion of incident light incident on (a) spherical isotropic materials, (b) elliptical anisotropic materials, and (c) hyperbolic anisotropic materials.....	153
A.3.2 Materials analysis data of an anisotropic, dispersion, laminate material fabricated with TiAl <sub>3</sub> /AlPO bilayers.....	154

## APPENDIX FIGURES (Continued)

<u>Figure</u>	<u>Page</u>
A.3.3	TEM micrograph of ZrCuAlNi/AlPO laminate illustrating lower limit of amorphous metal layer thickness..... 155
A.3.4	Real components of the complex, isotropic amorphous metal and AlPO dielectric responses along with effective, anisotropic dielectric responses of laminate (a) ZrCuAlNi/AlPO and (b) TiAl <sub>3</sub> structures..... 159
A.3.5	Normalized measured to modeled error versus metal/dielectric ratio of reflectance data collected using T <sub>M</sub> polarized light with laminates fabricated with bilayers comprised of (a) ZrCuAlNi/AlPO and (b) TiAl <sub>3</sub> /AlPO ..... 163
A.3.6	XPS depth profiles taken through amorphous metal/oxide laminate structures..... 164
B.1.1	Schematic process flow for production of capacitors via aqueous solution-processing..... 178
B.1.2	(a) Experimental XRR data collected on a HafSO <sub>x</sub> film containing four layers (coats)..... 180
B.1.3	Cross-sectional SEM images of AlPO/HafSO <sub>x</sub> thin film device..... 181
B.1.4	Relative dielectric constant, k, as a function of the HafSO <sub>x</sub> thickness fraction..... 184

The Chemistry and Device Applications of  
Amorphous Thin-Film Interfaces

Chapter 1

INTRODUCTION TO AMORPHOUS MATERIALS IN THE THIN  
FILM

## **Introduction to Amorphous Materials**

Amorphous materials are rather common because amorphousness simply means: “without a clearly defined shape or order.” Amorphous can also be used as a pejorative to mean disorganized or vague when used in regards to people. Some people may argue that having no defined shape or order is a virtue. Bruce Lee argued that we should be like water for the fact that water is amorphous. Amorphous materials tend toward accepting shapes, but in doing so amorphous materials have great power.

To address the source of this power, we simply need to investigate water. In its standard state, water is amorphous. Water has no defined shapes because the molecules within it can relatively freely move about each other. When energy is removed from water, and it freezes, it no longer acts as a liquid. In solid water, the molecules organize themselves into brilliantly symmetric patterns. These highly symmetric organizations of atoms in the solid state are called crystals. When gaseous water is turned to a solid, the process forms snowflakes of crystalline water. In snowflakes, the symmetries of atomic organization can even be viewed by basic optical magnification.

In fact, the great majority of materials act similarly to water in this regard. Most materials are crystalline as solids. It is rather rare to find materials that are disorganized in the solid form, even though amorphous solids are incredibly historically pertinent. Figure 1.1 illustrates what happens when electrons are rapidly propelled through thin membranes of crystalline silicon in Figure 1.1a and through an amorphous oxide

material in Figure 1.1b. The organized points present in the crystalline figure arise from the highly symmetric diffraction events that occur when electrons are repelled by atoms within the material. The lack of an organized pattern in Figure 1.1b indicates the overall lack of organization in the material. Arguably, amorphous solids containing oxygen, generally called glasses, are the most historically pertinent.

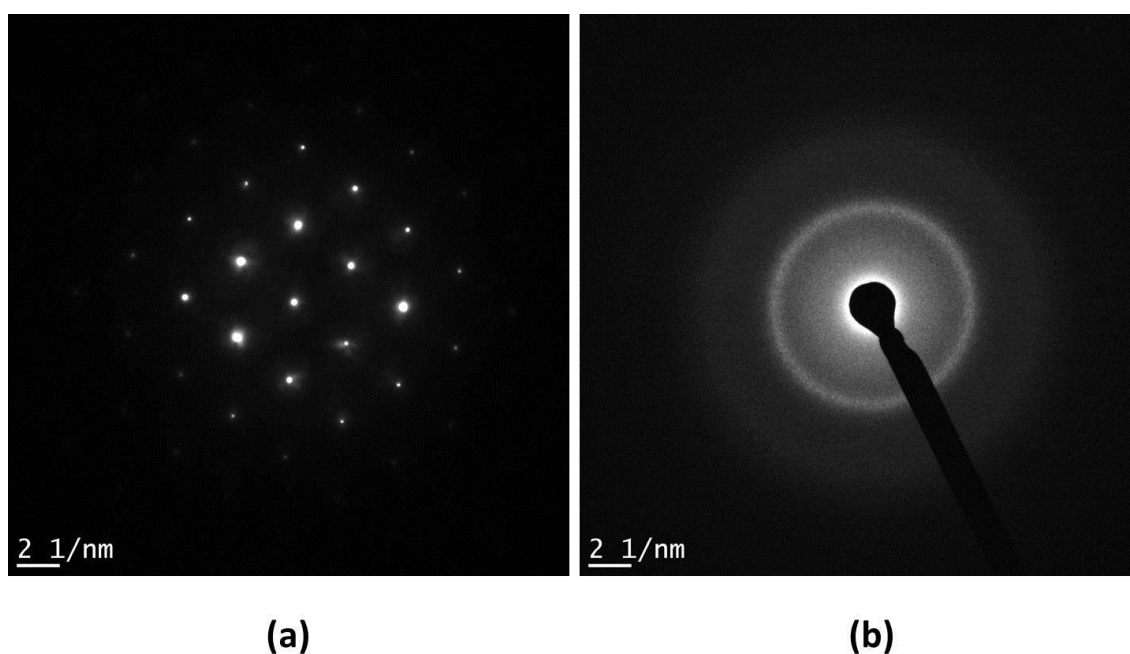


Figure 1.1: (a) Electron diffraction pattern for single-crystal silicon. (b) Electron diffraction taken from amorphous SiO<sub>2</sub>.

### **Amorphous Oxides**

Humans have a long history with amorphous-oxide solids. Arguably human history begins around the time that people first started using stone tools; and obsidian (amorphous SiO<sub>2</sub> doped with Fe<sub>3</sub>O<sub>4</sub> and MgO) was the material of choice for the best

stone-age, tools. Obsidian a volcanic glass, and is first reported by Pliny the Elder in his famous work Naturalis Historia and has been shown through archaeology to be heavily present in the Mediterranean as well as eastern and northern Africa.<sup>1</sup> The material has amazing properties that come from the fact that the atoms within it are amorphous.

Obsidian is capable of incredibly sharp edges and smooth lines. The lack of a crystal structure removes the ability of the material to preferentially deform in symmetrically favorable directions; this is to say that the atoms don't know where to move when under pressure. This allows the material to be rather hard, but it also allows the material to be chipped into something with an atomically sharp edge.

Obsidian deposits are located near volcanoes due to the large amount of heat present in volcanoes, however the production of pure-black obsidian glass requires rapid cooling. If the  $\text{SiO}_2$  is cooled too slowly, crystallites of  $\text{SiO}_2$  can collaboratively grow into snowflake-like structures generating "snowflake obsidian."

Silicon dioxide glass saw refinement in early northeastern Africa, where the first Egyptian glassworks show human understanding of the preparation and processing of melts very similar to what we now consider glass.<sup>2</sup> Glass has been a mainstay of human culture since. We use amorphous oxide glasses in everything from spectacles to windows and cookware. Small compositional changes in the glass can dominate properties such as the refractive index (lens and window applications), as well as color inclusion.

One common misconception about glasses is that they flow. The misconception originates with the observation that old windows are thicker at the bottom than at the top. Old windows do tend to be thicker at the bottom than at the top, however this fact is due to the methods used to process glass for windows from antiquity until the mid-twentieth century: glass blowing.<sup>3</sup> If glasses did flow, obsidian would not be able to hold edges from antiquity, and modern electronics relying upon glasses would not be possible.

### **Amorphous oxide insulators**

While oxygen and silicon are the two most abundant elements on the Earth's crust respectively, man has had few ways to separate them until the invention and use of electrochemical separation for this purpose in the 1850s and later.<sup>4</sup> Notable findings about silicon were that it did not react like a metal or a nonmetal when probed with electricity and heat. It was a novel class of material, a semiconductor. Silicon was found to be useful in switching, however it wasn't until the end of 1957 when physicist Jean Hoerni theorized about how to make a stack of silicon and silicon dioxide glass that modern electronics were born.<sup>5</sup> (An interesting note, this theory predates the generation of a flat-glass process for windows by over ten years.<sup>6</sup>)

While silicon is semiconducting, silicon dioxide ( $\text{SiO}_2$ ) does not conduct electricity well at all. Oxygen has a ravenous appetite for the electrons of silicon, hence the abundance of  $\text{SiO}_2$  in the Earth's crust is higher than any other elemental combination. The ability of oxygen to take and hold the electrons of silicon makes the material

nonconductive to electricity, therefore  $\text{SiO}_2$  is an insulator. The magical aspect of silicon is that its crystals will grow amorphous  $\text{SiO}_2$  with little more than water and thermal input. Hoerni realized this fact, and made an empire based upon it.

In the time since Hoerni the field of amorphous materials shown to be effective dielectrics has grown to include other oxide materials, few stand up to  $\text{SiO}_2$ .

It has been a mission of our group to move past the dependence on silicon for active electronic materials. We accomplish this by searching out new amorphous materials that do not rely on a silicon substructure for their manufacture. To this end, many of the studies herein revolve around generating amorphous materials that can function regardless of substrate or backing. These ends have been achieved to a large degree, as will be discussed later in the Aqueous Solution Processing section.

### **Amorphous Oxide Semiconductors**

Not all elements bond as tightly to oxygen as silicon. zinc, tin, and indium have propensities to retain some loosely-held electrons, making them ideal candidates for semiconductor materials. Previous research has shown that with physical vapor deposition techniques that viable semiconductor devices may be produced on substrates other than silicon,<sup>7-9</sup> and even make transparent devices.<sup>10</sup> Chemistry in these systems, specifically oxidative sensitivity, dominates their long-term behavior and makes them a prime field of study for the chemist. A great deal of my work has been to find methods of preventing damage to these novel materials during the finishing stages of circuit production and usage as will be discussed in Chapter 4.

## Amorphous Metals

Recent developments in metallurgical heating and rapid cooling have allowed for an entirely novel field to emerge, the field of amorphous metals. The first bulk amorphous sample of metal was reported to from an alloy of gold and silicon in 1960,<sup>11</sup> and since the field has grown substantially. There has done a great deal of work developing amorphous metals further than preceding scientists by adding substantial amounts of other metals such as titanium and zirconium to the mixes. A spin-off company from Caltech named Liquid Metal<sup>12</sup> now sells tailor-made metallic blends, although their flagship product was Vitreloy 1, an alloy with the composition:

$Zr_{41.2}Be_{22.5}Ti_{13.8}Cu_{12.5}Ni_{10}$ . Vitreloy is of historic importance because it is the first-reported slow-cooling bulk metallic glass.

Other scientists are expanding the field as well.<sup>13,14</sup> The field of amorphous metal study has exploded with fervor and new materials recently. Multiple applications have been also been found for amorphous metals in anything from golf drivers<sup>12</sup> to hydrogen separation,<sup>15-17</sup> and even magnetic sensing.<sup>14</sup>

Even more inspirational work is being done by people developing new methods to measure and model amorphous materials by utilizing amorphous metals. X-ray and neutron PDF are showing themselves to be at the forefront of amorphous metal study, with wonderful contributions in which local structures are deduced through total scattering.<sup>18</sup> While the bulk properties of bulk metallic glasses are incredibly interesting, for the purpose of this contribution, thin-film applications of amorphous

metals will be the primary concern. Amorphous metals have been shown useful as gates<sup>19</sup> and even electrodes<sup>20</sup> in next-generation devices. A great deal of this work investigates exactly how much chemistry these metals do when incorporated into planar, stack structures pertinent to devices.

### **Aqueous Solution Processing**

It was previously mentioned that our goals are to move away from processing methods common to silicon. I believe that the silicon-processing industry is generally stuck in a processing paradigm based upon Hoerni's work. The Keszler group is working to redefine the paradigm of electronics processing to include aqueous solution processing of inorganic materials.<sup>21</sup> Aqueous processing is superior to conventional processing methods in that it removes the energy taken by a vacuum system from the processing resource input while maximizing the ability to reclaim unused material from an excess pool of liquid. One need not lose the vast majority of one's material simply by depositing while using this method, whereas a vacuum system does not offer that option.

Before I started studying the aqueous processing of inorganic solutions, I was not aware of the balance that needs to be stricken to do so. I have done a great deal of teaching of general chemistry in my time at Oregon State University, and I now understand what a disservice we provide to the students by teaching them water's solubility "Rules."

Water makes a relatively ideal solvent for oxide materials. It is ideal in that it has low molecular volume, and causes little disturbance to morphology as it is excreted from the film during heating. Water also has a surface tension that allows for even dispersion of nanoparticulate matter, offering angstrom-smooth thin-film interfaces.<sup>22-24</sup> Water also offers the ability to complete Prompt Inorganic Condensation (PIC) reactions in which hydroxyl ligands may be promptly reacted away to produce a dense, oxide film.<sup>21</sup>

The Keszler group has been very successful in broadening the number of oxide dielectric materials that may be processed utilizing aqueous solution to include Zr<sup>22</sup>, Hf<sup>22,25</sup>, Ti<sup>26</sup>, and Al<sup>24</sup>. Semiconducting oxide materials have been generated, including: pure zinc oxide<sup>27</sup> and indium gallium zinc oxide (IGZO).<sup>28</sup> Further investigation into the abilities of aqueous solutions to aid in the production of thin-film devices is warranted, and I look forward to the future of this science.

**References:**

- (1) Dixon, J. E.; Cann, J. R.; Renfrew, C. *Sci. Am.* **218**, 38-46.
- (2) Nicholson, P. T.; Shaw, I. *Ancient Egyptian materials and technology*; Cambridge University Press: Cambridge, UK, 2000.
- (3) Brill, R. H. Corning Museum of Glass | Articles | Does Glass Flow?  
<http://www.cmog.org/dynamic.aspx?id=294#.TpZoJ7JliXs> (accessed Oct 13, 2011).
- (4) Deville, H. S. C. *Ann. Chim. Phys.* **1854**, *43*, 31-33.
- (5) Riordan, M. The Silicon Dioxide Solution - IEEE Spectrum  
<http://spectrum.ieee.org/semiconductors/design/the-silicon-dioxide-solution> (accessed Oct 13, 2011).
- (6) Pilkington, L. A. B. *Proc. R. Soc. Lond. A* **1969**, *314*, 1-25.
- (7) Jackson, W. B.; Hoffman, R. L.; Herman, G. S. *Appl. Phys. Lett.* **2005**, *87*, 193503.
- (8) Nomura, K.; Ohta, H.; Takagi, A.; Kamiya, T.; Hirano, M.; Hosono, H. *Nature* **2004**, *432*, 488-492.
- (9) Hoffman, R. L. *Solid-State Electron.* **2006**, *50*, 784-787.
- (10) Chiang, H. Q.; Wager, J. F.; Hoffman, R. L.; Jeong, J.; Keszler, D. A. *Applied Physics Letters* **2005**, *86*, 012503.
- (11) Klement, W.; Willens, R. H.; Duwez, P. *Nature* **1960**, *187*, 869-870.
- (12) Liquidmetal - Amorphous Metal Alloys - Product Design & Development  
<http://www.liquidmetal.com/> (accessed Oct 13, 2011).
- (13) Greer, A. L.; Ma, E. *MRS Bull.* **2007**, *32*, 611-619.
- (14) Inoue, A.; Nishiyama, N. *MRS Bull.* **2007**, *32*, 651-658.
- (15) Dolan, M.; Dave, N.; Morpeth, L.; Donelson, R.; Liang, D.; Kellam, M.; Song, S. *J. Membr. Sci.* **2009**, *326*, 549-555.
- (16) Hara, S.; Sakaki, K.; Itoh, N.; Kimura, H. M.; Asami, K.; Inoue, A. *J. Membr. Sci.* **2000**, *164*, 289-294.

- (17) Tawarayama, H.; Hosono, H.; Yamaura, S.-ichi; Zhang, W.; Inoue, A. *Chem. Lett.* **2009**, *38*, 502.
- (18) Fan, C.; Liaw, P. K.; Wilson, T. W.; Dmowski, W.; Choo, H.; Liu, C. T.; Richardson, J. W.; Proffen, T. *Appl. Phys. Lett.* **2006**, *89*, 111905.
- (19) Grubbs, M.; Zhang, X.; Deal, M.; Nishi, Y.; Clemens, B. M. *Appl. Phys. Lett.* **2010**, *97*, 223505.
- (20) Cowell, E. W.; Alimardani, N.; Knutson, C. C.; Conley, J. F.; Keszler, D. A.; Gibbons, B. J.; Wager, J. F. *Adv. Mater.* **2011**, *23*, 74-78.
- (21) Mitzi, D. B. *Solution Processing of Inorganic Materials*; Wiley: Hoboken, New Jersey, 2009.
- (22) Anderson, J. T.; Munsee, C. L.; Hung, C. M.; Phung, T. M.; Herman, G. S.; Johnson, D. C.; Wager, J. F.; Keszler, D. A. *Adv. Funct. Mater.* **2007**, *17*, 2117-2124.
- (23) Cowell III, E. W.; Knutson, C. C.; Wager, J. F.; Keszler, D. A. *ACS* **2010**, *2*, 1811-1813.
- (24) Meyers, S. T.; Anderson, J. T.; Hong, D.; Hung, C. M.; Wager, J. F.; Keszler, D. A. *Chem. Mater.* **2007**, *19*, 4023-4029.
- (25) Jiang, K.; Anderson, J. T.; Hoshino, K.; Li, D.; Wager, J. F.; Keszler, D. A. *Chem. Mater.* **2011**, *23*, 945-952.
- (26) Jiang, K.; Zakutayev, A.; Stowers, J.; Anderson, M. D.; Tate, J.; McIntyre, D. H.; Johnson, D. C.; Keszler, D. A. *Solid State Sci.* **2009**, *11*, 1692-1699.
- (27) Meyers, S. T.; Anderson, J. T.; Hung, C. M.; Thompson, J.; Wager, J. F.; Keszler, D. A. *J. Am. Chem. Soc.* **2008**, *130*, 17603-17609.
- (28) Mensinger, Z. L.; Gatlin, J. T.; Meyers, S. T.; Zakharov, L. N.; Keszler, D. A.; Johnson, D. W. *Angew. Chem.* **2008**, *120*, 9626-9628.

## Chapter 2

# ORGANIZATIONAL CHEMICAL EFFECTS AND REAGENT LIMITATION OF REACTIONS IN AMORPHOUS METAL AND AMORPHOUS OXIDE THIN FILMS

Christopher C. Knutson, E. William Cowell III, William Stickle, John F. Wager,

Douglas A. Keszler

To be published in *The Journal of Materials Chemistry*

**Introduction:**

This contribution has two thrusts. First, we study diffusion chemistry involving a phase transition in amorphous metal thin films. Second, we investigate how thin an amorphous metal thin-film may be deposited by utilizing an oxidative, solution-processed oxide film. Finally, we summarize the meanings of these findings by surveying plausible devices using the platform of amorphous metals.

Amorphous metals have recently become popular in engineering, tools, hydrogen separation and electronic applications<sup>1-10</sup> due to their morphology combined with properties that usually only come with metallic bonding. Primarily the studies investigate proper composition of the metals to achieve amorphousness over a certain temperature range in the bulk. Some studies have focused on decomposition of these bulk metallic glass (BMG) materials under oxidative stress,<sup>11,12</sup> however study of these materials in the ultra-thin film is rare.<sup>13</sup>

Simply oxidizing a metal into air or solution does not answer key questions about compositional changes in the material, nor does it illustrate how the morphology changes associated with compositional stress. Thickening of native oxide has been characterized electronically.<sup>1</sup> Acid has been shown to selectively etch amorphous metals by electropositivity.<sup>11,12</sup> However, these studies are rarely dimensionally limited in a way that clearly demonstrates segregation dynamics, nor do they significantly probe reagent-limitation dynamics in amorphous metal

We have comprehensively investigated reactions involving amorphous metals and other materials in previous studies,<sup>14</sup> and have done further investigation of the materials presented beyond the scope of this contribution<sup>1</sup>. The scope of this contribution is to alert the thin-film community of interesting chemical reactivity and diffusion interactions involving amorphous metals in quantum-confined materials ranges. We feel that these atomic scales are the most interesting realm of modern physics, electronics and optics.

### **Experimental:**

The amorphous multicomponent metallic film (AMMF) layers were deposited via DC magnetron sputtering onto 100 nm of thermally-oxidized silicon (Hewlett Packard, Corvallis). A three-inch vacuum-arc-melted target with a composition of  $Zr_{40}Cu_{35}Al_{15}Ni_{10}$  was purchased from Kamis Inc. Films were sputtered with powers of 30 and 60 W and a pressure of 3 mTorr with a 20-sccm flow of argon gas. Thickness of the metallic films was controlled via deposition time. Deposition times of 1.0 min, were used at 60 W, and powers of 30 W were used with depositions times of 1.0 min, 40 s and 20 s.

Aluminum oxide phosphate solutions were prepared as described by Meyers, Anderson, Hong, *et. al.*<sup>15</sup> to 0.24 and 0.10-M concentrations of aluminum. The solutions were deposited via spin coating for 30 s at a rate of 3000 rpm, yielding approximately 20-nm and 8-nm films, respectively. Deposition was immediately followed by one minute of thermal treatment at 300 °C on a hotplate open to air.

Further annealing in air using a Neytech QEX furnace was carried out during the first test, and is described in that section.

X-ray Photoelectron Spectroscopy measurements were performed in a Physical Electronics Quantera Scanning ESCA Microprobe with a focused Al K $\alpha$  X-ray (1486.7eV) source for excitation. The X-ray beam used was a 40 W, 200  $\mu$ m X-ray beam spot at the sample. The sputter depth profile data were acquired at a grazing incidence (20° relative to the detector.) Binding energy scales were calibrated using the Cu  $2p_{3/2}$  feature at  $932.62 \pm 0.05$  eV and Au  $4f$  at  $83.96 \pm 0.05$  eV.

Two different ion guns were used for the sputter depth profiles. The first gun used was a 1 keV argon-ion beam rastered over a 3mm x 3mm area. XPS data were collected with 1 eV, 20 mA electrons and low-energy Ar<sup>+</sup> ions to minimize charging artifacts. The second gun used was a C<sub>60</sub> gun with 10kV accelerating voltage and a current of 10nA. This new technique has been shown to be useful in low-energy applications, and offers a slower profile rate than the Ar<sup>+</sup> ions.<sup>16,17</sup>

For TEM analysis, protective-masking films of carbon via vacuum evaporation and iridium via sputtering were blanket-deposited. A standard focused ion beam (FIB) *in situ* lift-out process was used to prepare cross sections in an FEI DualBeam 235 system using 30 kV Ga<sup>+</sup>. Cross-sections were transferred via micromanipulator to a copper grid for final thinning of the TEM membrane. Both sides of the membrane were then milled using a Ga<sup>+</sup> ion beam with 5-kV accelerating voltage and a 6° glancing angle.

TEM measurements were taken in a JEOL JEM2500SE analytical TEM/STEM with a 200 kV accelerating voltage.

### **Results and discussion:**

Thin and continuous films of electronically viable materials are of utmost interest for a variety of science and technology venues. ZrCuAlNi (ZCAN) amorphous metal has been shown to form such thin films.<sup>1</sup> On exposure to air, they react with O<sub>2</sub>(g) to form thin native oxide coatings. The compositions of these oxides are dominated by the high concentration of electroactive Zr in the ZCAN metal. Aluminum has been shown to exhibit similar effects;<sup>14</sup> however, its limited presence (15%) does not generate as high of a statistical probability of reaction at the surface as Zr has. Aluminum will also oxidize, affording native oxide with Al concentrations reflecting that in the original ZCAN composition. Interestingly, the thickness of the surface coating can readily be increased by annealing at modest temperatures (300 °C) for extended periods, while preserving both the amorphous nature of the metal and the smoothness of the metal-oxide interface.

In this contribution we examine the effects of the crystallization of the amorphous metal on the chemistry and structure of the AlPO/ZCAN nanolaminates. Selected laminates are heated to 500 °C, and the resulting behavior is compared with control samples heated at 300 °C.

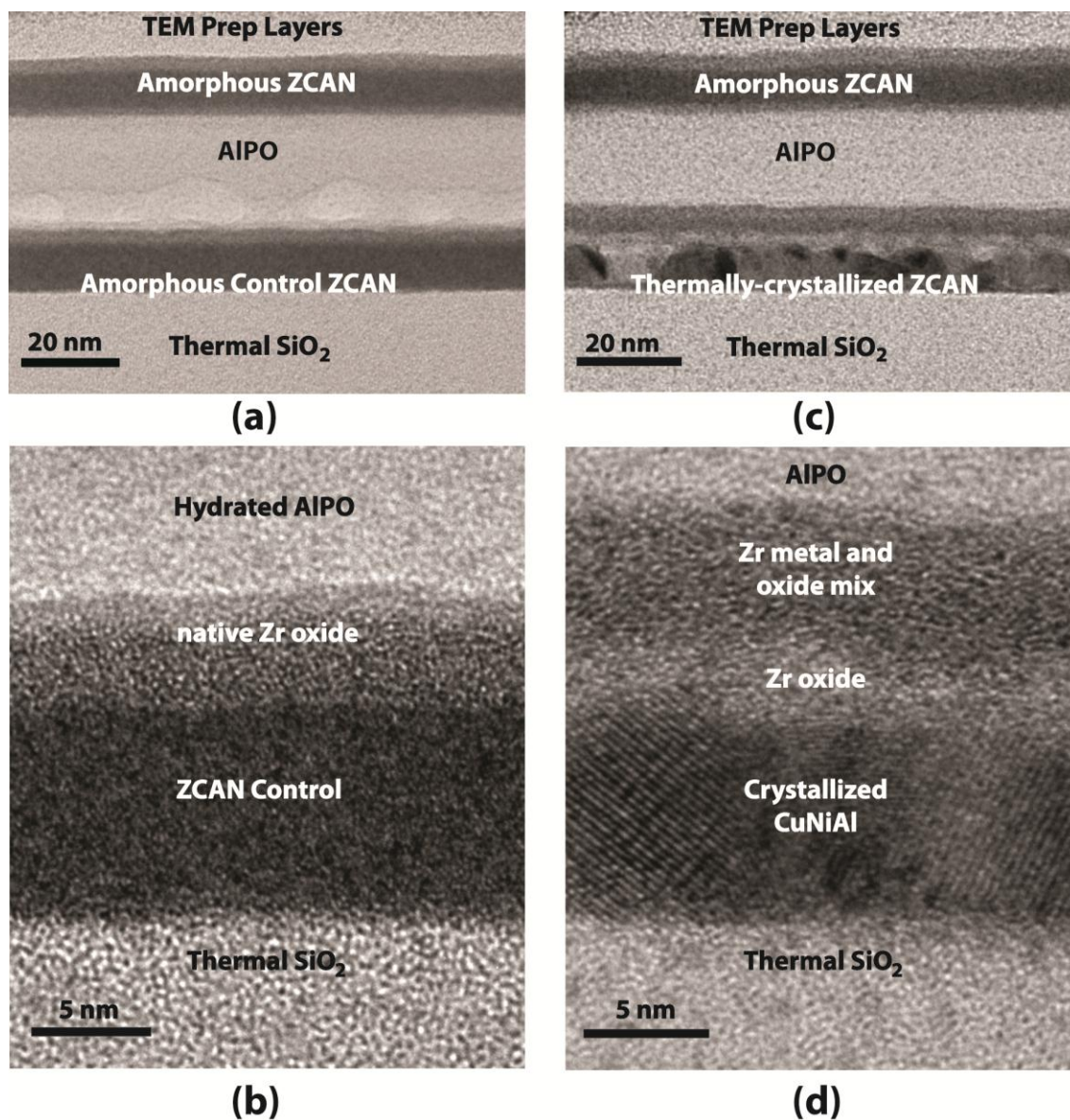


Figure 2.1: (a) Low-resolution TEM image of a ZCAN/AIPO laminate. (b) High-resolution image of 300 °C-thermally activated AIPO/ZCAN barrier layer. (c) Low-resolution TEM image of laminate structure with 300 °C annealed ZCAN and AIPO base topped with a room-temperature deposited ZCAN. (d) High-resolution image of 500 °C thermally activated AIPO/ZCAN barrier layer.

A low resolution TEM image of a thin AIPO layer sandwiched between two ZCAN layers is shown in Figure 2.1(a). The lower ZCAN and AIPO films were annealed at 300 °C prior to deposition of the capping ZCAN layer at room temperature. The continuity of the films and their smooth, defined interfaces are clearly evident. The thin lighter gray contrast layer on top of each ZCAN film represents the native oxide formed on exposure to air. The image also reveals low-density regions, (voids) near the bottom of the AIPO film, indicating that residual water remains in the AIPO film following the 300 °C anneal. This observation is consistent with previous observations on the thermal dehydration of AIPO.<sup>15</sup> The location of these voids indicates that the AIPO film is drying in a top-down fashion. This drying can occur through a combination of the initial anneal, the thermal annealing associated with the energy of the electron beam during TEM imaging, and chemical reduction of H<sub>2</sub>O by an active metal in the ZCAN film. The high-resolution image, Figure 2.1(b), illustrates that the amorphous nature of the bottom film is preserved throughout the 300-°C anneal.

Figure 2.1(c) illustrates exactly what happens when a ZCAN thin film is rapidly annealed past crystallization temperatures when sealed from direct air contact by AIPO. The thin film of amorphous ZCAN, which saw no thermal input after annealing, at the top the stack appears in stark contrast to the extreme crystallinity of the laminate's base ZCAN layer. In contrast to Figure 2.1(a), the image in Figure 2.1(c) contains a rather large swath of gray contrast across the transition between the crystallized metal and the oxide material. It is much larger than previously observed in the control experiment, and contains a contrast gradient that gets lighter and then darker once again as it

transitions from the high-temperature ZCAN into the AIPO film. Further investigation into the atomic compositions of component layers is necessary. The image indicates that the metal is ejecting atoms and ions to fill the void space in the film left by residual hydration.

The crystallization of amorphous metallic components is also of interest. The image in Figure 2.1(c) shows that even a confined amorphous metal of 10 nm in thickness will form separate domain structures in laminates. The high-resolution image in Figure 2.1(d) makes the domain separation obvious by clearly demonstrating two different symmetry directions within the metallic layer. The amount of the sample, or lack thereof, makes diffraction techniques difficult and further work needs to be done to generate samples capable of strong diffraction in the thin film. Regardless of crystal structure, the images in Figure 2.1(c) illustrate the roughening of a 10-nm ZCAN film upon rather moderate, 500 °C processing temperatures; however, that roughness does not appear to translate largely into the films above it.

Previous studies have shown XPS depth profiling to be superior to EDS measurements in the measurement of laminated systems<sup>14</sup>, therefore we utilize XPS measurement to investigate the compositions of the components.

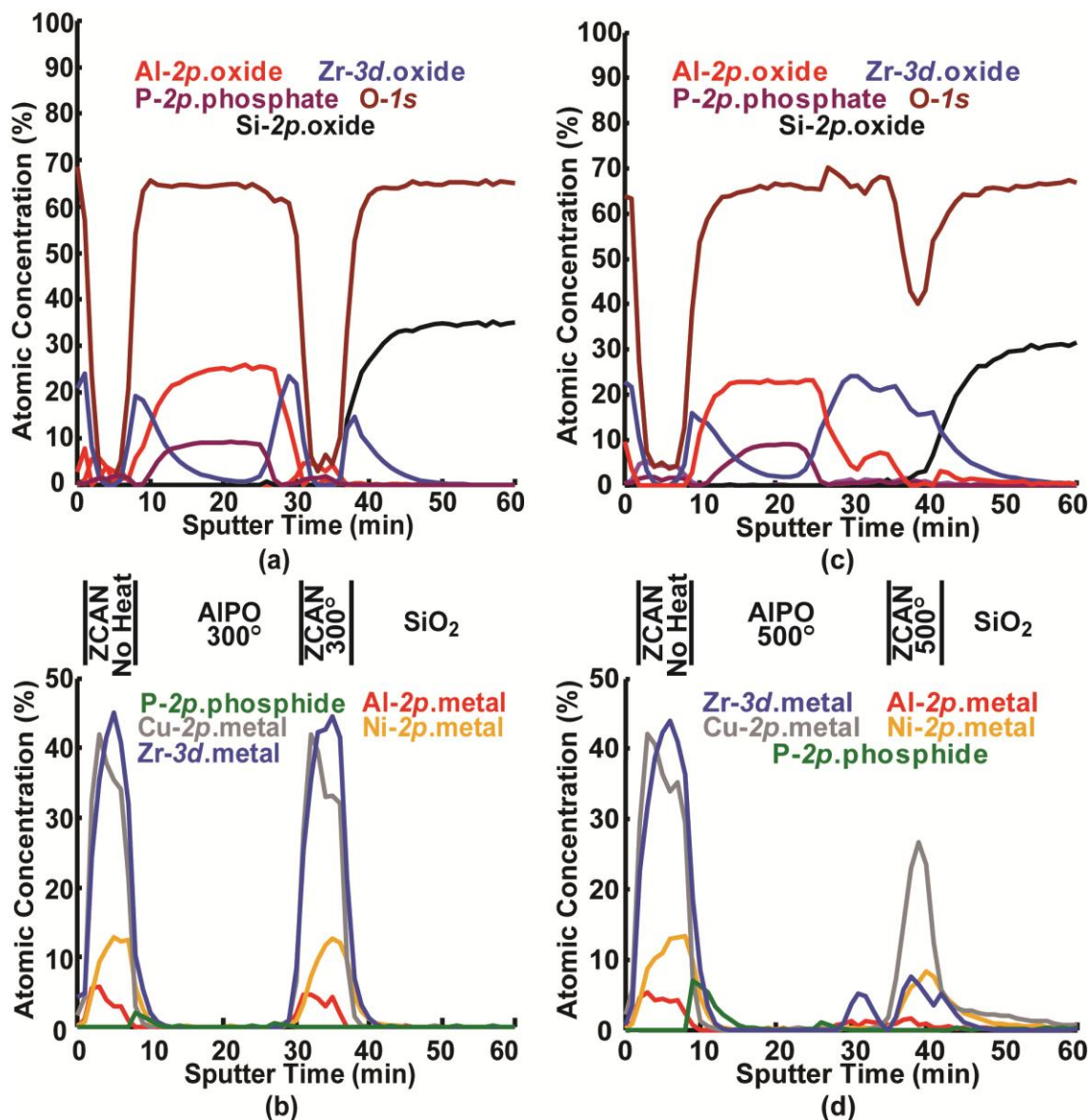


Figure 2.2: (a) XPS depth profile (using  $\text{Ar}^+$ ) of oxidized material in 300°-annealed stack structure processed exactly the same as the structure in Figure 2.1(a). (b) Magnified XPS depth profile of metallic and reduced phosphorus species from system in (a). (c) Depth profile of oxidized material in stack structure processed exactly the same as the structure in Figure 2.1. (d) Magnified XPS depth profile of metallic and reduced phosphorus species from system in (c). All figures are aligned to schematic diagrams of original layer positions and treatments.

The XPS profile in Figure 2.2 mirrors the TEM images from Figure 2.1. Although the sputter times for investigation of the stacks differ, probably due to material hardness of the hydrated AlPO vs. the dehydrated AlPO, the profiles for the as-deposited ZCAN are virtually identical. The 300°-annealed control layer maintains much of the chemical integrity of the as-deposited ZCAN as well. Interestingly, the original location of the native oxide in the control experiment, Figure 2.2(a), is where a minimization of Zr metal is found, which is to say that there is a material valve or pump controlling the flow of zirconium atoms through. There appears to be a great capability for oxygen diffusion and zirconium diffusion in these films as well. Zirconium is so apt to leave the ZCAN layer into the hydrated AlPO film to reduce the water present into hydrogen that the metal will continue leaving the crystallizing film even if there is no more water to reduce.

The other easily oxidized metal, Al, appears to have left the thermally-activated ZCAN film while still present in the 300 °C-annealed film. As seen in Figure 2.2(b), the aluminum is virtually removed from the thermally-activated ZCAN which is expected in light of zirconium's propensity to leave the crystallizing ZCAN. This experiment demonstrates a tendency of zirconium to leave amorphous metals through simple thermal input, even after an oxidation gradient can no longer draw metal from the material. The residual hydration at the interface between the AlPO and the ZCAN appears to be capable of running reactions to pump Zr from the amorphous metal to run a dehydration reaction, and that dehydration reaction appears, in turn to be capable of drawing more Zr from the ZCAN film than there is water to react with. This is an

important insight for both the design of systems involving ZCAN metal and thermal input as well as simply studying the mechanisms of crystallization of multi-component, amorphous metal films.

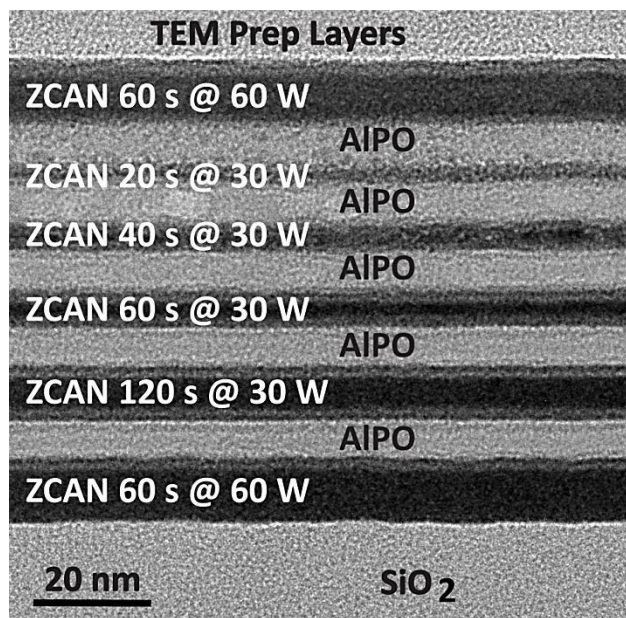
The crystalline material is shown to be primarily made of nickel, copper, zirconium oxide and aluminum oxide. While the Zr and Al migrate into the AlPO film and take the volume left by oxidatively-decomposed water, it is also important to note the propensity of the 500 °C-annealed sample to diffuse copper into the SiO<sub>2</sub> layer in Figure 2.2(d), as expected from copper's status as a mobile defect in SiO<sub>2</sub> and the higher anneal temperature of 500 °C. There is little diffusion of either metal into the SiO<sub>2</sub> layer in Figure 2.2(b). It is important to note that there is virtually no diffusion of nickel or copper into the AlPO from either annealing condition for these structures. Further study of these segregation and selective oxidation effects is warranted.

While the previous experiment highlights what happens to amorphous metal undergoing different annealing conditions, it is important to utilize the information gleaned from the study to gain deeper understanding of ZCAN's behavior within normal processing conditions (i.e. > 300 °C)<sup>1,14</sup>. Therefore, we undertake further investigation focusing on understanding exactly how thin a film of amorphous metal may be deposited by sputtering with regards to the interfacial chemistry of the system.

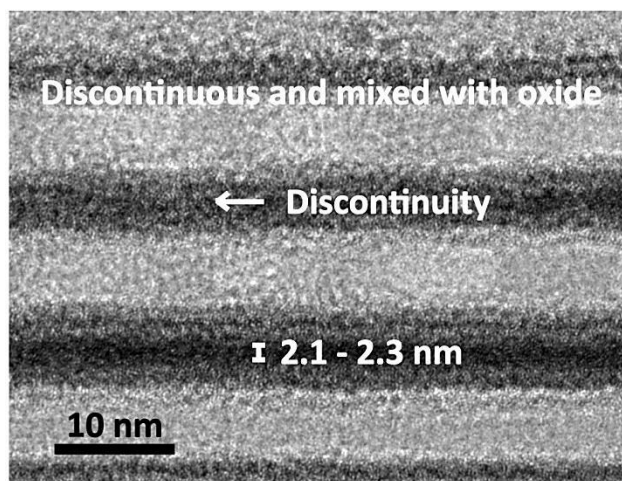
Primary areas of interest for this study include dehydration phenomena and selective reactions of ZCAN's components; therefore a laminate was designed to probe these characteristics. In our laminate, a 0.10 M AlPO dielectric solution precursor was

deposited with 60 s of thermal processing at 300 °C. ZCAN was sputtered first with a power of 60 W for 60 s as has been done in previous studies for reference comparison.<sup>14</sup>

The sputter power was halved to slow the deposition rate, and the sputter time was doubled. Deposition times were successively decreased while maintaining the 30 W sputter. Finally, a capping layer of ZCAN was deposited with no additional thermal input to see if reactions were simply being run by the sputtering deposition, or if there are indeed thermally driven reactions occurring at the base of the spun-on films during the thermal dehydration of the AlPO layers.



(a)



(b)

Figure 2.3: (a) Low-resolution TEM image detailing a laminate with ZCAN depositions carried out as listed. A layer of carbon was deposited atop during TEM preparation. (b) High-resolution TEM of thinnest ZCAN films with issues highlighted.

Figure 2.3 shows what happens with reagent limitation at low temperature (300 °C).

Similar interface oxidation phenomena have been reported in 10-nm films.<sup>14</sup> However in this case, the interface reactions are limited by how much metal is present in the

system to react. It has been measured that the reaction occurring is primarily the oxidation of Zr metal from the ZCAN films<sup>14</sup>, and it appears that while creating a film of less than 2.1 nm, there are not enough metallic atoms to create a homogenous ZCAN film. The thinnest, homogenous ZCAN film we are able to create from the ZCAN/AIPO system at 300 °C was measured by TEM to be 2.1 nm. Attempts at thinner films of metal show morphology problems such as void formation in the AIPO layers and loss of homogeneity in the metal film as can be seen observed Figure 2.3(b). The limitation of the electropositive metals and their subsequent diffusion also limit the dehydration of the solution-processed thin films. Extended exposure to the electron beam, as shown in Figure 2.4, clearly demonstrates where there are not enough electropositive metal atoms to dehydrate the solution-processed oxide material in the top three layers of AIPO.

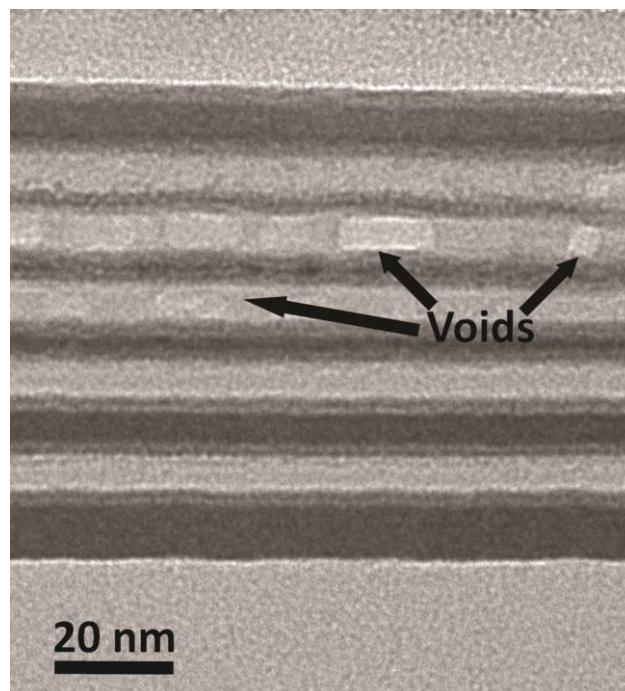


Figure 2.2: Electron-beam annealed sample showing pockets of low density caused by heating and E-beam reduction of water present in the TEM membranes.

The bubbling of the AlPO films located between the thinnest metal films in Figure 2.4 indicates a large amount of water present in the films. When the water is reduced and or evaporated into vacuum during TEM analysis, it leaves bubble-like voids in the areas from which it came. These observations follow logically from electropositivity trends which suggest the reagent limitation of the following reactions:

1.  $\text{Zr} + 2\text{H}_2\text{O} \rightarrow \text{ZrO}_2 + 2\text{H}_2$
2.  $\text{Al} + 3\text{H}_2\text{O} \rightarrow \text{Al}_2\text{O}_3 + 3\text{H}_2$

limit the dehydration of the AlPO films. In Equations 1 and 2, the electropositive metals reduce water to produce hydrogen and metal oxide. It has been shown that nickel-containing amorphous metal systems are useful as hydrogen separation

membranes<sup>3</sup>, indicating that ZCAN may be capable of hydrogen storage and transport, allowing for the removal of the only gaseous product of the preceding reactions.

Indications of the previous reactions moving to completion can be seen in previous work<sup>14</sup> as well as between the thick layers of ZCAN at the bottom of Figure 2.4. 60 s of 30 W sputtering, with subsequent 300 °C annealing is enough to drive sufficient reduction of water in the receiving AIPO film to carry out dehydration such that the AIPO film is not further dehydrated by electron beam exposure.

It is also of note that the cap of non-annealed ZCAN deposited for 60 s at 60 W did not fully dehydrate the layer of AIPO underneath it. This suggests that the layer of ZCAN underneath each dehydrated AIPO layer is contributing electropositive metals to the dehydration of the AIPO film as well. It is clear that in the two bottom-most AIPO films (surrounded by depositions of 60 s at 60 W, 120 s at 30 W and 60 s at 30 W), enough electropositive metal and thermal input from processing is present to drive the metallic dehydration reaction, within the oxide, to completion such that the electron beam no longer removes water during TEM measurement.

Continuity of the films is at the crux of the measurements in this study. The XPS measurements were taken with relatively large spot sizes (200 μm), giving a measure of continuity of the films. While at their thinnest, the AMMF layers begin to selectively segregate into grain-like features, making either confined nanoparticles or a 2-d mesh within a matrix of oxidized components. While obvious in the TEM, the XPS measurements simply detail composition as a function of depth.

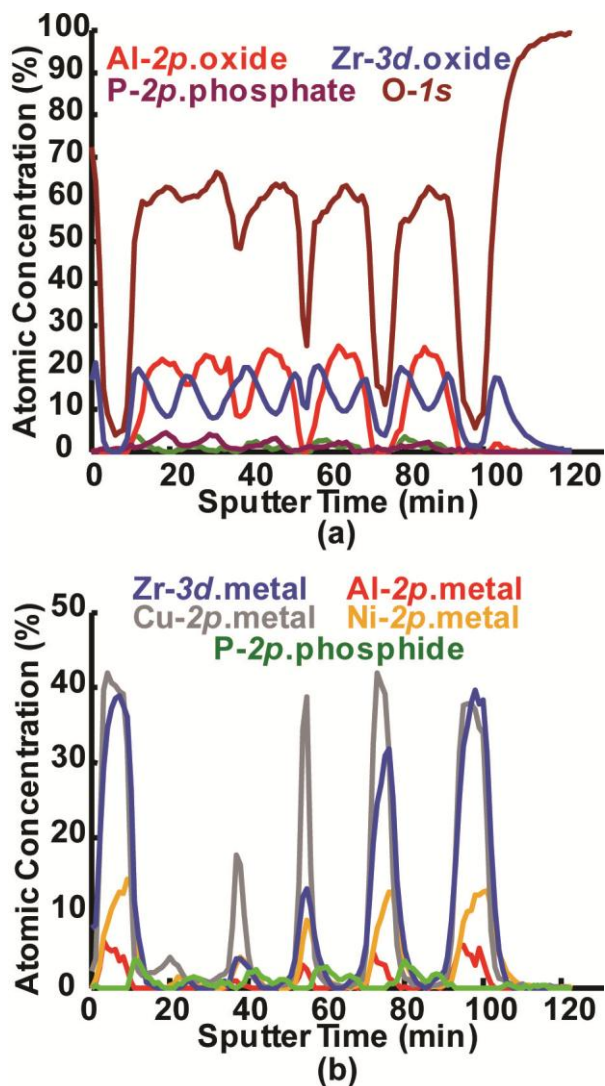


Figure 2.5: (a)  $C_{60}$  XPS depth profiles showing concentrations of oxidized species. (b)  $C_{60}$  XPS depth profiles showing the concentrations of unreacted metals aligned to match the spatial distribution in (a).

Figure 2.5 shows the compositional breakdown of the ZCAN as it is progressively decomposed via chemical reaction of its most electropositive components. At these scales ( $> 6$  nm) any resolution via XPS depth profiling is difficult to attain. A new sputtering technique, using  $C_{60}$  for ablation of inorganic oxides, had to be utilized to gain any resolution of the extremely-thin metals and oxides. The profile contains

phosphide peaks at each sputtered-on interface, indicating that phosphide in previous studies<sup>14</sup> was not formed by  $\text{Ar}^+$  sputtering.

The profile in Figure 2.5(a) shows that this method does not resolve the complete removal of all zirconium oxide in the ZCAN layer unless the ZCAN film is thicker than 5 nm. Aluminum tracking shows that no oxidized aluminum is present in the 60 s, 30 W film indicating presence of pure, highly-electropositive metal. This trend mirrors the lower initial aluminum composition of ZCAN amorphous metal. In Figure 2.5(b) tracking of the metals further illustrates that there is little significant aluminum metal present in the ZCAN layer deposited at 30 W for 40 s. Figure 2.5(b) contains concentrations of Zr metal in all layers of the ZCAN present. This indicates that the Aluminum is the only metal to be completely oxidized away. When contrasted with Figure 2.4, the measurement indicates that aluminum oxidation is a significant force in dehydration, and that the reagent limitation of the dehydration appears to depend on diffusion as well as component-metal electropositivity.

Interesting diffusion is seen within the thinnest layer (30 W for 20 s), in that the diffusion is in stark contrast to the thermal diffusion detailed in Figure 2.2. In Figure 2.2, the copper and nickel segregate downward, toward the  $\text{SiO}_2$ , into the ZCAN's original position. However in the thinnest layer of ZCAN, the copper tends to participate in a much more conventional, random diffusion. In fact, when deposited ultra-thin, the copper appears to diffuse much more readily than when in a continuous amorphous metal film; however no evidence of oxidized copper was observed. This

measurement may simply be due to the fact that the layer deposited at 30 W for 20 s shows evidence of extreme segregation and nanoparticle or 2-d mesh formation as well as significant roughening due to the dehydration reactions in the TEM images of Figure 2.3 and Figure 2.4.

### **Conclusions:**

This work displays thermodynamic and chemical effects on ZCAN amorphous metal systems. The study offers insight into material considerations that should be undertaken when utilizing amorphous metals in thin-film form. First, we show that the thermal input from moderate processing temperatures of 500 °C, into ZCAN thin-film systems causes the measurable ejection of Zr metal through the native, surface oxide, and ultimately a pooling of metal outside of a multi-grain crystalline metallic material. The work demonstrates significant strides forward in understanding how thin a metal film may be sputtered in a smooth, continuous fashion without domain formation and segregation. We also demonstrate that the “bubbling” of the water in the AlPO film dominate the roughness seen in the TEM measurements; and that all initial measurements show incredibly smooth amorphous metal, even when it reacts to become heterogeneous in ultra-thin dimensions.

Segregation effects in ZCAN act similarly in terms of thermal and chemical considerations, meaning that copper and nickel do not readily react in dehydration reactions while aluminum and zirconium metals do, and therefore the significant metal concentrations track accordingly as the films move thinner and thinner. The chemical

phenomena highlighted herein offer insight into deposition parameters and material choices necessary to make the thinnest-possible, continuous metallic films.

Thin, continuous, ultra-smooth, amorphous metallic films have shown utility in electronic applications as electrodes in two terminal devices<sup>1</sup>, and have been theorized to be necessary as components in three-terminal devices<sup>18</sup>. This study shows that interfacial chemistry dominates how thin a homogenous ZCAN amorphous metal film may be sputter deposited. The study also demonstrates what happens when it the ZCAN film is chemically decomposed upon atomic delivery and subsequent chemical reactions during deposition. Similar chemical reactions caused by sputter implantation and subsequent chemical reaction have shown up as asymmetries in two-terminal devices with thick ZCAN films<sup>14</sup> and can be theorized to occur within the confines of trends established in this contribution when deposited thin.

Recent theoretical contributions to optics involving thin, flat films of noble metals and dielectrics propose that noble metal films may be combined with dielectric materials in given ratios to attain negative refractive indices across greater ranges of wavelengths.<sup>19</sup> Further, these planar structures offer capabilities to attain sub-Abbe resolution. In theory, the generation of bulk material properties should be able to attain the ultra-thin; however segregation and crystallization dominate the minimal sizes that elemental, noble-metal films may be readily produced. In this contribution, ZCAN amorphous metal shows the ability to reach thicknesses less than one hundred times smaller than the wavelengths of visible light while remaining smooth and homogenous.

Not only do amorphous metals deposit smooth and continuous layers as thin as 2.1 nm, but they also selectively oxidize to leave meshed-metal dispersions of their most noble components when further reagent limited. In theory, the findings within this paper demonstrate the basic science necessary to tailor amorphous metals for selective reactions capable of generating noble-metal-particle or mesh dispersions within high-refractive-index-oxide matrices by selectively reacting components from the same amorphous metal sputtering-target material. The study demonstrates that the choice of complimentary materials and chemicals for the deposition of ultra-thin amorphous metals is necessary in order to attain the thinnest, continuous metallic films possible.

**References:**

- (1) Cowell, E. W.; Alimardani, N.; Knutson, C. C.; Conley, J. F.; Keszler, D. A.; Gibbons, B. J.; Wager, J. F. *Adv. Mater.* **2011**, *23*, 74-78.
- (2) Grubbs, M.; Zhang, X.; Deal, M.; Nishi, Y.; Clemens, B. M. *Appl. Phys. Lett.* **2010**, *97*, 223505.
- (3) Dolan, M.; Dave, N.; Morpeth, L.; Donelson, R.; Liang, D.; Kellam, M.; Song, S. *J. Membr. Sci.* **2009**, *326*, 549-555.
- (4) Hara, S.; Sakaki, K.; Itoh, N.; Kimura, H. M.; Asami, K.; Inoue, A. *J. Membr. Sci.* **2000**, *164*, 289-294.
- (5) Inoue, A.; Nishiyama, N. *MRS Bull.* **2007**, *32*, 651-658.
- (6) Mulas, G.; Schiffini, L.; Scudino, S.; Cocco, G. *Journal of Alloys and Compounds* **2008**, *454*, 83-88.
- (7) Mulas, G.; Schiffini, L.; Scudino, S.; Cocco, G. *Journal of Alloys and Compounds* **2008**, *455*, 106-112.
- (8) Sharma, P.; Zhang, W.; Amiya, K.; Kimura, H.; Inoue, A. *J. Nanosci. Nanotechnol.* **2005**, *5*, 416-420.
- (9) Tawarayama, H.; Hosono, H.; Yamaura, S.-ichi; Zhang, W.; Inoue, A. *Chem. Lett.* **2009**, *38*, 502.
- (10) Ylönen, M.; Kattelus, H.; Savin, A.; Kivinen, P.; Haatainen, T.; Ahopelto, J. *Microelectron. Eng.* **2003**, *70*, 337-340.
- (11) Padhy, N.; Ningshen, S.; Kamachi Mudali, U. *J. Alloy Compd.* **2010**, *503*, 50-56.
- (12) Paillier, J.; Mickel, C.; Flaviu Gostin, P.; Gebert, A. *Mater. Charact.* **2010**, *61*, 1000-1008.
- (13) Ningshen, S.; Kamachi Mudali, U.; Krishnan, R.; Raj, B. *Surf. Coat. Technol.* **2011**, *205*, 3961-3966.
- (14) Cowell III, E. W.; Knutson, C. C.; Wager, J. F.; Keszler, D. A. *ACS* **2010**, *2*, 1811-1813.

- (15) Meyers, S. T.; Anderson, J. T.; Hong, D.; Hung, C. M.; Wager, J. F.; Keszler, D. A. *Chem. Mater.* **2007**, *19*, 4023-4029.
- (16) Sanada, N.; Yamamoto, A.; Oiwa, R.; Ohashi, Y. *Surf. Interface. Anal.* **2004**, *36*, 280-282.
- (17) Sun, S.; Szakal, C.; Roll, T.; Mazarov, P.; Wucher, A.; Winograd, N. *Surf. Interface. Anal.* **2004**, *36*, 1367-1372.
- (18) Cowell, E. W. Amorphous multi-component metals as electrode materials, Oregon State University, 2010.
- (19) Cai, W.; Genov, D.; Shalaev, V. *Phys. Rev. B* **2005**, *72*.

## Chapter 3

# INTERFACE CHEMISTRIES IN NANOLAMINATES OF AMORPHOUS METALS AND AMORPHOUS OXIDES

Christopher C. Knutson, E. William Cowell III, William Stickle, Ronald Kelley,  
Randy Burgess, Peter Eschbach, Alan J. Telecky, John F. Wager, and Douglas A.

Keszler

To be published in *Surface and Interface Analysis*

## Introduction

This contribution investigates the interfacial solid-state reactions occurring during solution deposition and the more energetic deposition method of sputtering. Multiple experiments are presented to illustrate trends in laminar, solid-state chemical reactions in ultra-thin, ultra-smooth amorphous metal and oxide materials. These experiments define and detail the parameters and thickness limitations inherent to the deposition of these material sets. Advances in thin-film technologies<sup>3,1</sup> make this work of great interest because this work defines the basis of interfacial chemistries occurring at the junctions of ultrathin, ultra-smooth metal and oxide films necessary to properly engineer nano-scale effects through the use of amorphous materials.

The first set of experiments attempts to define the actual surface depth of chemical reactions at each interface (e.g. metal on oxide and oxide on metal) of the laminate. A second set of experiments provides insight into the chemical mechanism of the measured XPS interfacial chemistry. A pure, electropositive metal and a pure, semi-noble metal are deposited in order to test the observed diffusion and interfacial chemical gradients. The phosphorus concentration within the amorphous oxide is then varied to test reagent limitation within the film as a method for controlling a measured interfacial reaction. Sputter power during deposition is investigated to determine if deposition rate plays a role in the interfacial chemistries present. We probe the diversity of the system by investigating laminates made using an alternate amorphous metal composition and finally we probe the initial amorphous metal's reactivity with aqueous-solution processed oxide materials containing sulfate species.

Amorphous-oxide thin films are material staples in current and emerging devices as insulators. Amorphous metals, in combination with amorphous oxides, have recently been used to fabricate the first examples of high-performance tunneling diodes.<sup>2</sup> In amorphous tunneling diodes, very thin oxide layers < 10 nm are employed. Such systems also provide capabilities for hydrogen separation.<sup>3-6</sup> Fundamental chemical economies drive the question of how thin these devices may be fabricated, and what kind of chemical reactions occur at the interfaces of these rather novel materials. As such, the nature of the metal-insulator interface, occupying a significant portion of the insulator thickness, can play a major role in affecting physical and chemical performance.

In a recent contribution<sup>7</sup> we described a new platform of amorphous metals and solution-processed oxides that provides a unique opportunity to study interfacial chemistries. We also have begun to describe how interfacial chemistry dominates the capabilities and responses of two-terminal systems in the ultra-small scale.<sup>2</sup> The interfacial chemistries in our tunneling diode system also offer valuable insight into considerations which need to be taken when making ultra-thin, laminated devices. Further, our system choices used to create regular, repeating laminated structures were very deliberate. Our aim was to create a system with all components on the order of the thickness of a tunneling barrier (10 nm) at the relatively large test-scale of 1" x 1".

We approached this problem as an exercise in depositing extremely flat glass. The most successful approach to producing thin, large-scale, flat glass is the process of floating glass.<sup>8</sup> Pilkington discovered that floating silica glass atop molten (amorphous)

tin allows the production of virtually any desired size of flat glass panes. Pilkington-type glass-floating processes are widely used in production of high-quality windows and display planes because the method utilizes surface tensions to create smooth and uniform sheets of glass.

We propose a unique method of utilizing similar forces and materials in order to create ultra-smooth nanoscale lamination techniques at 300° C. Creating solid systems that exhibit similar characteristics to the float glass process at temperatures under 400° C is a unique challenge, with unparalleled capabilities to produce smooth, thin and consistent films. The challenge is overcome through thoughtful material and processing choices.

A series of inorganic, aqueous-solution-processed oxides has recently emerged at the forefront of planarization, patterning and deposition of smooth, consistent, electronically-viable thin-film oxides with the capability to be manufactured over large-scale glass at low cost.<sup>9-16</sup> The general method employed in these examples of inorganic, aqueous-solution-processed oxides utilizes the surface tension of water to produce atomically-smooth oxide surfaces via spin-coating. The high surface tension of molten glass is replaced with the lower surface tension of the solution by creating incredibly small particles and evenly dispersing them in a true solution with water. The nanoscale optimization of the same principles of floating glass has been realized, and with it a new ability to simply and efficiently produce layered dielectric materials for optical devices has emerged.<sup>17</sup>

The amorphous metal composition presented in this contribution remains amorphous at processing temperatures of 300° C.<sup>7</sup> There is a reported window of stoichiometric makeup allowing bulk metallic glass behavior for this system.<sup>18</sup> The amorphous AlPO dielectric is also capable of remaining glassy over wide compositional ranges<sup>13</sup> and is shown to remain amorphous throughout this work. The amorphousness of the HafSOx dielectric system<sup>9</sup> is shown to be more sensitive to atomic economy from interfacial chemical reactions.

Controlled nanoscale material delivery is inherently based upon atom economy and speciation. The metal and dielectric systems demonstrated in this contribution allow for controlled deposition, reliable material compositions and repeatable interfaces. By choosing extremely planar deposition methods of statistically randomized atomic arrangements in each component material of a laminate, the delivery of both metal and dielectric systems is controlled over large scales. Statistically randomizing atoms in each respective layer of a laminated solid-state system is a novel way of turning a three-dimensional problem into a more two-dimensional problem.

Amorphous metals are a promising field of study due to the novel properties resulting from their metallic nature combined with isotropically-disordered structure. Typically these studies are limited to bulk, physical characterizations;<sup>19-22</sup> however, relatively thin-film surface chemistries are starting to be recognized.<sup>23</sup> Thin films of amorphous metals deposited via DC-magnetron sputtering are low-cost, atomically smooth and electronically viable in nanoscale tunneling,<sup>2</sup> and metal oxide semiconductor electronic devices.<sup>24</sup> Aqueous acid on amorphous metal interface reactivities have been studied

electrochemically<sup>22</sup> and by microscopic evaluation of corrosion phenomena,<sup>21</sup> however little is known, to date, about their reactions in solid-state, laminated systems.

Mixed metal/oxide laminates have been demonstrated to produce negative-index of refraction into optical wavelengths.<sup>25</sup> To engineer the next generation of miniaturization of this class of laminated devices, it is inherently beneficial to understand the limitations on common materials such as the surface roughness of crystalline thin-films and the propensity to additively distort layered structures at the nanoscale by successively piling rough, polycrystalline materials without high-quality planarization.

Understanding the interfacial chemistries that occur between amorphous metals and oxide glasses is necessary for the optimizations of devices with nanoscopic bilayers due to the exceedingly high interface-to-bulk ratios that occur between extremely-thin films. Ultra-smooth interfaces are of exceeding importance in systems that require extreme uniformity over large areas because surface roughness can magnify local fields in laminated devices<sup>2</sup>, and offer opportunities for the scattering of photons. As stack-structured metal/oxide metamaterials move to smaller scale, the control of ultra-smooth interfaces is necessary for predictive modeling.

Nanoparticle surface chemistries have been of recent interest,<sup>26-28</sup> but little has been fully characterized about their surfaces to date because of issues involving oxidation changes in the particles during evaluation by an electron beam.<sup>29</sup> This contribution demonstrates a novel method of producing high-quality, atomically-smooth, ultra-thin laminates of amorphous metals and glasses. We also demonstrate that this method allows for reagent-limitation studies and energy-input control of blanketed, vertical

nanoscale structures. We have previously shown that solution deposition and DC-magnetron sputtering of amorphous materials allow the tailoring of amorphous metal/oxide laminated materials to nanoscale bilayer thicknesses at temperatures below 400° C.<sup>7</sup>, however this is the first comprehensive study into the nature of the interfaces that occur within these amorphous metamaterials as well as the methods needed to measure the interfacial chemistries.

The nature of the films and interfaces are investigated in terms of chemical compositions via X-ray photoelectron spectroscopy and cross sectional morphology via transmission electron microscopy. By being constrained vertically in a stacked matrix, reactions of the amorphous metal with the TEM electron beam are minimized, overcoming a serious issue of nanoparticle measurement.<sup>29</sup> Finally, a wider set of metal and amorphous, polycationic oxides are investigated to give further insight into the interfacial reactions specific to laminated amorphous metal/oxide materials.

Simple explanations of the observed behavior are presented as a mix of solid-state chemistry, oxidation-reduction chemistry and reagent-limited dehydration reactions. Amorphous metal/oxide laminates probe the lower limits of current nanotechnology in the production and measurement of highly-consistent, nanoscale metamaterials. The study also illuminates a method to investigate solid-state interfacial reactions pertinent to surface catalysis and the reactivities of isotropically dispersed, anisotropically arranged material sets. The demonstrated control of crystallinity and layer thickness in the individual materials allow for investigations on the scale of tens of atoms. This study probes oxidation phenomena in amorphous metals, and shows evidence of

preferential, highly-reactive segregation events concurrent with reported bulk observations of glassy metals fabricated with similar composition under oxidative environmental stress.<sup>21,22</sup>

## **Experimental**

Three-inch, vacuum-arc-melted multicomponent metal targets were purchased from Kamis Inc. with stoichiometric compositions of  $Zr_{40}Cu_{35}Al_{15}Ni_{10}$  and  $(TiAl_3)$ . Thin films were deposited from these targets via DC magnetron sputtering. Power was adjusted between 30 and 60 W, at a pressure of 3 mTorr with a 20-sccm flow of Ar (g) gas. Pure Ti and Cu metals were deposited from two-inch targets via RF magnetron sputtering at powers of 60 watts at a pressure of 5 mtorr and a 20-sccm flow of Ar (g).

Aluminum oxide phosphate (AlPO) solution precursors for the film deposition were prepared as previously described by Meyers and coworkers<sup>13</sup> to a 0.1-M concentration of aluminum with nitric acid as the strong acid. An aluminum to phosphate ratio of 5:3 was chosen for all films unless noted otherwise. Amorphous zirconium oxide sulfate, and hafnium oxide sulfate solutions were prepared as previously described by Anderson and coworkers<sup>9</sup> to a 0.080 M concentration of zirconium or hafnium. All solutions were spin-coated onto the AMMF at a speed of 3000 rpm for a duration of 30 s, followed by treatment at 300° C for 1 min on a hotplate in air. All samples were prepared on 1in<sup>2</sup> coupons of thermally oxidized silicon provided by the Hewlett Packard's company.

X-ray Photoelectron Spectroscopy (XPS) measurements were performed in a Physical Electronics Quantera Scanning ESCA Microprobe with a focused monochromatic Al Ka X-ray (1486.7eV) source for excitation. The X-ray is a 40 W beam, with a 200 μm

diameter X-ray beam spot at the sample. The sputter depth profile data were acquired at grazing incidence with the samples rotated  $20^\circ$  relative to the detector. Binding energies were calibrated by using the Cu  $2p_{3/2}$  feature at  $932.62 \pm 0.05$  eV and Au  $4f$  at  $83.96 \pm 0.05$  eV. Samples were sputtered using a standard Quanterra ion gun with a 1 KeV argon-ion beam rastered over a 3 mm x 3 mm area. To minimize charging artifacts, the XPS data were collected with 1 eV, 20  $\mu$ A electrons and low-energy  $\text{Ar}^+$  ions.

Samples for TEM analysis, were first coated with carbon (vacuum evaporator, 30 sec) and iridium (sputtered, 2.5 min) as protective masks. Cross-section samples were then prepared using a standard FIB in-situ lift-out process in an FEI DualBeam 235 system. This process involves FIB patterning of a 1- $\mu$ m thick membrane using a 30 kV  $\text{Ga}^+$  ion beam and then transferring the membrane to a copper half-grid using a micromanipulator inside the DualBeam system. Once attached to the copper grid, the membrane was further milled to an electron transparent thickness ( $< 100$  nm). For final preparation, both sides of the membrane were milled using a  $\text{Ga}^+$  ion beam with a 5-kV accelerating voltage at a  $6^\circ$  glancing angle.

TEM analysis was performed in a JEOL JEM2500SE analytical TEM/STEM employing a 200 kV accelerating voltage. For beam sensitive samples, efforts were made to image the sample using the least beam current possible to reduce beam heating effects. Electron diffraction was carried out in a FEI Titan 80-300 TEM with 200 kV accelerating voltage.

The artistic overlays were completed by utilizing raw image files from the JEOL JEM2500SE TEM, separating the scale bar via pixel-counting, cutting and rotating the

desired image from the raw file and overlaying the original pixel-counted scale bar over the adjusted image by utilizing Adobe Photoshop. XPS data were then overlaid on the TEM images. Original images are attached as supplemental information.

### **Results and discussion**

A laminate was prepared to test the amorphousness of the system by utilizing electron diffraction. Previously characterized interfaces<sup>7</sup> were further investigated in order to determine the degree of crystallinity of the interfacial volumes. TEM images in Figure 3.1 display the interfacial reaction zones as light gray zones atop and below the amorphous metal layers.

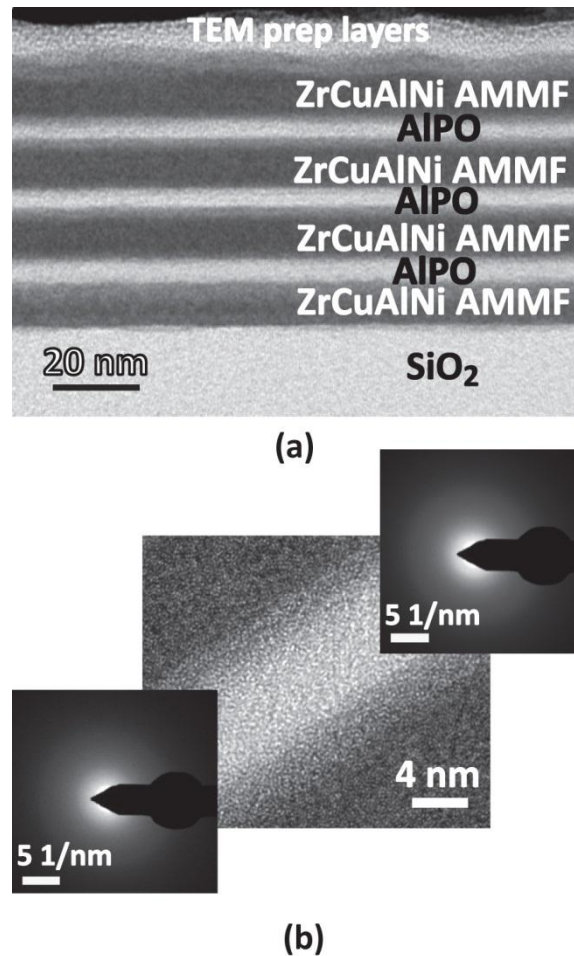


Figure 3.1: (a)TEM micrograph of nanolaminated structure with four layers of ZrCuNiAl amorphous metal separated by three layers of AlPO. (b)High-resolution TEM micrograph of a single metal-insulator-metal section from the AlPO/AMMF nanolaminate pictured in (a). The electron diffractions presented are taken from the interfacial regions pictured in (b) such that the tip is laterally even with each interface investigated by the diffraction.

As seen in (a) of Figure 3.1, the TEM image reveals a highly-structured nanolaminate with films  $\leq 10$ -nm thick. It is rather remarkable that such a high-quality laminate can be produced by combining conventional sputtering and application of an aqueous solution with an eyedropper. While the interfaces are quite smooth, they are not abrupt. The gray-scale transitions at the interfaces in the high-magnification image (Figure

3.1(b)) provides evidence that chemical interdiffusion has occurred. Initial laminates as pictured in Figure 3.1(a) received no additional thermal input beyond the 300° C hot-plate treatments of each oxide layer. Electron-diffraction samples were taken from the interdiffusion regions as well as the metal and dielectric layers. All areas provided amorphous patterns to electron diffraction as shown in Figure 3.1(b).

Earlier EDS profile studies have shown incongruent diffusion profiles throughout the oxide layer of the laminate.<sup>7</sup> Specifically, the profiles detailed the termination of copper and nickel at the oxide/AMMF interface while zirconium permeated the entire stack.<sup>7</sup> The extreme smoothness and repeatability of the films is obvious from the TEM image; however, there are also shaded areas of the AlPO film near the interfaces indicating surface chemistry occurring at each junction. XPS depth profiling provides a means to measure composition and oxidation-state gradients and probe the makeup of the interface regions for this sample.

Figure 3.2(a) shows the distributions of the zero-valent metal atoms largely tracks the ZCAN film pattern. Likewise, the Al<sup>3+</sup> profile (Figure 3.2(b)) tracks the sequence of AlPO layers. The presence of high Zr<sup>4+</sup> concentrations is consistent with each chemical reaction at the interfaces. No significant concentration of charged Cu or Ni species were found in the interface regions. Curiously, phosphorus was detected as P<sup>3-</sup> rather than the expected phosphate P<sup>5+</sup>. This phosphide concentration peaks at the ZCAN-on-AlPO interface.

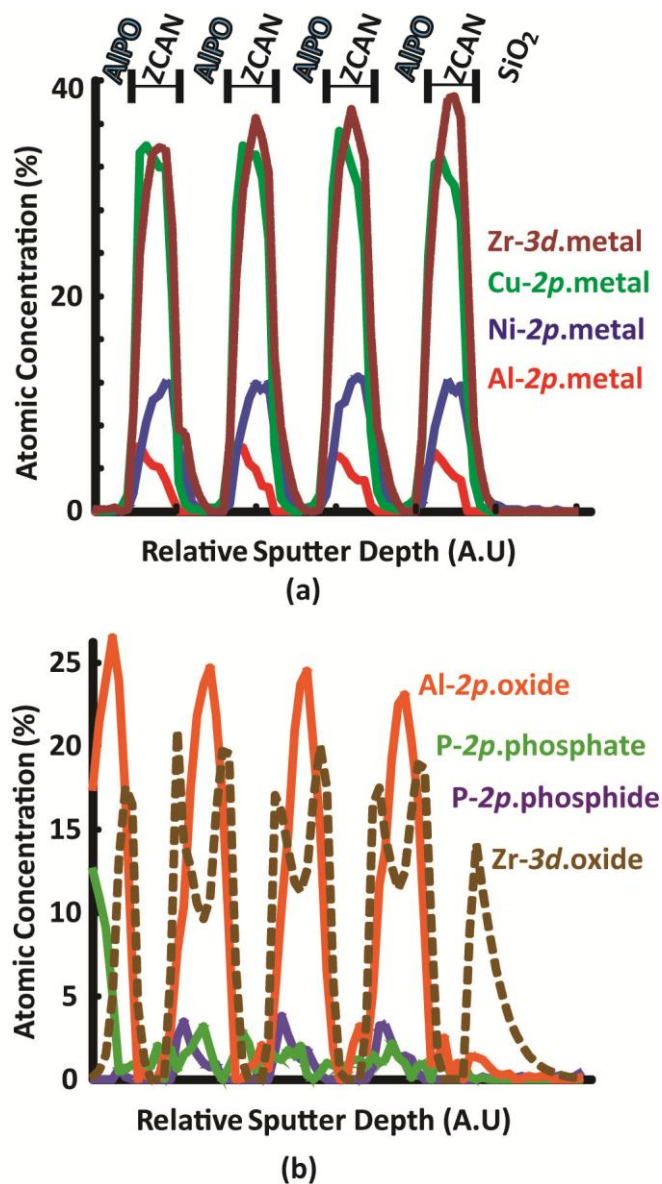
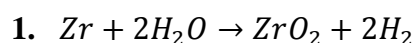


Figure 3.2: (a) XPS depth profile of neutrally-charged metals from nanolaminated structure with four bilayers of AlPO-topped ZrCuNiAl, topped with a schematic diagram labeling the component layers. (b) XPS depth profile of selected ions from the same nanolaminated structure.

The TEM images in Figure 3.1 show smooth, continuous layers, in a spatially-small analysis volume. The XPS depth profiles provide information from a much larger area (9mm<sup>2</sup>). Nanometer-scale resolution from a large analysis area is indicative of

incredibly uniform films. Crystalline roughness makes the deconvolution of highly spatially-resolved interfacial XPS depth profiles difficult. Our method of planarization through surface tension and amorphousness allows for extremely long-range laminated order in the planar dimensions while maintaining incredibly-thin vertical dimensions. These features of our films allow the demonstration of the capabilities of the Quantera instrument and the analytical apparatus.

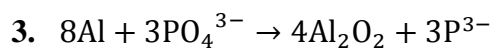
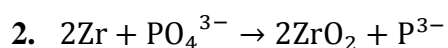
The XPS depth profiles presented in Figure 3.2 also show evidence of differing interfacial reactions. The primary reaction involves the oxidation of zirconium metal to Zr(IV) at each interface which is congruent with the TEM measurements. Literature suggests that "valve" metals in bulk metallic glasses, such as zirconium, oxidize preferentially in the presence of oxidizers.<sup>21-23</sup> We suggest that at the surface, these valve metals are capable of reducing any residual hydration in surrounding films as shown in Equation 1, and that the valve metals are capable of driving further reactions discussed later. The oxides used in this study are all reported to contain water at the processing temperatures used<sup>9,13</sup>, making the following reaction highly probable of not only oxidizing the zirconium, but also allowing for interdiffusion by freeing up volume within the oxide film. Amorphous metals have been shown to take up hydrogen<sup>3</sup>, making equation 1 likely to produce little change in the amorphous metal in the stack structures.



The amorphous metals are processed under vacuum while the subsequent solution deposition is carried out in ambient atmospheric conditions. The surface of the

amorphous metal oxidizes when removed from the deposition chamber. The XPS profiles show that the surface oxide is primarily Zr(IV) oxide, which is consistent with the electropositivity trend of the metals present in the ZrCuAlNi AMMF.

The interface created by the sputter deposition of the metal onto the AlPO exhibits interesting reduction chemistry. Tapering Zr<sup>4+</sup> and Al<sup>3+</sup> profiles are consistently observed when the ZrCuAlNi film is deposited upon either aluminum phosphate oxide or thermally oxidized silicon. Trace amounts of phosphide are measured in each interface in which AlPO is deposited upon AMMF. It is important to note that these phosphide species are not detected in AlPO samples without metal deposited atop them. The following reactions are proposed for the observed phosphide at the interface:



Phosphide is consistently measured at the sputtered-on interfaces within this material set in multiple experiments. We propose that the origin of the phosphide in the measurement is due to the energy of sputtering combined with the electropositivity of the valve metals present; however, we have been unable to test if the phosphide is measured on the same interface if the XPS profile is taken in the opposite direction. Experimental parameters have not yet been developed to run the previously described tests of directional dependence of phosphide formation. We show that the measurement of phosphide can be made rather consistently and that there is chemistry occurring during sputtering interactions with these laminates, be it during the original deposition or the XPS profiling.

Further investigation into the origin and control of the phosphide formation is undertaken utilizing the current analytical configuration. Negligible migration of the copper and nickel into the interfacial regions is measured, demonstrating that the trend of electropositivity within the metals contained in the ZrCuAlNi AMMF has the largest effect on reaction and subsequent migration into the oxide films.

### **Metallic Modulation of Reaction at the Sputtered-on Interfaces**

Both copper and titanium metals are RF-magnetron sputtered onto amorphous AlPO films to test the effects of the electropositivity of the sputtered-on metal in the formation of phosphide at the top interface. Titanium is used because of its similar oxidation chemistry to zirconium. Copper was investigated due to the measured lack of migration and oxidation in the initial investigations of the laminated structures.<sup>7</sup>

The difference in oxygen affinity between the two metals is illustrated in the TEM images and XPS profiles provided in Figure 3.3. The TEM image in Figure 3.3(a) displays a crystalline, metallic top film of copper while the titanium pictured in Figure 3.3(c) produces an oxide when exposed to atmosphere. The titanium shows a propensity toward the measurement of phosphide in the sputtered-on surface while the copper interface shows no detectable reduction of phosphorus. The trend illustrates the spontaneity of the respective electrochemical cells in acidic solution, with  $\text{Cu} \mid \text{Cu}^{2+} \parallel \text{P} \mid \text{P}^{3-}$  being unfavorable and  $\text{Ti} \mid \text{Ti}^{4+} \parallel \text{P} \mid \text{P}^{3-}$  being favorable.

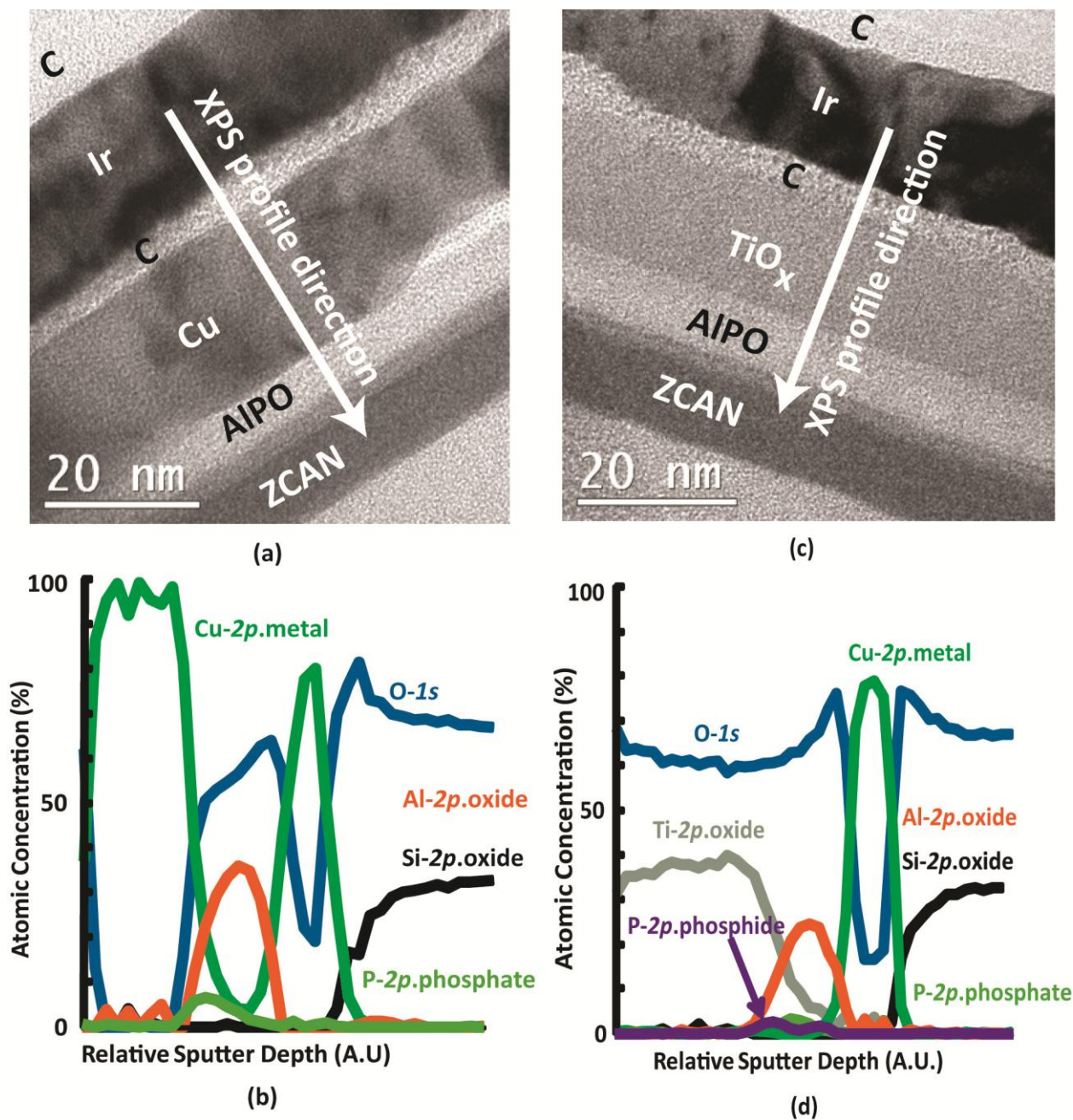
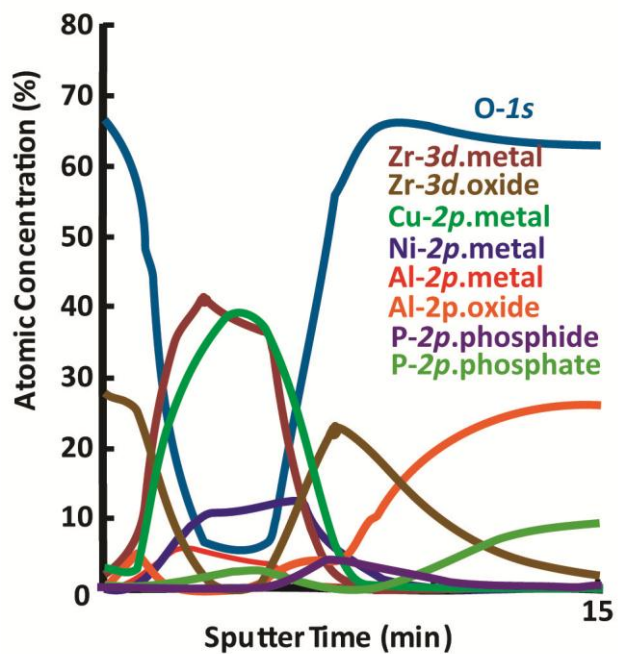


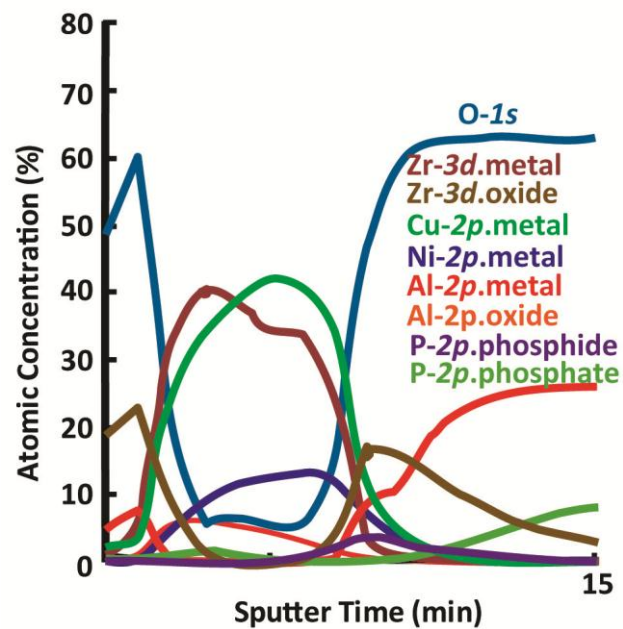
Figure 3.3: (a)TEM micrograph of Cu-AlPO-ZrCuAlNi laminate with the direction of the XPS profile indicated on the image. (b) XPS depth profile of the structure pictured in (a). (c)TEM micrograph of Ti-AlPO-ZrCuAlNi laminate with the direction of the XPS profile indicated on the image. (d) XPS depth profile of the structure pictured in (c).

### **Effects of Adjusting Sputtering Power**

Further investigation of the novel formation of phosphide at the sputtered-on interfaces is arranged to test for the source of the phosphide formation. It is hypothesized here that if the cause of the phosphide formation is in fact the initial deposition that adjusting sputter power will influence the amount and depth of phosphide formation at the interface. An experiment is devised in which sputter power was adjusted between 30 and 60 watts to measure the dependence of phosphide formation on the ZrCuAlNi deposition rate. ZrCuAlNi/AlPO structures were constructed on thermally oxidized silicon using a thick, high-temperature-annealed (800° C for 1 hour) AlPO bases to ensure dehydration<sup>13</sup>. This test confirmed that sputter power can be adjusted over a wide range and still produce consistent, amorphous metallic films from the same target. Figure 3.4 shows that no statistically discernable differences in phosphide or Zr(IV) concentrations were measured between the two powers, while the elemental composition of the amorphous metal remained consistent with previous samples. Being that the sputter power determines deposition rate of the amorphous metal, this work shows that sputter-deposition time can be easily adjusted without significant further effect on this system. This test also points to the source of the phosphide being either external to the production of the laminated stack or independent of sputtering power.



(a)



(b)

Figure 3.4: (a) XPS profile of ZrCuNiAl deposited onto high-temperature annealed AlPO at 30 W. (b) XPS profile of ZrCuAlNi deposited onto high-temperature-annealed AlPO at 60 W.

### Effects of Adjusting Phosphate Concentration in AIPO

A laminate was constructed in order to study the effect of the AIPO's concentration of phosphorus on the formation of phosphide. The laminate pictured in Figure 3.5 was fabricated with three AIPO layers of differing Al:P ratios. The stoichiometric Al:P ratios in the AIPO were arranged from the bottom of the laminate structure to be 5:3, 2:1 and 10:7 respectively. The AMMF layers of ZCAN were consistently kept to 10 nm with standard deposition energy and gas flows.

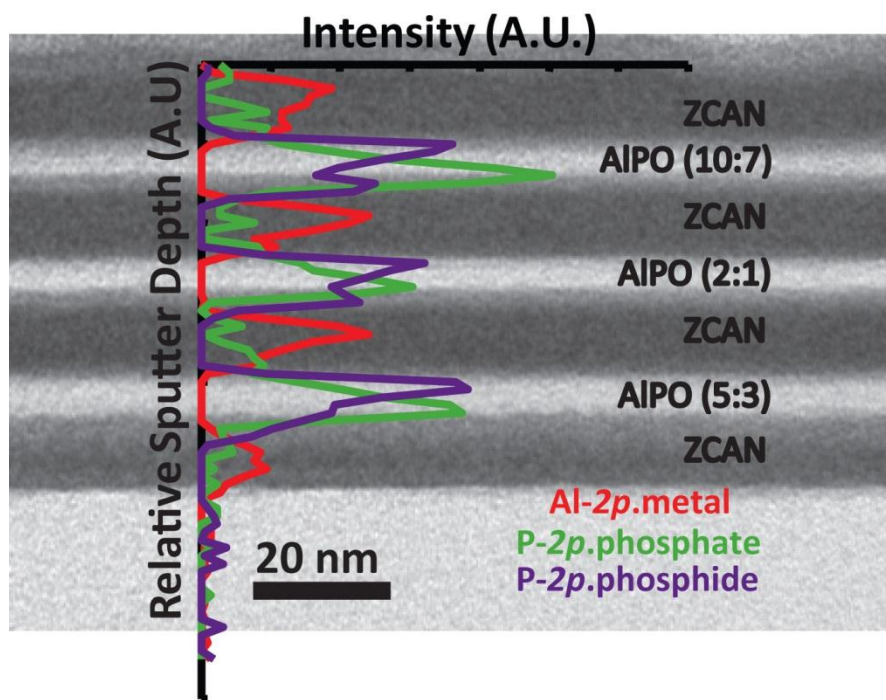


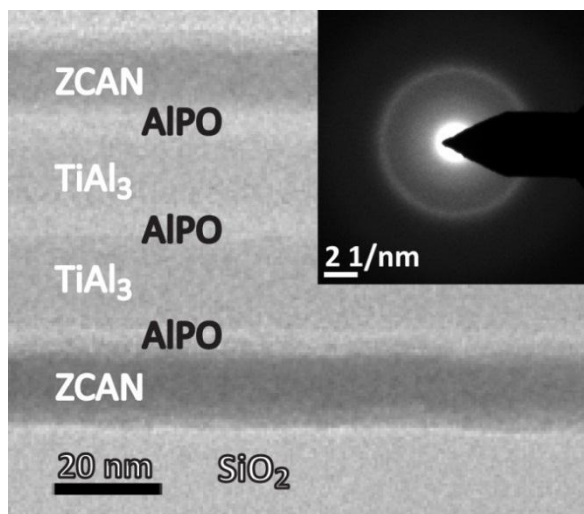
Figure 3.5: Labeled TEM micrograph of ZrCuAlNi-AIPO laminate utilizing AIPO precursors with different Al:P ratios with overlaid intensity profile of phosphate, phosphide and aluminum metal arranged for intuitive spatial overlap.

The image in Figure 3.5 illustrates that a difference in initial phosphate concentration of the solution is carried over into the composition of the laminate. The phosphate intensity corresponds directly to phosphate concentrations in the initial solution and

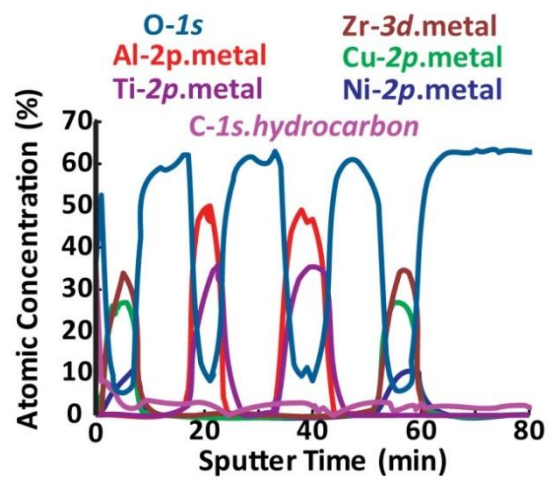
subsequent film. The measured phosphide intensities vary little between the bilayers with Al:P = 5:3 and 10:7, while significantly less phosphide is observed when Al:P = 2:1. More exploration is needed to determine if this is an indication of a zirconium-limited reduction of the phosphorus at the interface, but initial studies indicate this to be a valid hypothesis. Further measurement with lower-energy profiling methods may have the ability to uncover whether or not the differences in observed phosphide have to do with profile sputter energy and whether or not better resolution may be attained with the XPS profiles utilizing a less energetically-intense sputtering species.

### **Investigation of $\text{TiAl}_3$ Amorphous Metal**

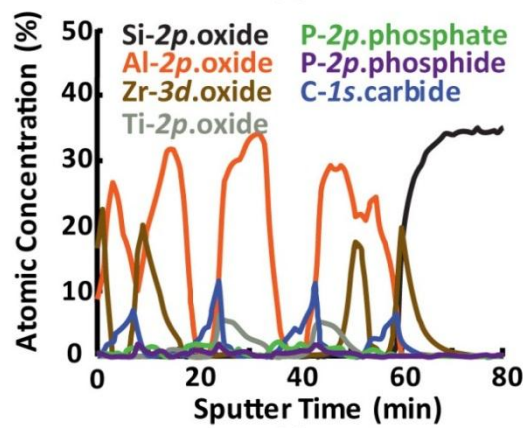
Figure 3.6: (a) Labeled schematic diagram of ZrCuAlNi-AlPO-TiAl<sub>3</sub> laminate with inset electron diffraction taken from section of film displayed. (b) Labeled XPS depth profile of unreacted metals and O<sup>2-</sup> in the ZCAN-AlPO-TiAl<sub>3</sub> laminate (c) XPS profile of charged species present in the laminate.



(a)



(b)



(c)

A laminate containing ZrCuAlNi amorphous metal and TiAl<sub>3</sub> amorphous metal was fabricated in order to investigate if the system would remain amorphous as well as exhibit similar interfacial chemistry due to the electropositive nature of both elements in the TiAl<sub>3</sub> metallic glass. The image in Figure 3.6(a) shows the structure of the metal/oxide laminate constructed with both TiAl and ZrCuAlNi amorphous metal systems. A slight difference in the thicknesses of the TiAl<sub>3</sub> layers is due to off-axis sputtering. The target was placed slightly off axis to test whether or not sputter power has an effect on the interfacial chemistry of the system, and deposition time was kept constant. The pictured area was then investigated by electron diffraction in Figure 3.6(a), and found to be completely amorphous. These systems allow for various compositions of ultra-thin, continuous, amorphous metallic films to be easily integrated into metal/oxide laminated structures.

XPS depth profile in Figure 3.6 (b) and (c) show anionic oxygen alongside the metallic elemental species of the structure pictured in Figure 3.6 (a). Figure 3.6 demonstrates the same chemistries for the ZCAN / AIPO interfaces as previously measured on the ZCAN layers while TiAl<sub>3</sub> films also show a propensity to form phosphide at the interface with the aluminum oxide phosphate glass. These findings are congruent with the theory that electropositivities of the metals dominate the phosphide response in the sputtered-on interface. No significant difference in phosphide formation is measured between the on-axis and off-axis sputtering, indicating that the TiAl<sub>3</sub> interfacial, phosphide-generating reaction is not dependent upon deposition rate. Carbon species are observed throughout this sample as both hydrocarbon and carbide. These carbon

species may be an artifact of sample preparation, with sputter reduction causing carbide to pile up at the metal-on-oxide interfaces.

### **Investigation of Varied Dielectrics**

Zirconium oxide sulfate and hafnium oxide sulfate solutions were used to produce laminates with ZrCuAlNi in order to investigate the diversity of interfacial-reaction chemistries. It is hypothesized that because the Zirconium in the ZrCuAlNi-AMMF is capable of reducing phosphate species, the more favorable reduction of sulfur should occur in sulfate-containing systems. The Zirconium oxide sulfate (ZircSO<sub>x</sub>) solution also allows further probing of the involvement of Le Chatelier's Principle on these reactions by having a concentration of Zr(IV) already present in the films.

100-nm ZircSO<sub>x</sub> and HafSO<sub>x</sub> films were deposited on thermally oxidized silicon and heated to 300° C in order to take XPS depth profiles for a baseline of composition. Reduced sulfur and M(IV), with M as Zr or Hf, oxides are measured throughout both systems. The hafnium and zirconium-based samples without amorphous metal in Figure 3.7 show all of the sulfur present as the reduced sulfide species, also indicating that the greater reducibility of the sulfate species in this measurement. All previous studies have posited the sulfur as present in the form of oxygen-coordinated, and multiple measurements have indicated the sulfur present in the material to be from sulfate.<sup>9,14,16</sup> Sulfur concentrations, ignoring oxidation, are found to be similar to those measured by microprobe analysis on doped-HafSO<sub>x</sub> systems.<sup>9</sup> Although sulfur appears to be heavily photosensitive to the x-rays used to measure the system, laminates of the

system still demonstrate interesting chemical effects in both the XPS profiles and the TEM images.

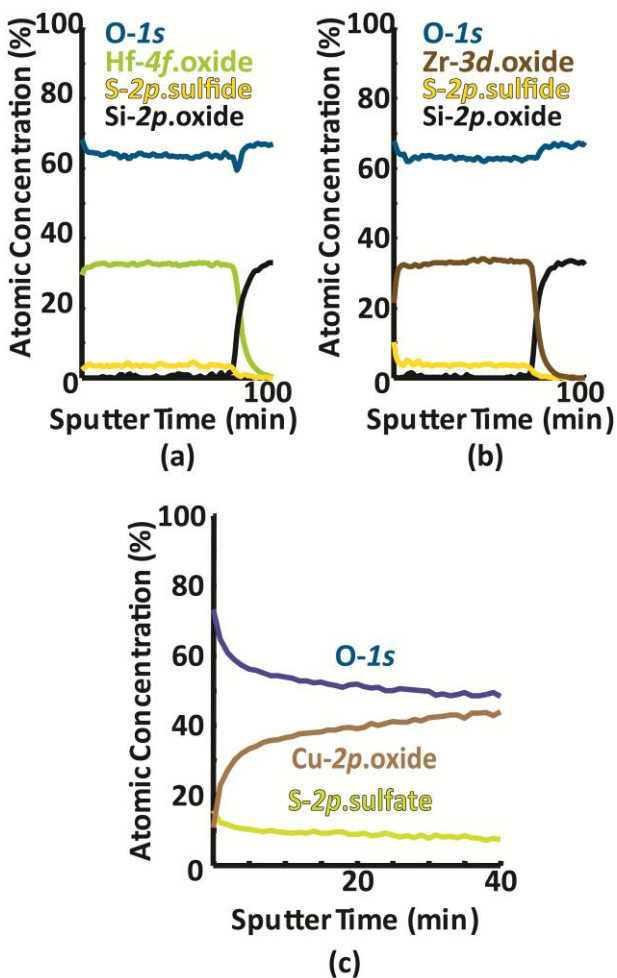


Figure 3.7: (a) XPS depth profile of 100-nm HafSO<sub>x</sub> film. (b) XPS depth profile of 100-nm ZircSO<sub>x</sub> film. (c) XPS depth profile of crystalline copper sulfate.

Figure 3.7 demonstrates that hafnium and zirconium sulfate films generate sulfide-shifted photoelectron energies while hydrated copper sulfate is incapable of creating the same phenomenon. This measurement mirrors those in Figure 3.3 and Figure 3.4 in which titanium is capable of causing the measurement of phosphide while copper is not. It is important to note that copper can be measured with sulfate in an oxidized form. In

laminated systems, all of the sulfate is still converted into sulfide during photoexposure, however photoelectron spectra indicate three distinct photoelectron energies for the Zr.

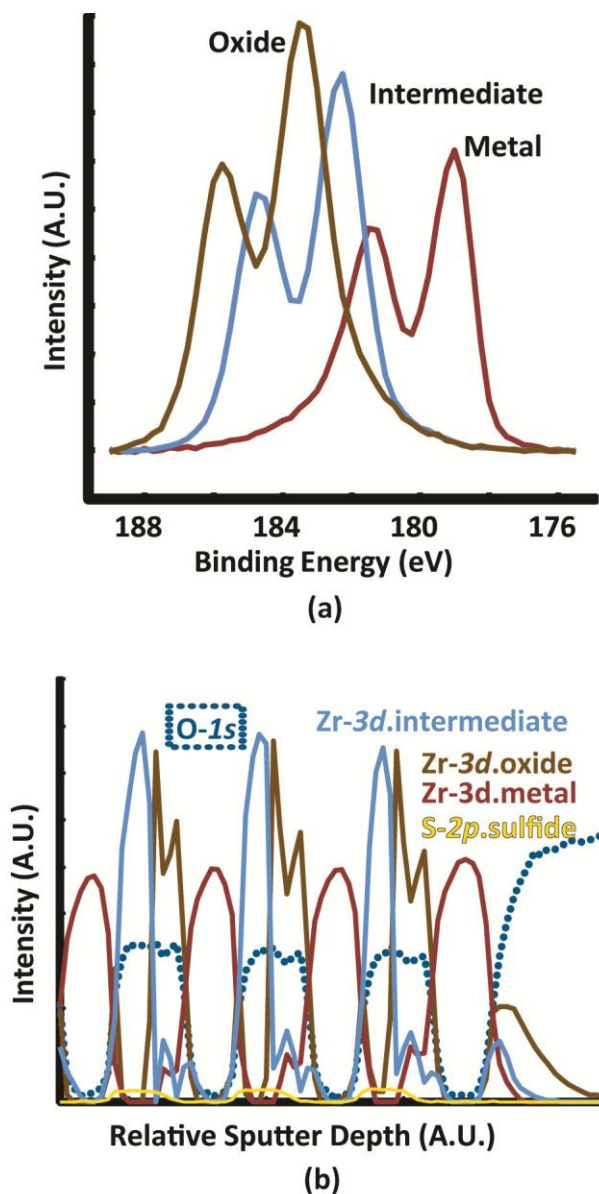
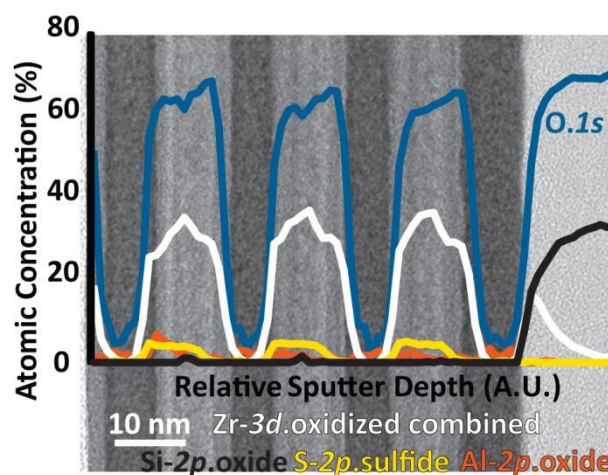


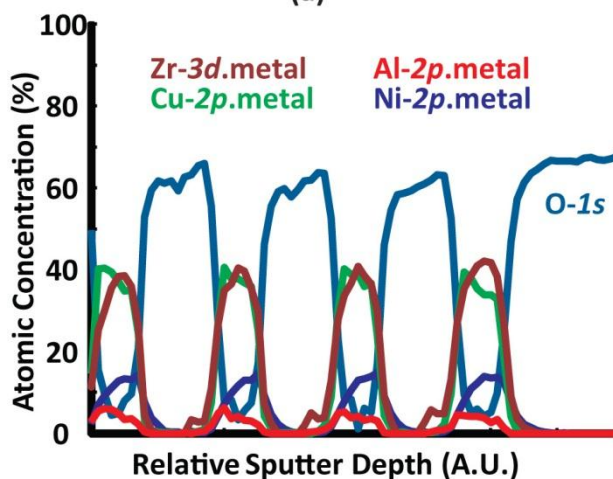
Figure 3.8: (a)Graph of Zirconium-photoelectron binding energies resolved from laminated structure. (b) Corresponding intensity vs. depth profile of laminate with the various species of zirconium present labeled.

Photoelectron binding-energy evaluations presented in Figure 3.8 show a zirconium state between that of the oxide and the metal. It is hypothesized that these

photoelectrons correspond to a sulfur-coordinated zirconium because the shift in binding energy presented in Figure 3.8(a) corresponds to coordination to a less electronegative anion than oxygen, and sulfur is the only other species present in the film. Zirconium oxide sulfide species have also been reported in literature<sup>30</sup>, lending credence to this hypothesis.



(a)

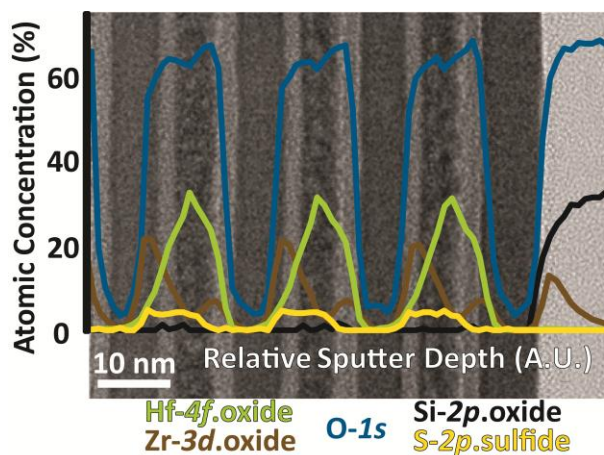


(b)

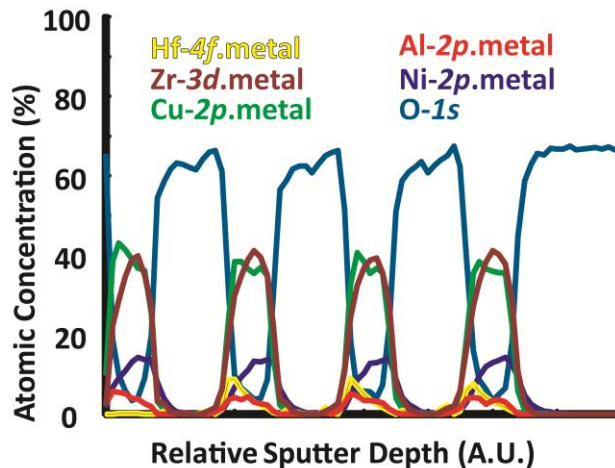
Figure 3.9: (a)TEM micrograph of ZrCuAlNi-ZircSOx laminated structure with XPS depth-profile overlay showing all oxidized metals present, as well as oxide and sulfide concentrations . (b) Corresponding XPS depth profile of metals from laminate accompanied by  $O^{2-}$  to allow for spatial scaling.

Figure 3.9 presents a TEM micrograph of a ZircSO<sub>x</sub>/ZrCuAlNi AMMF laminate with an overlaid XPS spectrum of O<sup>2-</sup>, Si<sup>4+</sup>, S<sup>2-</sup> and Zr<sup>4+</sup>. A change in image contrast is seen roughly at the location of the change in Zr oxidation state illustrated in Figure 3.9(b). The domain growth associated with the oxidation state change corresponds to a drop in oxide concentration. Maximum sulfide concentrations are observed in the middle of the ZircSO<sub>x</sub> layer. It is difficult to know how far the oxygen content decreases in the center due to the extremely-small, lateral feature sizes involved in the measurement, however the TEM indicates approximately 5 nm of darkening in the center of the film.

Being that the top and bottom surfaces of the oxide are dominated by ZrO<sub>2</sub>, it is reasonable to believe that there is sulfide concentration in the center. Also, the repeatable dips in oxygen anion concentration measured in the center of the oxide film whilst there is concurrent increase in cationic concentration is indicative that some part of the sulfide measured is consistent with the composition. Further measurements of the corollary system with Hafnium have far greater contrast in their imaging, dramatically emphasizing the reactions taking place.



(a)



(b)

Figure 3.10: (a) TEM micrograph of ZrCuAlNi-HafSO<sub>x</sub> laminated structure with XPS depth-profile overlay showing all oxidized metals present, as well as oxide and sulfide concentrations. (b) Corresponding XPS depth profile of metals from laminate accompanied by O<sup>2-</sup> to allow for spatial scaling.

The TEM micrograph in Figure 3.10(a) illustrates clear segregation of the heavier atomic species to the center of the HafSO<sub>x</sub> layer, as well as early domain formation in the middle section of the HafSO<sub>x</sub> film. The domain growth corresponds to a drop in oxide concentration at the center of the dielectric that is repeated in three successive bilayers. The contrast associated with this reaction is more obvious in the TEM images.

Maximum sulfide concentrations are measured in the middle of the  $\text{HfSO}_x$  layer where the oxide concentration drops while the  $\text{Hf(IV)}$  concentration maximizes. The location of the peak sulfide concentrations is congruent with sulfide measurements from the  $\text{ZrSO}_x$  laminate. The small amount of the  $\text{Hf}^{4+}$  measured as reduced to Hf metal which has displaced into the AMMF layers as an artifact of measurement.<sup>31</sup>

Even though there are definite chemical reactions and domain formations occurring within these  $\text{MSO}_x$  systems when amorphous metal is deposited on top of them, their overall smoothness appears to be largely dominated by the method in which they were deposited, making incredibly uniform layers of the subsequent reaction products. To be more clear, with these deposition methods the smoothness of the final system appears to be dictated by the smoothness of the precursor films, even if interfacial reactions present themselves.

Both systems show oxygen being preferentially removed from the metals with the hafnium system clearly showing via TEM that the zirconium atoms take their oxygen from the relatively well-hydrated oxide sulfate films. The Z contrast from the TEM image of the ZCAN system with the hafnium oxide sulfate system makes it evident that heavier metal cations are concentrating at the center of the film while a smaller-z metal is concentrating other low-z species at the outside of the material. These observations work in conjunction with the expected dehydration reaction listed in equation 1. Oxygen profiles shown in Figure 3.12 also show a decrease toward the middle of the dielectric film.

## Conclusions

Incredibly uniform, chemically controllable, repeatable laminated metal-dielectric materials can be easily and inexpensively fabricated in the nanoscale by using amorphous metal and solution-processed aluminum oxide phosphate glass. The materials and the methods used to deposit them play a large role in what chemistry happens at the solid-state interface between the two materials. Surface reactions in laminated structures provide valuable insight into the considerations that will need to be made in both measurement and production as optical and electronic device structures require extremely nano-scaled, and vertically-stacked structures.

Native-surface-oxide studies offer important information about how electropositive substrates will react with water-based, solution-processed oxide films as well as ambient processing conditions. Deposition-based interactions with the solution-processed, amorphous oxide films have been addressed both in terms of the novel interfacial chemistries that they produce. The intermixing of interfaces implies that proper modeling of these systems may be carried out as a wave instead of a step function of composition. The chemical gradation of these interfaces offers a new method of modeling systems and allowing for ultra-consistent transitions between unlike materials. Further optical characterization and electrical characterization is required to define the effects of the interface on properties like dielectric constant and index of refraction in these material sets.

The chemistries are observed to be contingent upon the concentrations of reducible species in the amorphous oxide bulk matrix; and the reactions are dependent upon the

electropositivities of the metals being sputter-deposited upon the oxides. This study offers the insight into a method of tailoring interdiffusion via stoichiometric choice of amorphous metal and oxide material, as well as insight into allowable ordering of deposition for specific material sets. Characterization of amorphous-metal-composition-based interdiffusion through the sputtering of a top contact is necessary because the work offers a plausible method of creating controlled, graded, asymmetric dielectrics in the nanometer scale. Understanding the underlying causes of this chemical gradation offers an opportunity to engineer the asymmetry of diode responses to bias in metal-insulator-metal devices.

## References

- (1) Hoffman, A. J.; Alekseyev, L.; Howard, S. S.; Franz, K. J.; Wasserman, D.; Podolskiy, V. A.; Narimanov, E. E.; Sivco, D. L.; Gmachl, C. *Nat. Ma* **2007**, *6*, 946-950.
- (2) Cowell, E. W.; Alimardani, N.; Knutson, C. C.; Conley, J. F.; Keszler, D. A.; Gibbons, B. J.; Wager, J. F. *Adv. Mater.* **2011**, *23*, 74-78.
- (3) Dolan, M.; Dave, N.; Morpeth, L.; Donelson, R.; Liang, D.; Kellam, M.; Song, S. *J. Membr. Sci.* **2009**, *326*, 549-555.
- (4) Mulas, G.; Schiffini, L.; Scudino, S.; Cocco, G. *Journal of Alloys and Compounds* **2008**, *454*, 83-88.
- (5) Tawarayama, H.; Hosono, H.; Yamaura, S.-ichi; Zhang, W.; Inoue, A. *Chem. Lett.* **2009**, *38*, 502.
- (6) Hara, S.; Sakaki, K.; Itoh, N.; Kimura, H. M.; Asami, K.; Inoue, A. *J. Membr. Sci.* **2000**, *164*, 289-294.
- (7) Cowell III, E. W.; Knutson, C. C.; Wager, J. F.; Keszler, D. A. *ACS* **2010**, *2*, 1811-1813.
- (8) Pilkington, L. A. B. *Proc. R. Soc. Lond. A* **1969**, *314*, 1-25.
- (9) Anderson, J. T.; Munsee, C. L.; Hung, C. M.; Phung, T. M.; Herman, G. S.; Johnson, D. C.; Wager, J. F.; Keszler, D. A. *Adv. Funct. Mater.* **2007**, *17*, 2117-2124.
- (10) Munsee, C. Characterization of solution-based inorganic semiconductor and dielectric materials for inkjet printed electronics. EECS, Oregon State University: Corvallis, OR, 2005.
- (11) Jiang, K.; Anderson, J. T.; Hoshino, K.; Li, D.; Wager, J. F.; Keszler, D. A. *Chem. Mater.* **2011**, *23*, 945-952.
- (12) Jiang, K.; Zakutayev, A.; Stowers, J.; Anderson, M. D.; Tate, J.; McIntyre, D. H.; Johnson, D. C.; Keszler, D. A. *Solid State Sciences* **2009**, *11*, 1692-1699.
- (13) Meyers, S. T.; Anderson, J. T.; Hong, D.; Hung, C. M.; Wager, J. F.; Keszler, D. A. *Chem. Mater.* **2007**, *19*, 4023-4029.

- (14) Telecky, A.; Xie, P.; Stowers, J.; Grenville, A.; Smith, B.; Keszler, D. A. *J. Vac. Sci. Technol. B* **2010**, *28*, C6S19.
- (15) Mensinger, Z. L.; Gatlin, J. T.; Meyers, S. T.; Zakharov, L. N.; Keszler, D. A.; Johnson, D. W. *Angew. Chem.* **2008**, *120*, 9626-9628.
- (16) Stowers, J.; Keszler, D. A. *Microelectron. Eng.* **2009**, *86*, 730-733.
- (17) Jiang, K.; Zakutayev, A.; Stowers, J.; Anderson, M. D.; Tate, J.; McIntyre, D. H.; Johnson, D. C.; Keszler, D. A. *Solid State Sci.* **2009**, *11*, 1692-1699.
- (18) Sharma, P.; Zhang, W.; Amiya, K.; Kimura, H.; Inoue, A. *J. Nanosci. Nanotechnol.* **2005**, *5*, 416-420.
- (19) Inoue, A.; Nishiyama, N. *MRS Bull.* **2007**, *32*, 651-658.
- (20) Greer, A. L.; Ma, E. *MRS Bull.* **2007**, *32*, 611-619.
- (21) Paillier, J.; Mickel, C.; Flaviu Gostin, P.; Gebert, A. *Mater. Charact.* **2010**, *61*, 1000-1008.
- (22) Padhy, N.; Ningshen, S.; Kamachi Mudali, U. *J. Alloy Compd.* **2010**, *503*, 50-56.
- (23) Ningshen, S.; Kamachi Mudali, U.; Krishnan, R.; Raj, B. *Surf. Coat. Technol.* **2011**, *205*, 3961-3966.
- (24) Grubbs, M.; Zhang, X.; Deal, M.; Nishi, Y.; Clemens, B. M. *Appl. Phys. Lett.* **2010**, *97*, 223505.
- (25) Xiao, S.; Chettiar, U. K.; Kildishev, A.; Drachev, V.; Shalaev, V. *Opt. Lett.* **2009**, *34*, 3478-3480.
- (26) Doan, N.; Kontturi, K.; Johans, C. *Journal of colloid and interface science* **2010**, *350*, 126-131.
- (27) Zhou, L.; Rai, A.; Piekiet, N.; Ma, X.; Zachariah, M. R. *J. Phys. Chem. C* **2008**, *112*, 16209-16218.
- (28) Kasper, N.; Stierle, A.; Nolte, P.; Jin-Phillipp, Y.; Wagner, T.; de Oteyza, D. G.; Dosch, H. *Surf. Sci.* **2006**, *600*, 2860-2867.
- (29) Wang, C. M.; Baer, D. R.; Amonette, J. E.; Engelhard, M. H.; Anthony, J. J.; Qiang, Y. *Ultramicroscopy* **2007**, *108*, 43-51.

(30) Eastman, E.; Brewer, L.; Bromley, L. R. A.; Gilles, P. W.; Lofgren, N. L. *J. Am. Chem. Soc.* **1951**, *73*, 3896–3898.

(31) Feldman, L. *Fundamentals of Surface and Thin Film Analysis*; Prentice Hall, Inc.: Englewood Cliffs, New Jersey, 1986.

## Chapter 4

### SPUTTER-COATED PASSIVATION OF ZINC TIN OXIDE

Christopher C. Knutson, Rick E. Presley, Ram Ravichandran, Robert Kykyneshi, Eric  
S. Sundholm, Bao Yeh, Randy L. Hoffman, Devin A Morrey, John F. Wager, John  
Robertson, Douglas A. Keszler

To be published in *ACS Applied Materials & Interfaces*

**Introduction:**

Zinc tin oxide (ZTO) has shown promise as a transparent semiconductor in high-performance transistor applications<sup>1-3</sup>. The components are low-cost, easy to process, abundant in the Earth's crust, and are optically transparent. ZTO channel layers show strong dependence upon processing, and surface states making them a challenge to manufacture reliably<sup>4-7</sup>. ZTO is sensitive to ambient conditions such that it can be used in sensory applications, therefore requiring passivation in TFT applications<sup>8</sup>. Passivation utilizing RF sputtering has not previously been reported to our knowledge.

Early passivation studies for ZTO centered around low kinetic energy deposition methods in order to leave the surface of the channel undamaged<sup>9-11</sup>. Current ZTO low kinetic energy passivation techniques (i.e., atomic layer deposition and thermal evaporation) do not easily scale to most large-area glass manufacturing.

Sputtered films are economically viable, commonly processed in industry, and easily scalable to large-area applications. Sputter-deposited ZTO and indium tin oxide (ITO) have been successfully utilized in transparent electronic devices<sup>2,5,12</sup>. However, the electronic sensitivity of the ZTO surface to atomic implantation and oxygen concentration usually require passivating layers to be deposited by low energy deposition methods. Energetic deposition methods (i.e. sputtering) offer benefits of manufacturability but fundamental challenges of interfacial chemical implantation.

In light of recently observed amorphous interfacial reactions<sup>13</sup>, it is hypothesized that a target composition may be designed such that it can be sputter deposited onto ZTO

channels without drastically changing oxygen concentration or overall chemical composition of the ZTO. This barrier layer allows for consistent electronic performance while acting as a platform for further passivation. Chemical design of the barrier material also requires that the final deposited passivation stack (i.e., barrier layer plus passivation layer) be insulating at the operational field intensities of the device. The barrier material must also be developed from earth-abundant elements for cost purposes and optically transparent to fit into the niche of transparent devices. Zinc tin silicon oxide (ZTSO) is a low-cost, easily producible, environmentally benign target composition that accomplishes all necessary tasks for the barrier layer, which enables ZTO passivation.

This study addresses the chemistry occurring at the interface between the barrier and the channel layers. These interfaces are characterized and compared as deposited and after the barrier layer post deposition anneal. Electrical measurements verify the capabilities of the barrier layer with further verification carried out through the addition of a plasma-enhanced-chemical-vapor deposition (PECVD) SiO<sub>2</sub> passivation layer.

### **A Framework for Assessing Passivation**

The goal of this subsection is to describe a simple and yet general framework from which to discuss passivation. This approach constitutes an extension of our previous induced gap state modeling efforts<sup>14-17</sup>.

Figure 4.1: Equilibrium energy band diagrams illustrating an undesirable passivation scheme. (a) An ideal metal-insulator-semiconductor (MIS) thin-film stack and a passivation layer (P) are shown in isolation from one another, prior to interface formation. The charge neutrality level of the passivation layer ( $E_{\text{CNLP}}$ ) is positioned lower in energy than that of the semiconductor charge neutrality level ( $E_{\text{CNLS}}$ ). Therefore, electronic charge transfer occurs from  $E_{\text{CNLS}}$  to  $E_{\text{CNLP}}$  (right-going arrow). (b) This electronic charge transfer results in the formation of a positive dipole (upward arrow). The dipole voltage drops across both the semiconductor and the insulator. This passivation scheme is undesirable since the direction of electronic charge transfer leads to the formation of an accumulation layer at the semiconductor / passivation layer interface.

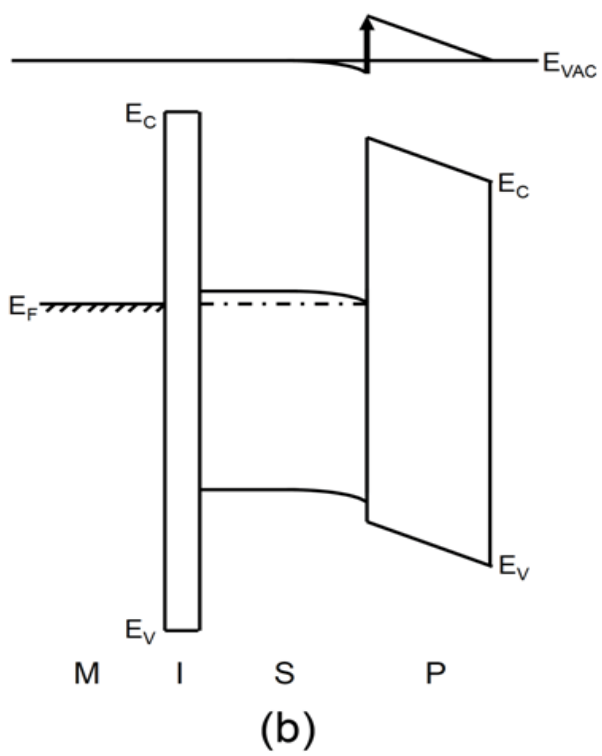
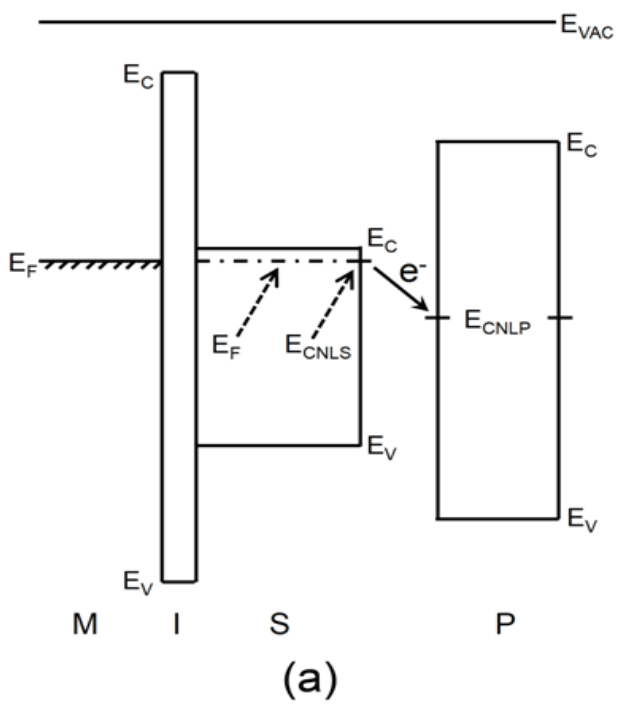


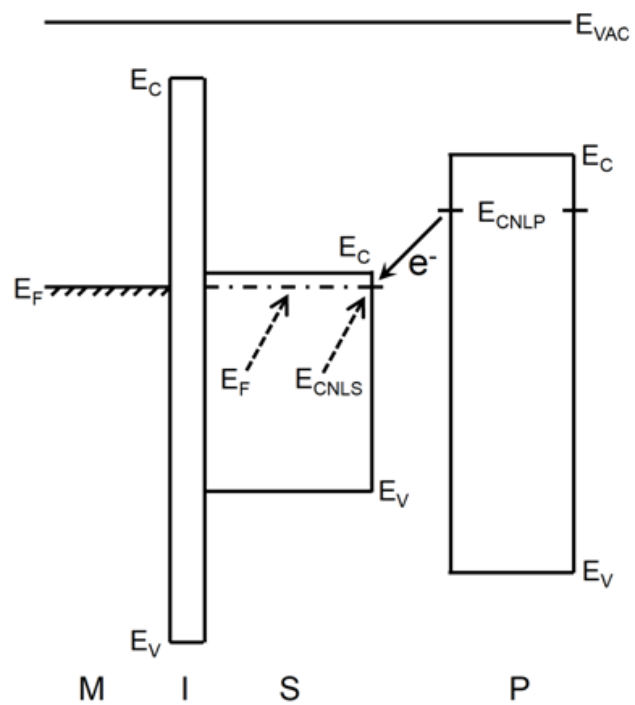
Figure 4.1 presents equilibrium energy band diagrams illustrating an undesirable passivation scheme. An *ideal* metal-insulator-semiconductor (MIS) thin-film stack is covered with a passivation layer (P). The MIS thin-film is *ideal* because both the insulator and semiconductor bands are flat and, also, the semiconductor Fermi level is positioned precisely at the semiconductor charge neutrality level energy,  $E_{\text{CNLS}}$ . These *ideal assumptions* allow us to concentrate exclusively on the physics and chemistry of interface formation between the semiconductor and the passivation layer.

Invoking the concept of a charge neutrality level is key to this assessment procedure. In terms of interface formation, a charge neutrality level may be envisaged as a Fermi level for interface states<sup>18</sup>. The charge neutrality level corresponds to the energy above (below) which electronic states at an interface are negatively (positively) charged when filled with electrons. When a semiconductor and a passivating insulator are brought into intimate contact, electronic charge transfer occurs between charge neutrality levels, giving rise to the formation of an interfacial dipole.

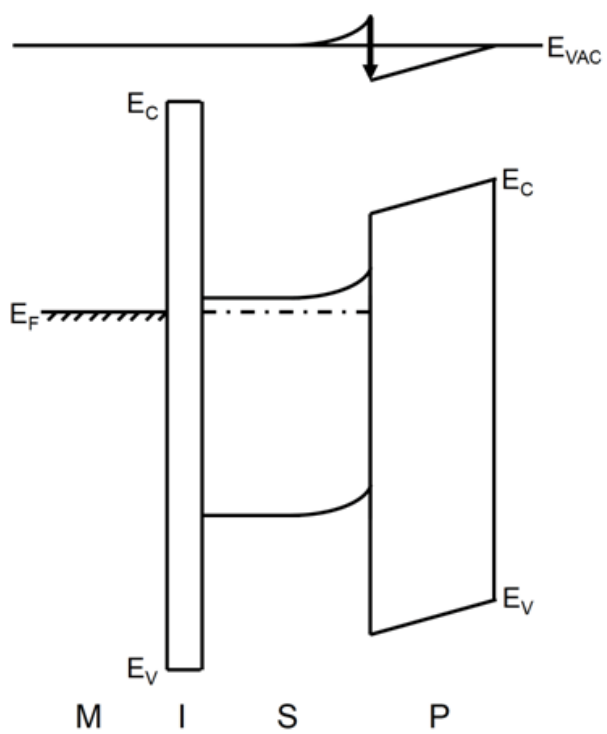
According to Figure 4.1(a), the charge neutrality level of the passivation layer ( $E_{\text{CNLP}}$ ) is positioned lower in energy than  $E_{\text{CNLS}}$  so that electronic charge transfer occurs from  $E_{\text{CNLS}}$  to  $E_{\text{CNLP}}$  (right-going arrow). This electronic charge transfer results in the formation of a positive dipole (upward arrow of Figure 4.1(b)). The dipole voltage drops across both the semiconductor and the insulator. This passivation scheme is undesirable since the direction of electronic charge transfer leads to the formation of an accumulation layer at the semiconductor / passivation layer interface. The presence of

an accumulation layer at this interface will result in a strong shift to the left in the turn-on voltage of a  $\log(I_D)$ - $V_{GS}$  transfer curve of a TFT since a large negative gate voltage is required to deplete electrons from this accumulation layer. Note that it is difficult to eliminate this accumulation layer via application of a gate voltage since it is present at the backside interface, remote from the gate.

Figure 4.2: Equilibrium energy band diagrams illustrating a desirable passivation scheme. (a) An ideal metal-insulator-semiconductor (MIS) thin-film stack and a passivation layer (P) are shown in isolation from one another, prior to interface formation. The charge neutrality level of the passivation layer ( $E_{\text{CNLP}}$ ) is position higher in energy than that of the semiconductor charge neutrality level energy ( $E_{\text{CNLS}}$ ). Therefore, electronic charge transfer occurs from  $E_{\text{CNLP}}$  to  $E_{\text{CNLS}}$  (left-going arrow). (b) This electronic charge transfer results in the formation of a negative dipole (downward arrow). The dipole voltage drops across both the semiconductor and the insulator. This passivation scheme is desirable since the direction of electronic charge transfer leads to the formation of a depletion layer at the semiconductor / passivation layer interface.



(a)



(b)

In contrast, Figure 4.2 shows equilibrium energy band diagrams illustrating a desirable passivation scheme.  $E_{\text{CNLP}}$  is positioned higher in energy than  $E_{\text{CNLS}}$  so that electronic charge transfer occurs from  $E_{\text{CNLP}}$  to  $E_{\text{CNLS}}$  (left-going arrow, Figure 4.2(a)), giving rise to a negative dipole (downward arrow, Figure 4.2(b)), and the formation of a depletion layer at the semiconductor / passivation layer interface. Note that in this case an undesirable accumulation layer is not present at the back interface so that the gate voltage controls electron accumulation exclusively at the front interface.

In summary, an appropriate passivation layer will tend to have an  $E_{\text{CNLP}}$  that is either aligned with or is positioned higher in energy than  $E_{\text{CNLS}}$ . This condition ensures that an electron accumulation layer will not be present at the channel backside interface.

## **PASSIVATION OF ZTO AND IGZO**

The objective of this subsection is to explore possible mechanisms responsible for ZTSO passivation of ZTO and IGZO using the passivation framework introduced previously.

In order to employ the modeling approach developed in the previous subsection, charge neutrality levels for ZTO, IGZO, and ZTSO must be estimated. This is accomplished, as summarized in Table 4.1, by simple averaging of constituent oxide values. The charge neutrality level is estimated to be 4.2, 4.4, and 4.7 V below the vacuum level for ZTO, IGZO, and ZTSO, respectively. These estimates suggest that there is very little charge neutrality level misalignment between ZTSO and ZTO or

IGZO. Thus, ZTSO is expected to effectively passivate ZTO and IGZO in terms of avoiding the formation of an electron accumulation layer at the back surface.

The bandgaps included in Table 4.1 for ZTO, IGZO, and ZTSO are obtained via the same simple averaging procedure used to estimate their charge neutrality levels. From spectroscopic ellipsometry, the measured bandgaps of ZTO, IGZO, and ZTSO are found to be 3.5, 3.2, and 3.6 eV, respectively. Thus, the averaging procedure used in Table 4.1 has overestimated the bandgap of IGZO and ZTSO by 0.4 and 1.7 eV, respectively, while it is in agreement with that of ZTO. This result suggests that the ZTO and IGZO charge neutrality level misalignment with respect to ZTSO may be even smaller than given in Table 4.1.

Since the measured bandgaps of ZTO and ZTSO are so similar, a negligible conduction band discontinuity is expected to be present at the ZTO/ZTSO interface, in contrast to the passivation cases sketched in Figures 4.1(b) and 4.2(b). Electrically, the ZTSO layer is found to be ‘dead’. That is, if a gate is deposited onto a ZTSO surface and a positive gate voltage is applied to this gate, the electrons induced into this ZTSO channel are found to have a negligibly small mobility. Thus, ZTSO passivation appears to involve avoiding the formation of a back channel electron accumulation layer at the ZTO/ZTSO interface and, furthermore, suppressing back channel conduction in the ZTSO due to the poor electrical quality of this layer.

A large semiconductor/passivation layer conduction band discontinuity, such as that sketched in Figures 4.1(b) and 4.2(b), would appear to be attractive for passivation since

electrons in the semiconductor would see an energy barrier that it would tend to confine them within the semiconductor. Four wide bandgap insulators, whose charge neutrality levels have been estimated, are included at the bottom of Table 4.1 as candidate passivation layers. The large charge neutrality level energies of  $\text{SiO}_2$  and  $\text{Y}_2\text{O}_3$  are unattractive from a passivation perspective since they lead to the undesirable passivation scheme shown in Figure 4.1. The charge neutrality level positioning of  $\text{HfO}_2$  and especially  $\text{Al}_2\text{O}_3$  are more promising for passivation. Indeed, we have had some success employing sputtered  $\text{Al}_2\text{O}_3$  as a passivation layer. However, development of a reliable, robust, and reproducible sputtered  $\text{Al}_2\text{O}_3$  passivation process appropriate for commercial applications remains an elusive goal. Even though the  $\text{HfO}_2$  charge neutrality level position appears suitable for ZTO and IGZO passivation, the high- $k$  nature  $\text{HfO}_2$  of makes it less attractive for passivation layer applications.

The wide bandgap insulators included in Table 4.1 – i.e.,  $\text{SiO}_2$ ,  $\text{Al}_2\text{O}_3$ ,  $\text{HfO}_2$ , and  $\text{Y}_2\text{O}_3$  – all have a strong tendency to oxidize, as revealed by their large Gibbs free energy of formation compared to that of the ZTO and IGZO constituent oxides – i.e.,  $\text{ZnO}$ ,  $\text{SnO}_2$ ,  $\text{In}_2\text{O}_3$ , and  $\text{Ga}_2\text{O}_3$ . This can lead to problems when trying to passivate ZTO or IGZO using these wide bandgap insulators since competition for oxygen between Si, Al, Hf, or Y and Zn, Sn, In, or Ga could lead to a reduction of the ZTO or IGZO surface. Such a loss of oxygen from the semiconductor surface, which can be modeled as a decrease in the semiconductor charge neutrality level position, is particularly problematic when strongly reducing process gases are used, e.g., silane in plasma-enhanced chemical vapor deposition (PECVD) of  $\text{SiO}_2$  or trimethylaluminum in atomic layer deposition of

$\text{Al}_2\text{O}_3$ . Although it is possible to circumvent these sort of problems associated with strongly reducing precursors using alternative deposition methods such as sputtering and pulsed laser deposition (PLD), sputtered dielectrics tend to crystallize while PLD dielectrics are difficult to prepare as particulate-free uniform coatings that are fully dense. Passivation layers with grain boundaries, poor density, and/or film porosity often exhibit promising electrical TFT properties since the semiconductor surface is effectively still in contact with air. Air exposure leads to a depleted backside surface. However, it is unlikely that such a low density passivation layer will provide suitable passivating properties for a commercial product.

### **PASSIVATION OF ZTO AND IGZO: QUANTITATIVE ASSESSMENT**

The framework for assessing passivation presented herein may be formulated quantitatively via induced gap states modeling<sup>14-17</sup>. The dipole voltage (i.e., the arrows shown in Figs. 1b and 2b),  $\Delta_{PS}$ , is equal to  $\Phi$

$$(1) \quad \Delta_{PS} = (1 - S_{PS})[\Phi_{CNLP} - \Phi_{CNLS}],$$

where  $S_{PS}$  is a passivation insulator-semiconductor interface parameter given by

$$(2) \quad S_{PS} \approx \frac{1}{1+0.1 \left[ \frac{(\epsilon_{\infty PR}-1)^2 (\epsilon_{\infty SR}-1)^2}{(\epsilon_{\infty PR}-1)^2 \left( \frac{C_{IP}}{C_{IP}+C_{IS}} \right) + (\epsilon_{\infty SR}-1)^2 \left( \frac{C_{IS}}{C_{IP}+C_{IS}} \right)} \right]},$$

where  $\epsilon_{\infty PR}$  and  $\epsilon_{\infty SR}$  are the high-frequency relative dielectric constants of the passivation insulator and semiconductor, respectively. The dipole capacitance densities included in Eq. (2) are specified by

$$(3) \quad C_{iS} = \frac{\epsilon_{\infty S}}{d_{iS}}, \quad C_{iP} = \frac{\epsilon_{\infty P}}{d_{iP}},$$

where  $\epsilon_{\infty P}$  ( $\epsilon_{\infty S}$ ) and  $d_{iP}$  ( $d_{iS}$ ) are the high-frequency dielectric constant and dipole layer thickness, respectively, for the passivation insulator (semiconductor). For quantitative analysis, the dipole layer thickness is always taken to be 0.4 nm<sup>17</sup>.

Another aspect of passivation is control of the interface state density. According to induced gap state modeling, the interface state density of a passivated surface is equal to

$$(4) \quad D_{PS} = \frac{1}{q} \left( \frac{C_{iP}C_{iS}}{C_{iP}+C_{iS}} \right) \left( \frac{1}{S_{PS}} - 1 \right),$$

while the surface state density of an unpassivated surface is given by

$$(5) \quad D_{SS} = \frac{C_i}{q} \left( \frac{1}{S} - 1 \right),$$

where  $C_i = \epsilon_{\infty} / d_i$  is dipole capacitance density for the semiconductor or insulator of interest and

$$(6) \quad S = \frac{1}{1+0.1(\epsilon_{\infty R}-1)^2},$$

is the interface parameter for the material surface of interest and  $\epsilon_{\infty R}$  is its corresponding high-frequency relative dielectric constant.

Table 4.2 summarizes the high-frequency relative dielectric constant ( $\epsilon_{\infty R}$ ), interface parameter for a surface (S), and surface state density ( $D_{SS}$ ) for selected semiconductors and insulators of relevance to this discussion of ZTO and IGZO passivation. Notice that  $D_{SS}$  is determined by  $\epsilon_{\infty R}$ . A small  $\epsilon_{\infty R}$  is desirable since it leads to a smaller surface

state density. The covalent semiconductors silicon and germanium are included in this table to underscore the fact that surface state densities of ZTO and IGZO are approximately two orders of magnitude smaller than that of a covalent semiconductor.

Table 4.3 reveals several interesting and surprising passivation trends.

First, consider the last entry in Table 4.3, involving a Si surface passivated by SiO<sub>2</sub>. Remarkably, the interface state density ( $D_{PS}$ ) of a SiO<sub>2</sub>-passivated Si surface is reduced by a factor of 416 compared to that of the surface state density of an unpassivated Si surface ( $D_{SS}$ , Table 4.2). This occurs because the Si/SiO<sub>2</sub> interface state density arises as a series combination of the Si and the SiO<sub>2</sub> surface state capacitances. Since these capacitances add in series, the smaller capacitance dominates, especially when one capacitance is much smaller than the other. Next, note that the interface dipole voltage is  $\Delta_{PS} = 0.10$  V for the Si/SiO<sub>2</sub> interface. According to Eq. (1),  $\Delta_{PS}$  is given by a product of a capacitive screening term ( $1-S_{PS}$ ) and a charge neutrality level misalignment term ( $\Phi_{CNLP}-\Phi_{CNLS}$ ). At first glance,  $\Delta_{PS}$  might be expected to be large since the misalignment term is rather large (0.7 V). However, the actual value of  $\Delta_{PS}$  is actually quite small since the interface parameter ( $S_{PS}$ ) is very large (0.84). This very large value for  $S_{PS}$  is, once again, a consequence of the addition of series capacitances with one capacitance being very small.

These same considerations apply to the passivation of ZTO and IGZO, although in a less extreme fashion since  $D_{SS}$  is smaller for these two oxide semiconductors than for Si. Comparing ZTO and IGZO passivation by ZTSO, SiO<sub>2</sub>, or Y<sub>2</sub>O<sub>3</sub>, SiO<sub>2</sub> has the

advantage of having the smallest interface state density ( $D_{PS}$ ). However, the interface dipole voltage ( $\Delta_{PS}$ ) is a more important consideration with respect to passivation. A large value of  $\Delta_{PS}$ , such as that obtained when  $Y_2O_3$  is used to passivate ZTO or IGZO (i.e., 0.52 V for ZTO and 0.53 V for IGZO), cannot be tolerated since it will result in a strong backside electron accumulation layer. Surprisingly, even though the charge neutrality level misalignment is very large for  $SiO_2$  passivation of ZTO or IGZO compared to ZTSO (i.e., 1.2 V for ZTO/ $SiO_2$  and 1.0 V for IGZO/ $SiO_2$  compared to 0.5 V for ZTO/ZTSO and 0.3 V for IGZO/ZTSO),  $\Delta_{PS}$  is almost identical for ZTSO or  $SiO_2$  passivation of ZTO or IGZO. This occurs because  $S_{PS}$  for  $SiO_2$  passivation is significantly larger than for ZTSO passivation.

These quantitative induced gap states modeling considerations lead us to suspect that electron accumulation layer problems associated with  $SiO_2$  passivation of ZTO or IGZO are probably not associated with *intrinsic* interface states (i.e., evanescent electronic states within the bandgap or induced gap states). Rather, they are more likely due to *extrinsic* interface state generation arising from reactive gas reduction of the ZTO or IGZO surface or, alternatively, hydrogen doping during PECVD of  $SiO_2$ .

In summary, ZTSO passivation of ZTO and IGZO appears to involve: (i) avoiding the formation of a back channel electron accumulation layer at the ZTO/ZTSO interface because of a small charge neutrality level misalignment, (ii) suppression of back channel conduction in the ZTSO due to the poor electrical quality of ZTSO, and (iii) avoiding oxygen reduction of the ZTO or IGZO surface by designing a passivation

layer (i.e., ZTSO) which is not strongly oxidizing, in contrast, for example, to SiO<sub>2</sub> or Y<sub>2</sub>O<sub>3</sub>. Additionally, our induced gap states modeling suggests that SiO<sub>2</sub> would be an excellent passivation layer for ZTO and IGZO if it could be deposited in such a manner to avoid oxygen reduction of the ZTO or IGZO surface.

## **Experimental:**

### **Target fabrication**

A 2" diameter ZTSO target is produced by combining a stoichiometric, 1:1:1 by metals mixture of zinc oxide (Cerac, 99.99%), tin dioxide (Cerac, 99.95%) and silicon dioxide (Cerac, 99.99%). The mixture is ground for two hours in an agate mortar and cold-compressed into a pellet under 150 atm of pressure. The pellet is transferred to an alumina crucible and heated to 1330 °C for 10 hours with a ramp rate of 4.4°C/min in a CM Rapid Temp Furnace . An Archimedes density of 94% is achieved using this method.

### **Film deposition:**

ZTO films are deposited using a 2" diameter target, purchased from Cerac, with a composition of Zn<sub>2</sub>SnO<sub>4</sub> [(ZnO)<sub>0.67</sub>(SnO<sub>2</sub>)<sub>0.33</sub>] via RF-magnetron sputtering. The films are deposited using 75 W RF power, a target to substrate distance of ~10 cm, a pressure of 5 mtorr, and a 22 sccm flow of process gas with a 9:1 ratio of Ar:O<sub>2</sub>. Films are then annealed in air at a ramp rate of 2 °C /min and a maximum temperature of 400 °C for 1 hr in a Neytech QEX furnace.

ZTSO films are deposited onto ZTO films via RF magnetron sputtering. The films are deposited using 80 W RF power, a target to substrate distance of ~10 cm, a pressure of 5 mtorr, and a 21 sccm flow of process gas with a 95:5 of Ar:O<sub>2</sub>. Films are then annealed in air at a ramp rate of 2 °C /min and a maximum temperature of 300 °C for 1 hr in a Neytech QEX furnace.

**Transmission electron microscope (TEM) interface analysis:**

Test films of ZTO and ZTSO are deposited as described above to thicknesses of ~50 nm and ~100 nm respectively, which are equivalent to TFT film thicknesses. TEM membranes are cut from the film stack and polished to a desired thickness of less than 100 nm using gallium ions in a FEI Helios Dual Beam Focused Ion Beam. Images and electron diffraction of the interfaces were taken using a FEI Titan 80-300 TEM.

**X-ray photoelectron spectroscopy depth profiling:**

Compositional depth profiles utilizing X-ray Photoelectron Spectroscopy (XPS) measurements were undertaken on blanket-stacks of films prepared in the same fashion as detailed above. XPS measurements were performed in a Physical Electronics Quanterra Scanning ESCA Microprobe with a focused monochromatic Al K $\alpha$  X-ray (1486.7 eV) excitation source. A 40 W, 200  $\mu$ m X-ray beam spot at the sample was utilized for measurements. Sputter depth profile data were acquired at grazing incidence with the samples at 20° relative to the detector. The Cu 2*p*<sub>3/2</sub> feature at 932.62  $\pm$  0.05 eV and Au 4*f* feature at 83.96  $\pm$  0.05 eV were used to calibrate the binding energy scale. A standard Quanterra ion gun was used to generate a 1 keV argon-ion

beam. The beam was rastered over a 3 mm x 3 mm area. Charging artifacts were minimized by collecting XPS data with 1 eV, 20  $\mu$ A electrons and low-energy  $\text{Ar}^+$  ions.

#### **X-ray diffraction:**

100 nm ZTSO films are deposited onto thermally oxidized silicon wafers (provided by HP Corvallis). X-ray measurements are performed using a Rigaku RAPID X-ray diffractometer using  $\text{Cu K}\alpha$  radiation. The cathode voltage is maintained at 50 kV with a 100 mA current.

#### **Ultraviolet and visible spectroscopic characterization:**

Transmission and reflection spectra were taken of 500 and 1200 nm films were deposited onto 1 mm-thick GM Associates Incorporated fused silica. The films were annealed to 400° C in a Neytech QEX furnace in air. Spectra were taken on an Ocean Optics UV-Vis (HR4000) Spectrometer with a Mikropack DH-2000-BAL hydrogen/deuterium source. Integration times of 3800  $\mu$ s to 100 ms were used. Wavelengths between 200 nm and 1100 nm were examined for this study, with primary focus being directed between 225 nm and 825 nm. Fringes in the spectra were used to determine sample thickness and index of refraction.

#### **Ellipsometric Characterization:**

Optical characterization of IGZO, ZTO and ZTSO films are performed using a variable angle spectroscopic ellipsometer (J.A. Woollam, VASE ®). Films of approximately 100 nm were deposited onto a thermally oxidized silicon wafers (provided by HP Corvallis), and subsequently annealed to 400 °C in a Neytech QEX

furnace.  $\Psi$  and  $\Delta$  spectra were acquired in the spectral range of 260-1500 nm at three angles of incidence ( $65^\circ$ ,  $70^\circ$  and  $75^\circ$ ) in steps of 10 nm to determine the film thickness, index of refraction, dielectric constant, and band gap.

#### **Thin film transistor (TFT) device fabrication and characterization:**

TFTs are fabricated using p-type silicon substrates (0.008-0.016  $\Omega$ -cm) with 100 nm of thermal oxide as the gate dielectric.  $\sim 50$  nm of ZTO is sputter deposited as previously described and patterned via a shadow mask. This deposition is followed by annealing in air using a ramp rate of 2  $^\circ\text{C}/\text{min}$  and a maximum temperature of 400  $^\circ\text{C}$  for 1 hr.  $\sim 200$  nm ITO source and drain contacts are deposited via RF sputtering (75 W, 5 mTorr, Ar,  $\sim 10$  cm substrate to target distance) and patterned via a shadow mask. The feature size of the TFT channel is 2000  $\mu\text{m}$  wide by 200  $\mu\text{m}$  long giving a W/L ratio of 10. A  $\sim 100$  nm ZTSO barrier layer is deposited as previously described and patterned via a shadow mask. Final annealing to a temperature of 300  $^\circ\text{C}$  in air concludes the device fabrication. Additionally, some TFTs are passivated using  $\sim 100$  nm PECVD  $\text{SiO}_2$ . TFTs are characterized in the dark using a Hewlett-Packard 4156C semiconductor parameter analyzer.

## Results and discussion:

### TEM characterization:

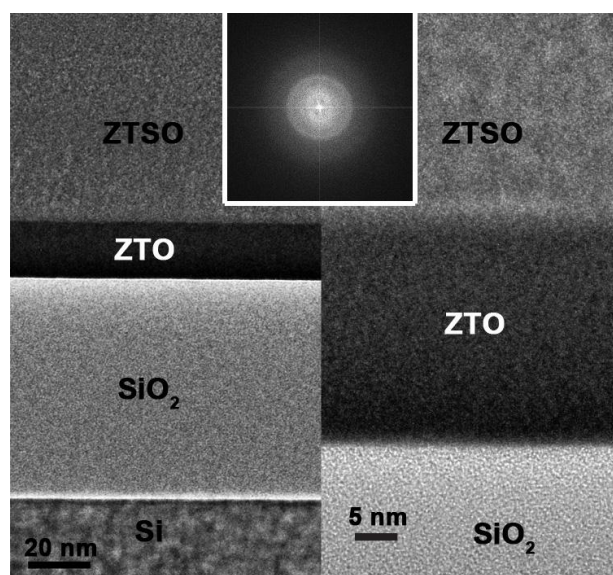


Figure 4.3: (Left) Low-resolution TEM image demonstrating an entire device stack. (Right) High-resolution interfacial TEM image of active interfaces of ZTO channel layer with both  $\text{SiO}_2$  base layer and ZTSO passivation layer. (Inset) Electron diffraction of the device stack taken from the region illustrated in this figure.

Transmission electron micrographs reveal the amorphous nature of the films. The cross-section in Figure 4.3 illustrates the small amount of interfacial damage created through sputter deposition for both the ZTO surface and the silicon dioxide regions of the micrograph as shown by the definition of the interfaces. The interfacial damage corresponds to increased trapping and hysteresis is measured in the electrical characterization. The image details the sharpness ( $<3$  nm) to which the interface aligns after annealing. The propensity to form an evenly-graded interface with minimal evidence of damage to the active layer of the channel (i.e., ZTO) is unique from previous attempts at passivation. The inset shown in Figure 4.3 is an electron diffraction

pattern confirming the amorphous nature of the oxide films at the temperatures utilized in this study.

#### X-ray photoelectron spectroscopy depth profiling:

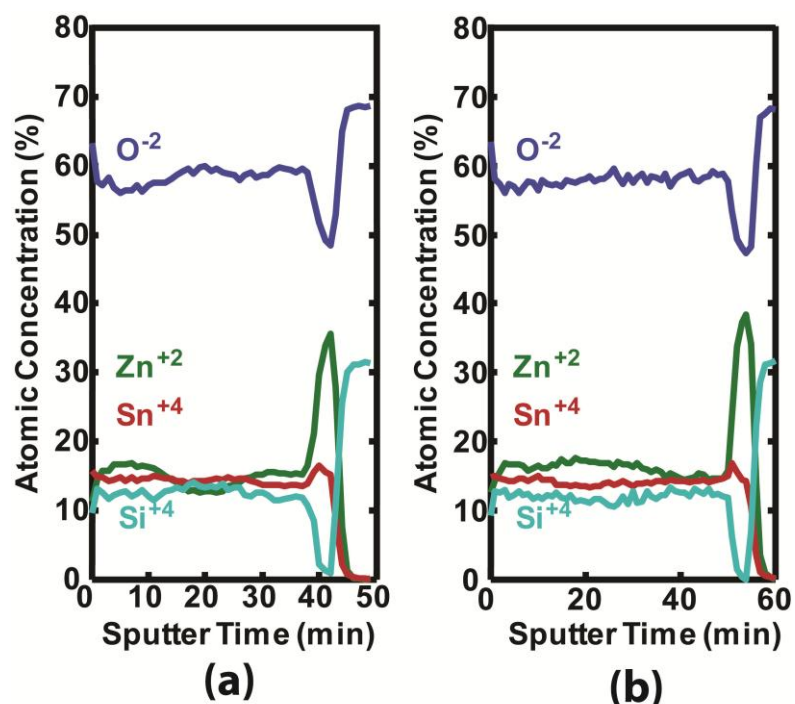


Figure 4.4: X-ray photoelectron spectroscopic depth profiles of atomic composition for: (a) an as-deposited ZTSO film in the device stack shown in Figure 4.3. (b) a 400 °C annealed ZTSO device stack as shown in Figure 4.3.

XPS measurements illustrate the differences in film composition prior-to and after annealing. In Figure 4.4(a) there is a sharp decrease in zinc concentration nearly 30 nm above the interface which then re-equilibrates to the near-interface level after nearly 30 nm. This indicates that there is preferential growth during the sputtering process. Figure 4.4(a) shows that 38 minutes of  $\text{Ar}^+$  sputtering are necessary to burrow through the as-deposited film, while Figure 4.4(b) shows that the same burrowing distance requires an extra ten minutes of sputtering on the 400 °C annealed sample. This

additional sputtering time is indicative of fortification of the ZTSO film by the annealing process. Figure 4.4(b) also clearly illustrates that the compositional variance present in the as-deposited ZTSO layer is annealed away in the final device.

#### X-ray diffraction:

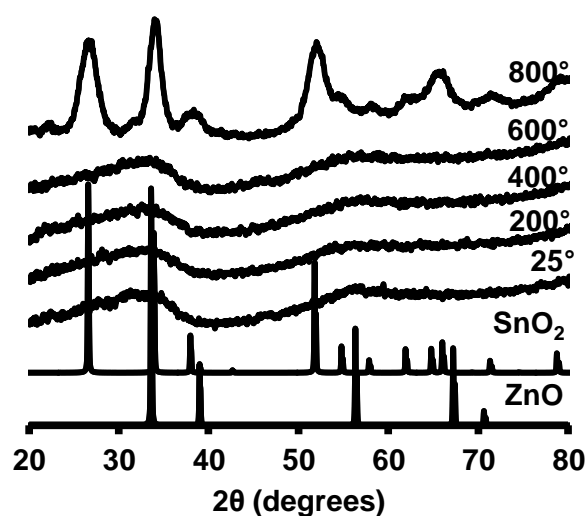


Figure 4.5: X-ray diffraction patterns of a 200 nm film of ZTSO heated to various listed temperatures (in Celsius) with calculated SnO<sub>2</sub> (Cassiterite) and ZnO (Zincite) patterns included for reference.

X-ray characterization clearly shows that the film remains amorphous for all processing temperatures used in this paper (i.e., < 600 °C). Crystallization begins near 600°C with peaks for zincite (ZnO) and cassiterite (SnO<sub>2</sub>) being prevalent in the films crystallized at 800 °C.

### Ultraviolet and visible spectroscopic characterization:

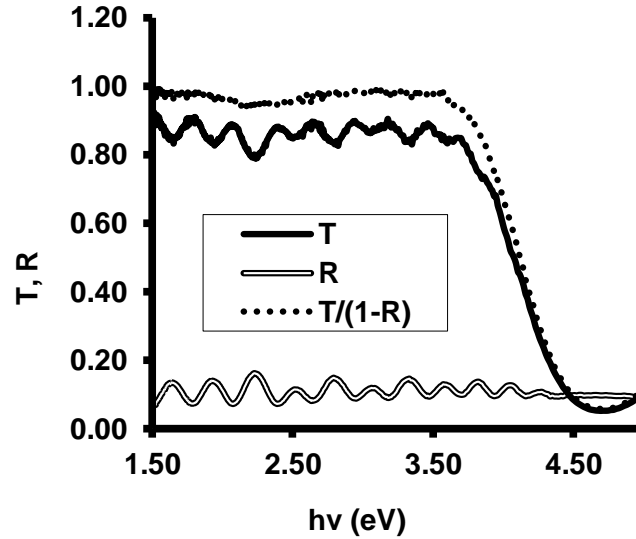


Figure 4.6: Ultraviolet and optical transmission and reflection data for 1.2  $\mu\text{m}$  thick film of ZTSO upon 1 mm thick fused silica.

UV-visible measurements of photonic transmission yield an average ZTSO optical clarity (between 1.7 and 3.1 eV) of 96.5%. Initial ZTSO films of 200 nm thickness results in questionable values of optical clarity very near to that of the silica substrate alone, however the presence of the absorption edge allows for recognition of a film present. Thicker ZTSO films of 0.5 to 1.2  $\mu\text{m}$  are generated to obtain reliable compliance between transmission and reflection fringes. Reflection data of the thicker ZTSO films does not significantly vary from that of the substrate, making the absorbance data appear much less smooth below the absorption edge. Absorption coefficients across the indicated spectrum are calculated using the equation,

$$(7) \quad \alpha = \frac{T}{(1-R)} \left( \frac{1}{t} \right)$$

where  $T$  represents the normalized transmission measurement,  $R$  is the normalized reflection measurement and  $t$  represents the film thickness in centimeters. An indirect band gap is derived from plotting  $(\alpha E)^{1/2}$  vs. photon energy (where  $E$  is the energy of the photon in eV) and finding the point on the x-axis where the linear regression of the slope of the absorption edge crosses. The curve in Figure 4.7 yields a band gap for ZTSO of 3.65 eV and an index of refraction of 1.7, making its optical properties similar to many production amorphous silicon oxide glasses. The optical properties of ZTSO prove its high capability of being used in transparent transistors for TFT back planes.

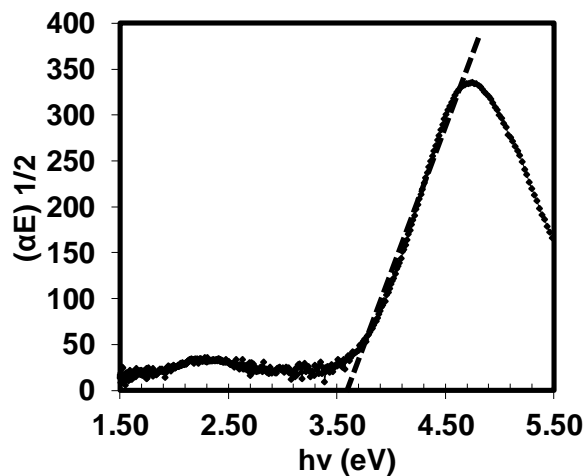


Figure 4.7: Indirect band gap analysis of 1.20 micron film of ZTSO deposited upon fused silica.

### Ellipsometric characterization:

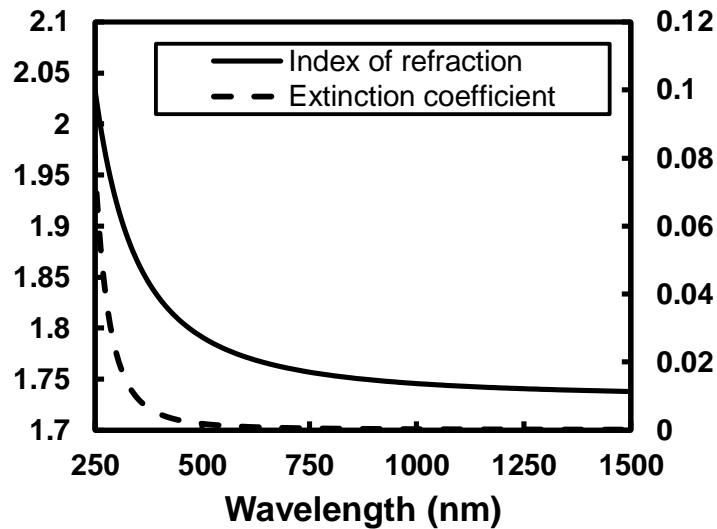


Figure 4.8: Index of refraction ( $n$ ) and extinction coefficient ( $k$ ) for 100-nm ZTSO thin-film annealed to 400 °C.

Figure 4.8 is a plot of the index of refraction for a ZTSO thin film as a function of wavelength. The values were obtained by fitting the experimental data to a Cauchy model, where the index of refraction can be represented as<sup>19</sup>

$$(8) \quad n(\lambda) = A + \frac{B}{\lambda^2} + \frac{C}{\lambda^4},$$

$$(9) \quad k(\lambda) = \alpha e^{\left[\beta \left(\frac{1.24 \times 10^4}{\lambda}\right)\right]}$$

Here A, B, C are material dependent constants,  $\alpha$  is the extinction coefficient amplitude and  $\beta$  is the exponent factor. These parameters as well as the thickness of the

film were defined as fitting parameters. The measured  $\Psi$  and  $\Delta$  spectra are compared against a model consisting of a Cauchy layer above 100 nm of  $\text{SiO}_2$  over a Si substrate. Including surface roughness causes a negligible change in the mean square error (MSE) and is not included in the final model since the films are amorphous at 400 °C. The thickness of the ZTSO layer are measured to be 107 nm with an index of refraction  $n = 1.73$  at 1000 nm. The absorption coefficient is calculated from the extinction coefficient ( $k$ ) data as

$$(10) \quad \alpha = \frac{4\pi k}{\lambda},$$

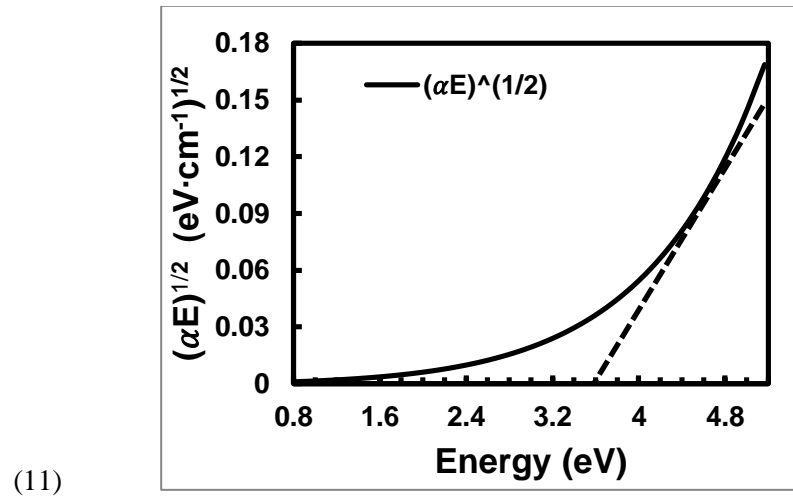


Figure 4.9: Plot of  $(\alpha E)^{1/2}$  vs. photon energy showing regression from which the band gap is estimated using ellipsometry.

Plotting the relationship between  $(\alpha E)^{1/2}$  vs. the energy as shown in Figure 4.9 allows us to estimate the band gap of ZTSO to be 3.6 eV. Since the complex index of refraction ( $N$ ) is related to the dielectric constant ( $\epsilon$ ) as

$$(12) \quad N = n - ik = \sqrt{\epsilon},$$

the relative dielectric constant of ZTSO is estimated to be  $\epsilon = 3.05$  at 1000 nm. While analysis of transparent conducting oxides via ellipsometry is commonly performed using a Lorentz oscillator model, the Cauchy model provides a better fit with a lower MSE for this system when compared to the Lorentz model. The values for the index of refraction and the band gap from this analysis agree well with values obtained via UV-visible spectroscopic characterization shown in the previous section. In addition to ZTSO, IGZO and ZTO films were analyzed using a Tauc-Lorentz model. The dielectric constant for IGZO and ZTO was 3.7 and 3.8, while the band gap was estimated to 3.2 and 3.4 eV respectively.

#### Electrical characterization:

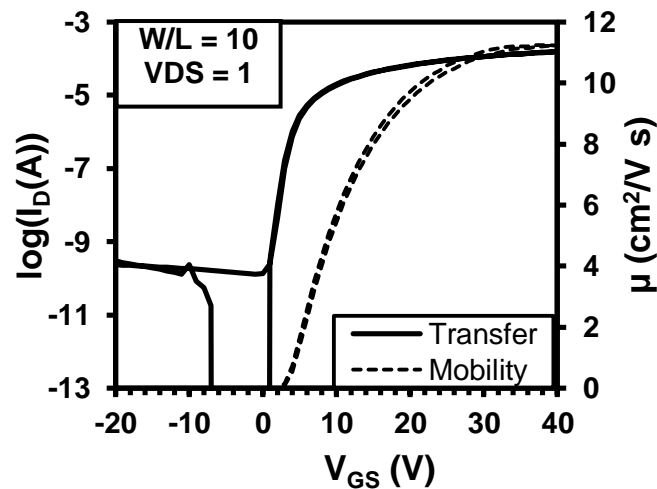


Figure 4.10: Logarithm of the drain current versus the gate-source voltage, i.e.,  $\log(I_D) - V_{GS}$  transfer curve and average mobility curve of a ZTO TFT (i.e. the ZTO surface is exposed to air).

Unpassivated ZTO TFTs are fabricated in order to establish a performance baseline for the material set and processing methods utilized in this paper. A turn-on voltage,  $V_{ON}$ ,

of approximately zero volts is standard for unpassivated devices exposed to air in ambient conditions.

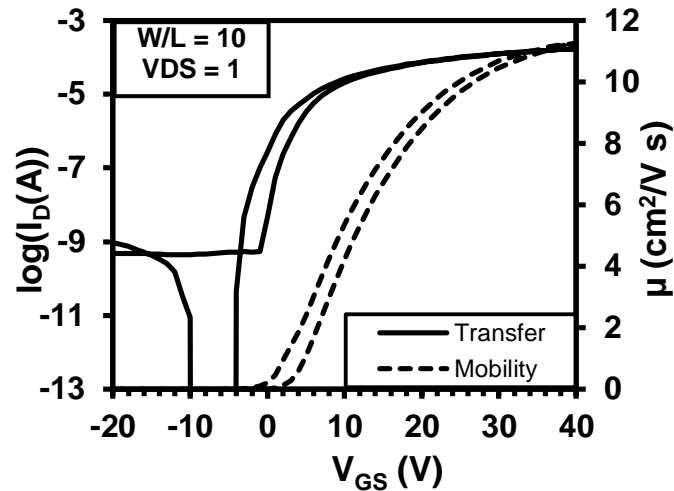


Figure 4.11: Logarithm of the drain current versus the gate-source voltage, i.e.,  $\log(I_D) - V_{GS}$  transfer curve and average mobility measurements of post-passivated TFTs.

Immediately after ZTSO deposition the TFTs have little change in average mobility, however the on-to-off ratio drops from  $10^6$  to  $10^5$  at  $V_{DS} = 1$  V, corresponding to an increase in the off current. The sputter damage shown previously in the TEM interface images of Fig. 1 appears to correspond to oxygen equilibration across the interface.  $V_{ON}$  shifts to the left to -2 volts indicating that the ZTO channel is significantly oxygen deficient, creating a higher number of free carriers.

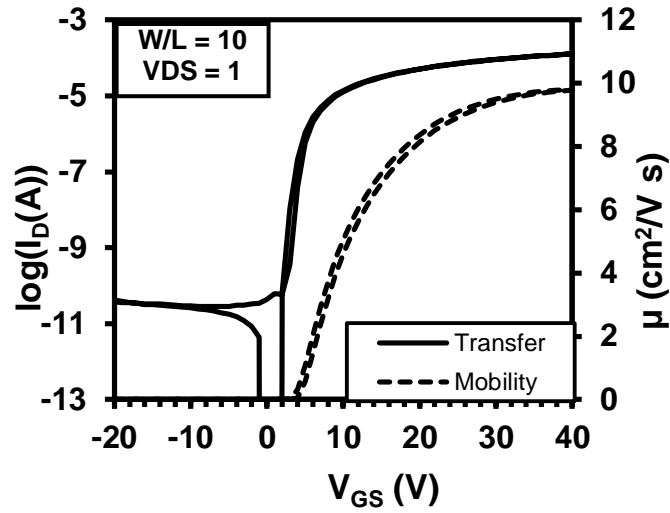


Figure 4.12: Logarithm of the drain current versus the gate-source voltage, i.e.,  $\log(I_D) - V_{GS}$  transfer curve and average mobility measurements ZTSO capped, post 400 °C annealed TFTs.

Annealing to 400 °C after ZTSO deposition allows for re-equilibration of oxygen across the ZTSO/ZTO interface which shifts  $V_{ON}$  to the right to  $\sim +2$  V. This measurement indicates that the channel is decreasing the number of free carriers via removal of oxygen vacancies in the ZTO channel. The on-to-off ratio also re-equilibrates closer to  $10^6$  as in the virgin device. Device average mobilities are decreased slightly to just less than  $10 \text{ cm}^2/\text{Vs}$  which corresponds to the decrease in measurement overvoltage (i.e.,  $V_{GS} - V_{ON}$ ) due to the increase in  $V_{ON}$ .

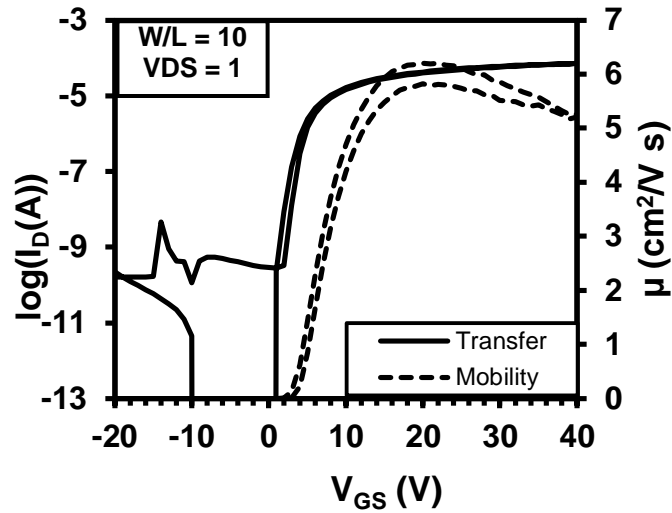


Figure 4.13: Logarithm of the drain current versus the gate-source voltage, i.e.,  $\log(I_D) - V_{GS}$  transfer curve and average mobility measurements of post-passivated, post 400 °C annealed, PECVD SiO<sub>2</sub> coated TFTs.

Finally, a passivation layer (i.e., PECVD SiO<sub>2</sub>) is added to the device stack, and the electrical properties of the TFTs are monitored. The most significant changes in device performance are observed with the PECVD SiO<sub>2</sub> addition, with striking decreases in both the on-to-off ratio and average mobility. The on-to-off ratio is decreased to  $\sim 10^5$  while the average mobility drops to roughly half of that of non-PECVD SiO<sub>2</sub> coated samples. Further studies are necessary to determine the exact cause of this effect.

While the decrease in average mobility and on-to-off ratio are not ideal, this dual layer passivation approach allows for better retention of mobility and  $V_{ON}$  stability than other previously reported systems. It is also important to note that other final passivation steps may yield better retention of mobility, on-to-off ratio, and  $V_{ON}$  stability.

**Conclusions:**

ZTSO is a viable route to achieve channel passivation for transparent transistors. ZTSO utilizes simple chemical properties inherent to SiO<sub>2</sub>, (i.e. oxygen retention, transparency, and glass forming capability) to create a method of moderating changes to the channel layer through less drastic chemical gradation of the interface via the implantation common to high-energy deposition methods. This method shows a promising future of single-tool, low-cost passivation options for sputter-coated transparent electronic devices.

**References:**

- (1) Chiang, H. Q. Wager, J. F. Hoffman, R. L. Jeong, J.; Keszler, D. A. *Applied Physics Letters* **2005**, *86*, 012503.
- (2) Jackson, W. B. Hoffman, R. L.; Herman, G. S. *Appl. Phys. Lett.* **2005**, *87*, 193503.
- (3) Heineck, D. P. McFarlane, B. R.; Wager, J. F. *IEEE Electron Device Lett.* **2009**, *30*, 514-516.
- (4) Hong, D. Chiang, H. Q. Presley, R. E. Dehuff, N. L. Bender, J. P. Park, C. H. Wager, J. F.; Keszler, D. A. *Thin Solid Films* **2006**, *515*, 2717–2721.
- (5) Chiang, H. Q. Development of oxide semiconductors: Materials, devices, and integration, Oregon State University, 2007.
- (6) Chen, Y.-C. Chang, T.-C. Li, H.-W. Chen, S.-C. Lu, J. Chung, W.-F. Tai, Y.-H.; Tseng, T.-Y. *Appl. Phys. Lett.* **2010**, *96*, 262104.
- (7) Jain, V. K. Kumar, P. Kumar, M. Jain, P. Bhandari, D.; Vijay, Y. K. *J. Alloy Compd.* **2010**.
- (8) Dutta, S.; Dodabalapur, A. *Sensor. Actuat. B-Chem.* **2009**, *143*, 50–55.
- (9) Görrn, P. Riedl, T.; Kowalsky, W. *J. Phys. Chem. C* **2009**, *113*, 11126-11130.
- (10) Park, S. H. K. Cho, D. H. Hwang, C. S. Yang, S. Ryu, M. K. Byun, C. W. Yoon, S. M. Cheong, W. S. Cho, K. I.; Jeon, J. H. *ETRI J.* **2009**, *31*, 653–659.
- (11) Hong, D.; Wager, J. F. *J. Vac. Sci. Technol. B* **2005**, *23*, L25.
- (12) Yong-Hoon Kim; Kwang-Ho Kim; Min Suk Oh; Hyun Jae Kim; Jeong In Han; Min-Koo Han; Sung Kyu Park *IEEE Electron Device Lett.* **2010**, *31*, 836-838.
- (13) Cowell, E. W. Alimardani, N. Knutson, C. C. Conley, J. F. Keszler, D. A. Gibbons, B. J.; Wager, J. F. *Adv. Mater.* **2011**, *23*, 74-78.
- (14) Wager, J. F. *Thin Solid Films* **2008**, *516*, 1755-1764.
- (15) Spies, J. A. Schafer, R. Wager, J. F. Hersh, P. Platt, H. A. S. Keszler, D. A. Schneider, G. Kykyneshi, R. Tate, J. Liu, X.; others *Sol. Energ. Mat. Sol. C.* **2009**, *93*, 1296–1308.

- (16) Wager, J. F.; Robertson, J. *J. Appl. Phys.* **2011**, *109*, 094501.
- (17) Wager, J. F. *Mater. Sol. Cells* **submitted**.
- (18) Peacock, P. W.; Robertson, J. *J. Appl. Phys.* **2002**, *92*, 4712.
- (19) Jenkins, F.; White, H. *Fundamentals of Optics*; 4th ed. McGraw-Hill, 1976.
- (20) Robertson, J.; Clark, S. *Phys. Rev. B* **2011**, *83*, 075205.
- (21) Robertson, J.; Falabretti, B. *J. Appl. Phys.* **2006**, *100*, 014111.
- (22) Bersch, E. Rangan, S. Bartynski, R. A. Garfunkel, E.; Vescovo, E. *Phys. Rev. B* **2008**, *78*, 085114.
- (23) Liu, D. Clark, S. J.; Robertson, J. *Appl. Phys. Lett.* **2010**, *96*, 032905.
- (24) Robertson, J. *J. Vac. Sci. Technol. B* **2000**, *18*, 1785.

Table 4.1. Energy band gap ( $E_G$ ), electron affinity ( $\chi$ ), charge neutrality level ( $\Phi_{\text{CNL}}$ ), and Gibbs free energy of formation (kcal/gm-atom) for selected oxides.  $\chi$  and  $\Phi_{\text{CNL}}$  are referenced to the vacuum level.

Oxides	$E_G$ (eV)	$\chi$ (V)	$\Phi_{\text{CNL}}$ (V)	$\Delta G_f$ (kcal/gm-atom)	Reference
ZnO	3.4	4.0	4.1	-38.3	<sup>20</sup>
SnO <sub>2</sub>	3.6	5.0	4.5	-41.4	<sup>20</sup>
In <sub>2</sub> O <sub>3</sub>	2.9	4.1	3.8	-39.7	<sup>20</sup>
Ga <sub>2</sub> O <sub>3</sub>	4.8	3.5	5.5	-47.7	<sup>21</sup>
ZTO (2:1)	3.5	4.3	4.2	NA	averaging
IGZO (1:1:1)	3.6	3.9	4.4	NA	averaging
ZTSO (1:1:1)	5.3	3.3	4.7	NA	averaging
SiO <sub>2</sub>	9	0.9	5.4	-68.2	<sup>21</sup>
Al <sub>2</sub> O <sub>3</sub>	6.2-7.0	1.65-2.5	3.6-4.7	-75.6	<sup>22,23</sup>
HfO <sub>2</sub>	6.0	2.4	4.7	-84.5	<sup>21</sup>
Y <sub>2</sub> O <sub>3</sub>	6	~2	5.6	-86.8	<sup>24</sup>

Table 4.2. High-frequency relative dielectric constant ( $\epsilon_{\infty R}$ ), interface parameter for a surface (S), and surface state density ( $D_{SS}$ ) for selected semiconductors and insulators.

Oxides	$\epsilon_{\infty R}$ (unitless)	S (unitless)	$D_{SS}$ ( $\times 10^{13} \text{ cm}^{-2} \text{ eV}^{-1}$ )	Reference
ZTO (2:1)	3.8	0.56	4.1	This work
IGZO (1:1:1)	3.7	0.58	3.7	This work
ZTSO (1:1:1)	3.1	0.69	1.9	This work
$\text{SiO}_2$	2.25	0.86	0.5	<sup>21</sup>
$\text{Al}_2\text{O}_3$	3.12	0.69	1.9	<sup>21</sup>
$\text{HfO}_2$	4	0.53	5.0	<sup>21</sup>
$\text{Y}_2\text{O}_3$	4.4	0.46	7.0	<sup>24</sup>
Si	12	0.08	200	<sup>21</sup>
Ge	16	0.04	500	<sup>21</sup>

Table 4.3. Interface parameter ( $S_{PS}$ ), interface dipole voltage ( $\Delta_{PS}$ ), and interface state density ( $D_{PS}$ ) for selected semiconductor/passivation layer combinations. For the assessment of  $\Delta_{PS}(\text{Si}/\text{SiO}_2)$ ,  $\Phi_{\text{CNL}}(\text{Si}) = 4.7 \text{ V}$  [3].

Semiconductor	Passivation layer	$S_{PS}$ (unitless)	$\Delta_{PS}$ (V)	$D_{PS}$ ( $\times 10^{13} \text{ cm}^{-2} \text{ eV}^{-1}$ )
ZTO (2:1)	ZTSO (1:1:1)	0.65	0.18	1.3
ZTO (2:1)	$\text{SiO}_2$	0.82	0.22	0.43
ZTO (2:1)	$\text{Y}_2\text{O}_3$	0.67	0.52	2.6
IGZO (1:1:1)	ZTSO (1:1:1)	0.65	0.10	1.3
IGZO (1:1:1)	$\text{SiO}_2$	0.82	0.18	0.43
IGZO (1:1:1)	$\text{Y}_2\text{O}_3$	0.56	0.53	2.4
Si	$\text{SiO}_2$	0.84	0.10	0.48

## CONCLUSIONS

Interface chemical reactions are of critical importance to the next generation of devices.

I have shown that novel chemistries may be achieved by utilizing amorphous metals and amorphous, solution-processed oxides. I have also shown that the component metals of bulk metallic glasses have selective chemical reactions that drive their interfacial diffusion behavior.

Finally, I have shown that Zinc Tin Silicon Oxide is a viable passivation material for amorphous-oxide semiconductors.

## BIBLIOGRAPHY

- Abadias, G. et al. "Stress, interfacial effects and mechanical properties of nanoscale multilayered coatings." *Surface and Coatings Technology* 202.4-7 (2007): 844–853. Print.
- Alemayehu, Matti et al. "Tunable dielectric thin films by aqueous, inorganic solution-based processing." *Solid State Sciences* (2011): n. pag. Web. 11 Oct. 2011.
- Anderson, J. T. et al. "Solution-Processed  $\text{HfSO}_x$  and  $\text{ZrSO}_x$  Inorganic Thin-Film Dielectrics and Nanolaminates." *Advanced Functional Materials* 17.13 (2007): 2117-2124. Web. 7 July 2011.
- Bersch, Eric et al. "Band offsets of ultrathin high-k oxide films with Si." *Phys. Rev. B* 78.8 (2008): 085114.
- Brill, Robert H. "Corning Museum of Glass | Articles | Does Glass Flow?" Web. 13 Oct. 2011.
- Cai, Wenshan, Dentcho Genov, and Vladimir Shalaev. "Superlens based on metal-dielectric composites." *Physical Review B* 72 (2005): n. pag. Web. 19 Sept. 2011.
- Chang, Y.-J. et al. "High-Performance, Spin-Coated Zinc Tin Oxide Thin-Film Transistors." *Electrochemical and Solid-State Letters* 10 (2007): H135. Web. 13 Oct. 2011.
- Chen, W., Y. Wang, et al. "Bulk metallic glasses in the Zr-Al-Ni-Cu system." *Acta materialia* 51.7 (2003): 1899–1907. Print.
- Chen, Yu-Chun, Ting-Chang Chang, et al. "Bias-induced oxygen adsorption in zinc tin oxide thin film transistors under dynamic stress." *Applied Physics Letters* 96.26 (2010): 262104. Web. 23 May 2011.
- Chiang, H. Q. "Development of oxide semiconductors: Materials, devices, and integration." 2007 : n. pag. Print.
- Chiang, H. Q et al. "High mobility transparent thin-film transistors with amorphous zinc tin oxide channel layer." *Applied Physics Letters* 86.1 (2005): 012503. Print.
- Chirakkara, S., K. K. Nanda, and S. B. Krupanidhi. "Pulsed laser deposited ZnO: In as transparent conducting oxide." *Thin Solid Films* (2011): n. pag. Print.

- Cowell III, E. William et al. "Amorphous Metal/Oxide Nanolaminate." *ACS Applied Materials & Interfaces* 2 (2010): 1811-1813. Web. 20 Sept. 2011.
- Cowell, E. W. "Amorphous multi-component metals as electrode materials." 2010 : n. pag. Print.
- Cowell, E. William et al. "Advancing MIM Electronics: Amorphous Metal Electrodes." *Advanced Materials* 23.1 (2011): 74-78. Web. 23 May 2011.
- Deville, H. St. C. "Recherches sur les métaux, et en particulier sur l'aluminium et sur une nouvelle forme du silicium." *ANNALES DE CHIMIE ET DE PHYSIQUE* 43 (1854): 31-33. Print.
- Dixon, J.E., J.R. Cann, and Colin Renfrew. "Obsidian and the origins of trade." *Scientific American* 218.3 38-46. Print.
- Doan, N., K. Kontturi, and C. Johans. "Directing oxidation of cobalt nanoparticles with the capping ligand." *Journal of colloid and interface science* 350.1 (2010): 126–131. Print.
- Dolan, M. et al. "Ni-based amorphous alloy membranes for hydrogen separation at 400° C." *Journal of Membrane Science* 326.2 (2009): 549–555. Print.
- Dutta, S., and A. Dodabalapur. "Zinc tin oxide thin film transistor sensor." *Sensors and Actuators B: Chemical* 143.1 (2009): 50–55. Print.
- Eastman, ED et al. "Preparation and Properties of the Oxide-Sulfides of Cerium, Zirconium, Thorium and Uranium<sup>2</sup>." *Journal of the American Chemical Society* 73.8 (1951): 3896–3898. Print.
- Erslev, P. T et al. "Mapping out the distribution of electronic states in the mobility gap of amorphous zinc tin oxide." *Applied Physics Letters* 95 (2009): 192115. Print.
- Görrn, P. et al. "Zinc tin oxide based driver for highly transparent active matrix OLED displays." *Solid-State Electronics* 53.3 (2009): 329–331. Print.
- Gallagher, J.P. "Contemporary stone tools in Ethiopia: Implications for archaeology." *Journal of Field Archaeology* 4.4 (1977): 407–414. Print.
- Gorham, Justin et al. "Surface Reactions of Molecular and Atomic Oxygen with Carbon Phosphide Films." *The Journal of Physical Chemistry B* 109.43 (2005): 20379-20386. Web. 26 May 2011.

- Görrn, Patrick, Thomas Riedl, and Wolfgang Kowalsky. "Encapsulation of Zinc Tin Oxide Based Thin Film Transistors." *The Journal of Physical Chemistry C* 113.25 (2009): 11126-11130. Web. 23 May 2011.
- Grubbs, Melody et al. "Development and characterization of high temperature stable Ta-W-Si-C amorphous metal gates." *Applied Physics Letters* 97.22 (2010): 223505. Print.
- Hara, S. et al. "An amorphous alloy membrane without noble metals for gaseous hydrogen separation." *Journal of Membrane Science* 164.1-2 (2000): 289–294. Print.
- Heineck, D.P., B.R. McFarlane, and J.F. Wager. "Zinc Tin Oxide Thin-Film-Transistor Enhancement/Depletion Inverter." *IEEE Electron Device Letters* 30.5 (2009): 514-516. Web. 23 May 2011.
- Hong, D. et al. "Transparent thin-film transistor exploratory development via sequential layer deposition and thermal annealing." *Thin Solid Films* 515.4 (2006): 2717–2721. Print.
- Hong, David, and John F. Wager. "Passivation of zinc–tin–oxide thin-film transistors." *Journal of Vacuum Science & Technology B: Microelectronics and Nanometer Structures* 23.6 (2005): L25. Web. 23 May 2011.
- Hsu, S. M, L. Raine, and H. Fanger. "Use of avidin-biotin-peroxidase complex (ABC) in immunoperoxidase techniques: a comparison between ABC and unlabeled antibody (PAP) procedures." *Journal of Histochemistry & Cytochemistry* 29.4 (1981): 577. Print.
- Hultman, Lars et al. "Interface structure in superhard TiN-SiN nanolaminates and nanocomposites: Film growth experiments and ab initio calculations." *Physical Review B* 75 (2007): n. pag. Web. 19 Sept. 2011.
- Inoue, Akihisa, and Nobuyuki Nishiyama. "New Bulk Metallic Glasses for Applications as Magnetic-Sensing, Chemical, and Structural Materials." *MRS Bulletin* 32.8 (2007): 651-658. Print.
- Jackson, W. B., R. L. Hoffman, and G. S. Herman. "High-performance flexible zinc tin oxide field-effect transistors." *Applied Physics Letters* 87.19 (2005): 193503. Web. 23 May 2011.
- Jain, V. K et al. "Study of post annealing influence on structural, chemical and electrical properties of ZTO thin films." *Journal of Alloys and Compounds* (2010): n. pag. Print.

Jenkins, Francis, and Harvey White. *Fundamentals of Optics*. 4th ed. McGraw-Hill, 1976. Print.

Jiang, K., J. T Anderson, et al. "Low-Energy Path to Dense HfO<sub>2</sub> Thin Films with Aqueous Precursor." *Chemistry of Materials* 23.4 (2011): 945-952. Print.

Jiang, K., A. Zakutayev, et al. "Low-temperature, solution processing of TiO<sub>2</sub> thin films and fabrication of multilayer dielectric optical elements." *Solid State Sciences* 11.9 (2009): 1692–1699. Print.

Kasper, N. et al. "In situ oxidation study of MgO (1 0 0) supported Pd nanoparticles." *Surface Science* 600.14 (2006): 2860-2867. Print.

Kim, H. "Atomic layer deposition of metal and nitride thin films: Current research efforts and applications for semiconductor device processing." *Journal of Vacuum Science & Technology B: Microelectronics and Nanometer Structures* 21 (2003): 2231. Web. 19 Sept. 2011.

Kim, Hye-Ri et al. "Effects of Hydrogen Doping on the Electrical Properties of Zinc-Tin-Oxide Thin Films." *JAPANESE JOURNAL OF APPLIED PHYSICS* 49.12 (2010): n. pag. Print.

Klement, W., R. H. Willens, and POL Duwez. "Non-crystalline Structure in Solidified Gold-Silicon Alloys." *Nature* 187 (1960): 869-870. Print.

Leskelä, M., and M. Ritala. "Atomic layer deposition (ALD): from precursors to thin film structures." *Thin Solid Films* 409.1 (2002): 138–146. Print.

Liu, D., S. J. Clark, and J. Robertson. "Oxygen vacancy levels and electron transport in Al<sub>2</sub>O<sub>3</sub>." *Applied Physics Letters* 96.3 (2010): 032905. Web. 22 July 2011.

Mensingher, Zachary L. et al. "Synthesis of Heterometallic Group 13 Nanoclusters and Inks for Oxide Thin-Film Transistors." *Angewandte Chemie* 120.49 (2008): 9626-9628. Web. 18 Aug. 2011.

Meyers, Stephen T. et al. "Solution-Processed Aluminum Oxide Phosphate Thin-Film Dielectrics." *Chemistry of Materials* 19.16 (2007): 4023-4029. Web. 7 July 2011.

Mikhelashvili, V., G. Eisenstein, and A. Lahav. "High capacitance density metal-insulator-metal structure based on Al<sub>2</sub>O<sub>3</sub>-HfTiO nanolaminate stacks." *Applied Physics Letters* 90 (2007): 013506. Web. 19 Sept. 2011.

Mikhelashvili, V., E. Garshtein, and G. Eisenstein. "Characteristics of Al/sub 2/O/sub 3//TiO/sub 2/ nanolaminates and AlTiO thin films on Si." *IEEE Electron Device Letters* 27 (2006): 344-346. Web. 19 Sept. 2011.

Mulas, G., L. Schiffini, S. Scudino, and G. Cocco. "Mechanochemical hydrogenation of ZrCuAlNi based powders:: Part I. Structural reconstruction and chemical properties." *Journal of Alloys and Compounds* 454.1-2 (2008): 83–88. Print.

---. "Mechanochemical hydrogenation of ZrCuAlNi based powders:: Part II. Mechanical treatment intensity and kinetic behaviour." *Journal of Alloys and Compounds* 455.1-2 (2008): 106–112. Print.

Nicholson, Paul T., and Ian Shaw. *Ancient Egyptian materials and technology*. Cambridge, UK: Cambridge University Press, 2000. Print.

Ningshen, S. et al. "Corrosion behavior of Zr-based metallic glass coating on type 304L stainless steel by pulsed laser deposition method." *Surface and Coatings Technology* 205.15 (2011): 3961-3966. Print.

Nomura, K. "Thin-Film Transistor Fabricated in Single-Crystalline Transparent Oxide Semiconductor." *Science* 300.5623 (2003): 1269-1272. Web. 7 June 2011.

Nomura, K., H. Ohta, A. Takagi, T. Kamiya, M. Hirano, and H. Hosono. "Room-temperature fabrication of transparent flexible thin-film transistors using amorphous oxide semiconductors." *Nature* 432.7016 (2004): 488–492. Print.

---. "Room-temperature fabrication of transparent flexible thin-film transistors using amorphous oxide semiconductors." *Nature* 432.7016 (2004): 488–492. Print.

Padhy, N., S. Ningshen, and U. Kamachi Mudali. "Electrochemical and surface investigation of zirconium based metallic glass Zr<sub>59</sub>Ti<sub>3</sub>Cu<sub>20</sub>Al<sub>10</sub>Ni<sub>8</sub> alloy in nitric acid and sodium chloride media." *Journal of Alloys and Compounds* 503.1 (2010): 50–56. Print.

Paillier, Jerome et al. "Characterization of corrosion phenomena of Zr-Ti-Cu-Al-Ni metallic glass by SEM and TEM." *Materials Characterization* 61.10 (2010): 1000-1008. Print.

Park, S. H.K et al. "Channel Protection Layer Effect on the Performance of Oxide TFTs." *ETRI journal* 31.6 (2009): 653–659. Print

Peacock, P. W., and J. Robertson. "Band offsets and Schottky barrier heights of high dielectric constant oxides." *Journal of Applied Physics* 92.8 (2002): 4712. Web. 21 July 2011.

Pekarskaya, E., J. F. Löffler, and W. L. Johnson. "Microstructural studies of crystallization of a Zr-based bulk metallic glass." *Acta materialia* 51.14 (2003): 4045–4057. Print.

Pilkington, L. A. B. "Review Lecture. The Float Glass Process." *Proceedings of The Royal Society of London A* 314 (1969): 1-25. Print.

Qiu, F. et al. "Formation of a Multiphase Gradient Structure in a Zr–Cu–Ni–Al–O Alloy." *Advanced Engineering Materials* 10.4 (2008): 384-388. Web. 10 July 2011.

Riedl, Thomas, Patrick Gorrn, and Wolfgang Kowalsky. "Transparent Electronics for See-Through AMOLED Displays." *Journal of Display Technology* 5.12 (2009): 501-508. Web. 23 May 2011.

Riordan, Michael. "The Silicon Dioxide Solution - IEEE Spectrum." 2007. Web. 13 Oct. 2011.

Robertson, J., and S. Clark. "Limits to doping in oxides." *Physical Review B* 83.7 (2011): 075205. Web. 22 July 2011.

Robertson, J., and B. Falabretti. "Band offsets of high K gate oxides on III-V semiconductors." *Journal of Applied Physics* 100.1 (2006): 014111. Web. 22 July 2011.

Robertson, John. "Band offsets of wide-band-gap oxides and implications for future electronic devices." *J. Vac. Sci. Technol. B* 18 (2000): 1785. Print.

Sanada, N. et al. "Extremely low sputtering degradation of polytetrafluoroethylene by C60 ion beam applied in XPS analysis." *Surface and Interface Analysis* 36 (2004): 280-282. Web. 9 Oct. 2011.

Sharma, Parmanand, Kunio Yubuta, et al. "Brittle metallic glass deforms plastically at room temperature in glassy multilayers." *Physical Review B* 80 (2009): n. pag. Web. 19 Sept. 2011.

Sharma, Parmanand, Wei Zhang, et al. "Nanoscale Patterning of Zr-Al-Cu-Ni Metallic Glas Thin Films Deposited by Magnetron Sputtering." *Journal of Nanoscience and Nanotechnology* 5.3 (2005): 416-420. Print.

- Song, Keunkyu et al. "Solution processed invisible all-oxide thin film transistors." *Journal of Materials Chemistry* 19.46 (2009): 8881. Web. 23 May 2011.
- Spies, J. A. et al. "pin double-heterojunction thin-film solar cell p-layer assessment." *Solar Energy Materials and Solar Cells* 93.8 (2009): 1296–1308. Print.
- Stoev, K., and K. Sakurai. "Recent theoretical models in grazing incidence x-ray reflectometry." *The Rigaku J* 14.2 (1997): 22–37. Print.
- Stowers, Jason, and Douglas A. Keszler. "High resolution, high sensitivity inorganic resists." *Microelectronic Engineering* 86 (2009): 730-733. Print.
- Sun, S. et al. "Use of C60 cluster projectiles for sputter depth profiling of polycrystalline metals." *Surface and Interface Analysis* 36 (2004): 1367-1372. Web. 9 Oct. 2011.
- Tawarayama, Hiromasa et al. "Oxide Glass/Amorphous Metal Alloy Laminated Membrane for Hydrogen Separation." *Chemistry Letters* 38.5 (2009): 502. Print.
- Thomson, J. J. "On Bodies Smaller Than Atoms." *Popular Science Monthly* 1901 : 323-335. Print.
- Trinh, DH et al. "Nanocomposite Al<sub>2</sub>O<sub>3</sub>-ZrO<sub>2</sub> thin films grown by reactive dual radio-frequency magnetron sputtering." *Thin Solid Films* 516.15 (2008): 4977–4982. Print.
- Wager, J. F, and J. Robertson. "Metal-induced gap states modeling of metal-Ge contacts with and without a silicon nitride ultrathin interfacial layer." *Journal of Applied Physics* 109.9 (2011): 094501. Print.
- Wager, J.F. "Transparent electronics: Schottky barrier and heterojunction considerations." *Thin Solid Films* 516.8 (2008): 1755-1764.
- Wang, C.M., D.R. Baer, et al. "Electron beam-induced thickening of the protective oxide layer around Fe nanoparticles." *Ultramicroscopy* 108.1 (2007): 43-51. Print.
- Wang, Y., J. Li, et al. "Ductile crystalline–amorphous nanolaminates." *Proceedings of the National Academy of Sciences* 104.27 (2007): 11155. Print.
- Ylönen, M. et al. "Potential of amorphous Mo-Si-N films for nanoelectronic applications." *Microelectronic engineering* 70.2-4 (2003): 337–340. Print.

Yong-Hoon Kim et al. "Ink-Jet-Printed Zinc&#x2013;Tin&#x2013;Oxide Thin-Film Transistors and Circuits With Rapid Thermal Annealing Process." *IEEE Electron Device Letters* 31.8 (2010): 836-838. Web. 23 May 2011.

Zhou, Lei et al. "Ion-Mobility Spectrometry of Nickel Nanoparticle Oxidation Kinetics: Application to Energetic Materials." *Journal of Physical Chemistry C* 112.42 (2008): 16209-16218. Web. 26 May 2011.

APPENDICES

## Appendix A.1

### Amorphous Metal/Oxide Nanolaminate

E. William Cowell III, Christopher C. Knutson, John F. Wager, and Douglas A. Keszler

## Introduction

In this letter, we describe a new class of nanolaminates and their unique interfacial characteristics. Nanolaminates in the present context are defined as stacks of alternating ultrathin layers of dissimilar materials. Such laminates have engendered interest for their ultra-low thermal conductivities (1, 2), high-area capacitance densities (3), and enhanced mechanical properties (4). They have been fabricated using a variety of techniques. Atomic-layer deposition (ALD) has been used to deposit insulator/insulator (5-7) and insulator/metal systems (8, 9). Pulsed-laser and aqueous-solution deposition have been used to produce high-quality oxide/oxide nanolaminates (10, 11), and DC magnetron sputtering provides a convenient means for deposition of metal/metal systems (4).

In this contribution, we outline a new approach relying on the combination of simple DC magnetron sputtering and solution processing for synthesis of very high quality, readily reproduced nanolaminates built from an amorphous metal and an amorphous oxide. Combining these materials at the nanometer scale through the selected deposition methods provides unprecedented opportunities for inducing and studying interlayer chemical reactions and designing unique, chemically graded interfaces. The oxide component is an alumina-rich phosphate (AlPO) (12) that is readily deposited from an aqueous solution. Through spin coating, film thickness can be precisely controlled by adjusting concentrations of the solution components. Because the aqueous solution contains no organic species, a high-temperature burn out is not required, allowing production of high-quality films at temperatures much lower than those associated with

a conventional sol-gel process employing metal-organic precursors. The aqueous solution-based deposition techniques also offer an easily managed method for producing high-quality films with simple beaker chemistries and extremely short processing times.

The Zr-Al-Cu-Ni amorphous multicomponent metal film (AMMF) was first investigated by Sharma and coworkers(13). This alloy, as a bulk material, exhibits superior mechanical strength arising from its amorphous nature. It has also been deposited in thin-film form via magnetron sputtering, yielding an atomically smooth surface (13). This smoothness makes the Zr-Al-Cu-Ni AMMF an especially attractive candidate for incorporation in nanolaminates. One of the driving forces controlling the amorphous nature of an AMMF is the disparate atomic radii among the constituent atomic metal components. If the condition of high disparity is met, a high degree of flexibility in the composition of AMMFs can be achieved.

Compositional flexibility creates an ability to tune the work function and to engineer the physical properties of the resulting interface between the AMMF and the solution-derived oxide. Therefore, AMMFs appear to be intriguing materials for use in engineering potential barriers and controlling charge in metal-insulator devices. We demonstrate below that AlPO/Zr-Al-Cu-Ni interfaces exhibit unique chemical characteristics on the basis of the method of film deposition. The nanolaminate structure is especially well-suited for investigation of these characteristics, as the modulation of interfacial properties can be controlled and then analyzed within a single nanolaminate structure by changing film and bilayer thickness.

## Results and discussion

The solution precursor for the amorphous oxide used in the nanolaminate was prepared as previously described (12) to a 0.1M concentration of aluminum. The solution was then spin coated onto the AMMF at a speed of 3000 rpm for a duration of 30 s, followed by treatment at 300 °C for 1 min on a hot plate.

The Zr-Al-Cu-Ni AMMF was deposited by using DC magnetron sputtering at a power of 60 W, a pressure of 3 mTorr, and a 20 sccm flow of Ar (g). The deposition rate at these conditions was measured to be ~10 nm/min. The AMMF composition from EPMA analysis of a 200-nm film was established as Zr<sub>40</sub>Cu<sub>35</sub>Al<sub>15</sub>Ni<sub>10</sub>. A base layer for the nanolaminate comprising 200 nm of AMMF was first deposited onto a 25 × 25 mm<sup>2</sup> substrate of Si coated with 100 nm of thermally grown SiO<sub>2</sub>.

Electron diffraction from the AMMF layer confirms the amorphous nature of the film. An initial nanolaminate was fabricated via deposition of eight alternating 10-nm thick films of AlPO and AMMF. Electron scattering through the entire stack reveals no evidence of crystallization. A TEM micrograph of the full nanolaminate consisting of four bilayers, each targeted at a thickness of 20 nm, is shown in Figure 1a. The surface of the base 200 nm AMMF is rather rough, whereas subsequent 10 nm AMMF layers are smooth. The roughening of the thick base layer has been consistently reproduced in subsequent nanolaminates, cf. Figure 1b. To investigate the cause of the roughening, we fabricated a nanolaminate with a 10 nm AMMF layer as the base. A comparison of X-ray reflectivity data between a nanolaminate with a 200 nm base layer and

a nanolaminate with a 10 nm base layer indicates that the 10 nm layer is much smoother. The fringes in the XRR pattern collected from the 10 nm base nanolaminate extend  $5^\circ 2\theta$  further than the pattern from the 200 nm base nanolaminate, consistent with the roughening of the thicker film. Investigation into the driving force for formation of the 200 nm AMMF roughening is ongoing.

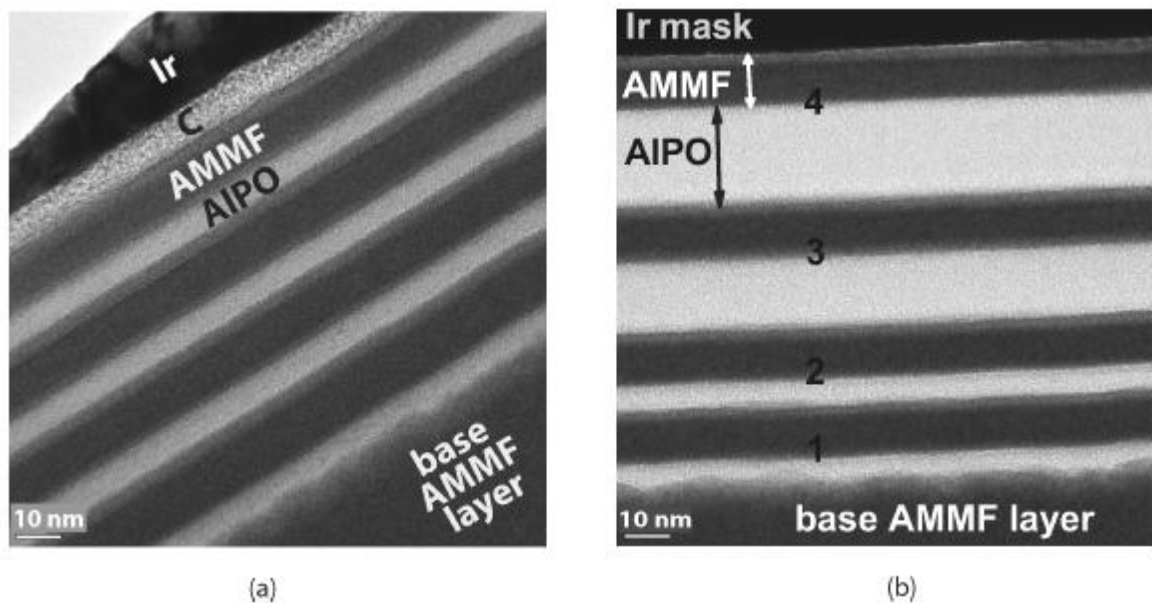


Figure A.3.1. (a) TEM micrograph of an AlPO/AMMF nanolaminate comprised of four 20 nm AlPO/AMMF bilayers. Carbon and iridium layers are deposited onto the top layer of the AMMF to prevent damage during focused ion beam (FIB) sample preparation. (b) TEM micrograph of an AlPO/AMMF nanolaminate comprised of 4 AlPO/AMMF bilayers. The lower two bilayers have a 20 nm thickness target; the AlPO thickness of bilayers 3 and 4 is targeted at 15 and 20 nm, respectively.

A high-angle annular dark field (HAADF) image of the two bilayers nearest the 200 nm AMMF base layer of the nanolaminate shown in Figure 1a is presented in Figure 2. The contrast of the HAADF image is proportional to the atomic numbers of the constituent elements, and it indicates that the interfacial regions between the AlPO and

AMMF layers contain elements lighter than those in the AMMF. The AIPO and AMMF interfaces exhibit contrasts that differ from both the AIPO and the AMMF in the secondary TEM micrograph.

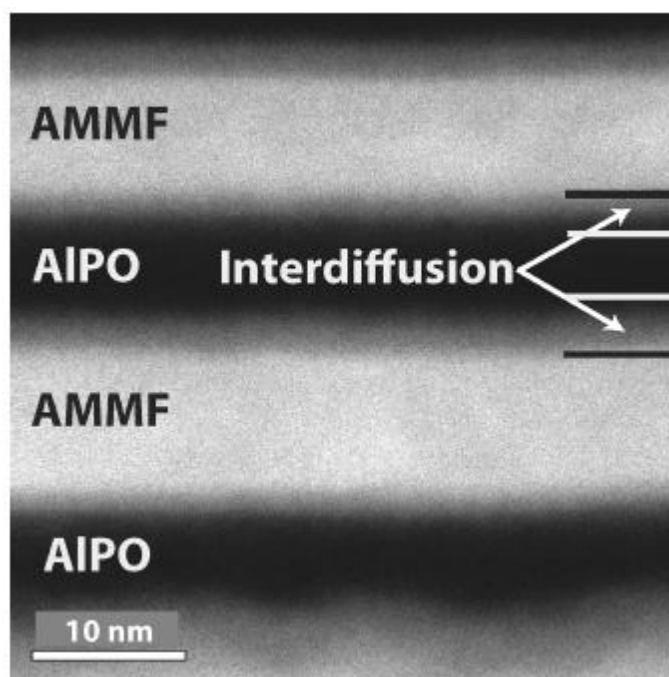


Figure A.1.4. HAADF image of lower 2 bilayers. Distances between horizontal lines are 10 nm based on image scale. Interdiffusion layers are hypothesized as metal atoms from AMMF diffusing into AIPO.

The contrast of the interfacial regions between the AIPO and AMMF is similar in appearance to the top of the nanolaminate, which forms on the last-deposited AMMF layer at room temperature in air without heating. Hence, even without heat, the AMMF film exposed to air appears to form a native oxide coating. This assertion is supported by XPS depth profiling, *vide infra*, where Zr(IV) is observed on top of the final AMMF layer in the nanolaminate. Interestingly, the thickness of this

native overcoat is similar to the thicknesses of the AMMF/AIPO interfaces on the top sides of the AMMFs. These observations are again consistent with the formation of a native oxide on exposing the AMMF to air with the result that the AIPO is likely being solution-deposited onto an oxide-coated AMMF.

EDS analysis was performed on the TEM sample to investigate elemental composition across the AMMF/AIPO interfaces. The EDS analysis showed that Cu and Zr atoms diffuse deeply into the AIPO layer, whereas the Ni atoms are substantially retained in the AMMF. The veracity of these results, however, was initially uncertain because of possible beam spreading of the incident electrons through the TEM sample, causing only an apparent presence of Zr and Cu in the AIPO film. Simulations of the beam spread, performed by the Analytical and Development Labs (ADL) at Hewlett Packard-Corvallis were consistent with an areal resolution of the EDS signal on the order of the dimension of the AIPO film. The simulations supported the view that the Zr and Cu EDS signals in the AIPO film could be an artifact of beam spreading through the sample. Applying the simulations to possible signal blurring, however, was inconsistent with the Ni signal, which appears to go to zero in the AIPO film. This inconsistency in the Ni signal did not support a beam-spreading hypothesis. A depth profile using X-ray photoelectron spectroscopy was undertaken to further investigate the composition of the nanolaminate layers and to examine the possible beamspreading effects of the EDS analysis. The profile data shown in Figure A.1.3 were taken from the nanolaminate shown in Figure A.1.1b, where the AIPO layers were deposited at thicknesses

of 20, 15, and 10 nm. As seen in Figure A.1.3a, the general characteristics of the laminated structure are compositionally verified. Layers of AMMF and AIPO are clearly evident, and the layer thicknesses of AIPO, ranging from 10 to 20 nm, are confirmed.

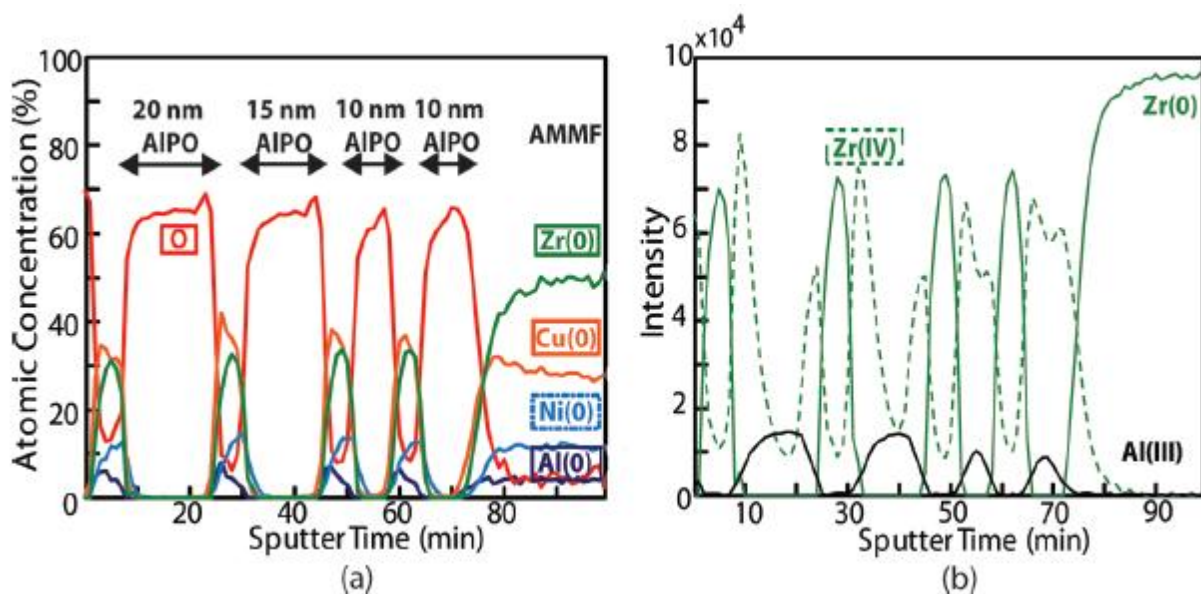


Figure A.1.5. (a) XPS depth profile of Zr, O, Cu, Al, and Ni taken through the nanolaminate shown in Figure A.1.1b. (b) XPS depth profile of Zr(IV) and Al(III) taken through the nanolaminate shown in Figure A.1.1b.

More detailed profiles for Zr(O), Zr(IV), and Al(III) are summarized in Figure 3b. Here, the presence of Zr(O) in the AMMF is confirmed. In the AIPO layers, however, the oxidation state is Zr(IV). For the 10 nm AIPO films, the Zr(IV) signal reveals that Zr has permeated the entire thickness. For the thicker 15 and 20 nm AIPO films, there is a bifurcation in the Zr signals, indicating that the AIPO layers are sufficiently thick to inhibit Zr migration. The Cu, Zr, and Ni metal profiles, presented in Figure 3a, show that the metal signals do not exist through the AIPO, and that the atomic concentrations

of the Cu and Ni metals match those of the bulk. No signals were detected for Cu(II) or Ni(II), indicating that the oxidation-reduction reaction between the AMMF and AlPO is selective to Zr.

The lack of XPS metal signals in the AlPO suggests that the Cu EDS signal in the AlPO is an artifact of beam spreading or signal averaging and that the Zr signal was in fact Zr(IV). As seen in Figure 3b, the Zr(IV) XPS profiles differ for the top and bottom interfaces in the nanolaminate structure. The higher intensity Zr(IV) peak repeatedly occurs at the interface involving sputter deposition of the AMMF onto the AlPO, whereas the lower intensity Zr(IV) peak occurs for deposition of AlPO onto the AMMF. Clearly, the degree of Zr oxidation is finely controlled, in part, by the deposition technique. A detailed discussion of the oxidation-reduction chemistry and the resulting interface structure are beyond the scope of the current contribution; they will be addressed in forthcoming publications. Presently, the creation of divergent interfaces in a laminate structure represents a unique lever for controlling characteristics on the small-end of the nanometer scale. Such control provides new avenues for tailoring interfaces and developing the potential of nanoscale electronic devices built from simple metal-insulator materials sets (14).

## References

- (1) Costescu, R. M.; Cahill, D.; Fabreguette, F.; Sechrist, Z.; George, S. *Science* **2004**, *303*, 989–990.
- (2) Chiritescu, C.; Cahill, D.; Nguyen, N.; Johnson, D.; Bodapati, A.; Keblinski, P.; Zschack, P. *Science* **2007**, *315*, 351–353.
- (3) Brennecka, G.; Parish, C.; Tuttle, B.; Brewer, L. *J. Mater. Res.* **2008**, *23*, 176–181.
- (4) Wang, Y.; Li, J.; Hamza, A. V.; Barbee, T. W. *Proc. Natl. Acad. Sci. U.S.A.* **2007**, *104*, 11155–11160.
- (5) Elam, J. W.; Sechrist, Z. A.; George, S. M. *Thin Solid Films* **2002**, *414*, 43–55.
- (6) Cho, M.-H.; Roh, Y. S.; Whang, C. N.; Jeong, K.; Choi, H. J.; Nam, S. W.; Ko, D.-H.; Lee, J. H.; Lee, N. I.; Fujihara, K. *Appl. Phys. Lett.* **2002**, *81*, 1071–1073.
- (7) Leskela, M.; Kemell, M.; Kukli, K.; Pore, V.; Santala, E.; Ritala, M.; Lu, J. *Mater. Sci. Eng., C* **2007**, *27*, 1504–1508.
- (8) Sechrist, Z. A.; Fabreguette, F. H.; Heintz, O.; Phung, T. M.; Johnson, D. C.; George, S. M. *Chem. Mater.* **2005**, *17*, 3475–3485.
- (9) Grubbs, R. K.; Nelson, C. E.; Steinmetz, N. J.; George, S. M. *Thin Solid Films* **2004**, *467*, 16–27.
- (10) Karakaya, K.; Barcones, B.; Rittersma, Z.; van Berkum, J.; Verheijen, M.; Rijnders, G.; Blank, D. *Mater. Sci. Semicond. Process.* **2006**, *9*, 1061–1064.
- (11) Anderson, J.; Munsee, C.; Hung, C.; Herman, T. P. G.; Johnson, D.; Wager, J.; Keszler, D. *Adv. Funct. Mater.* **2007**, *17*, 2117–2124.
- (12) Meyers, S.; Anderson, J.; Hong, D.; Hung, C.; Wager, J.; Keszler, D. *Chem. Mater.* **2007**, *19*, 4023–4029.
- (13) Sharma, P.; Zhang, W.; Amiya, K.; Kimura, H.; Inoue, A. *J. Nanosci. Nanotechnol.* **2005**, *5*, 420–424.
- (14) Reuss, R.; Chalamala, B.; Moussessian, A.; Kane, M.; Kumar, A.; Zhang, D.; Rogers, J.; Hatalis, M.; Temple, D.; Moddel, G.; Eliasson, B.; Estes, M.; Kunze, J.; Handy, E.; Harmon, E. *Proc. IEEE* **2005**, *93*, 1239–1256.

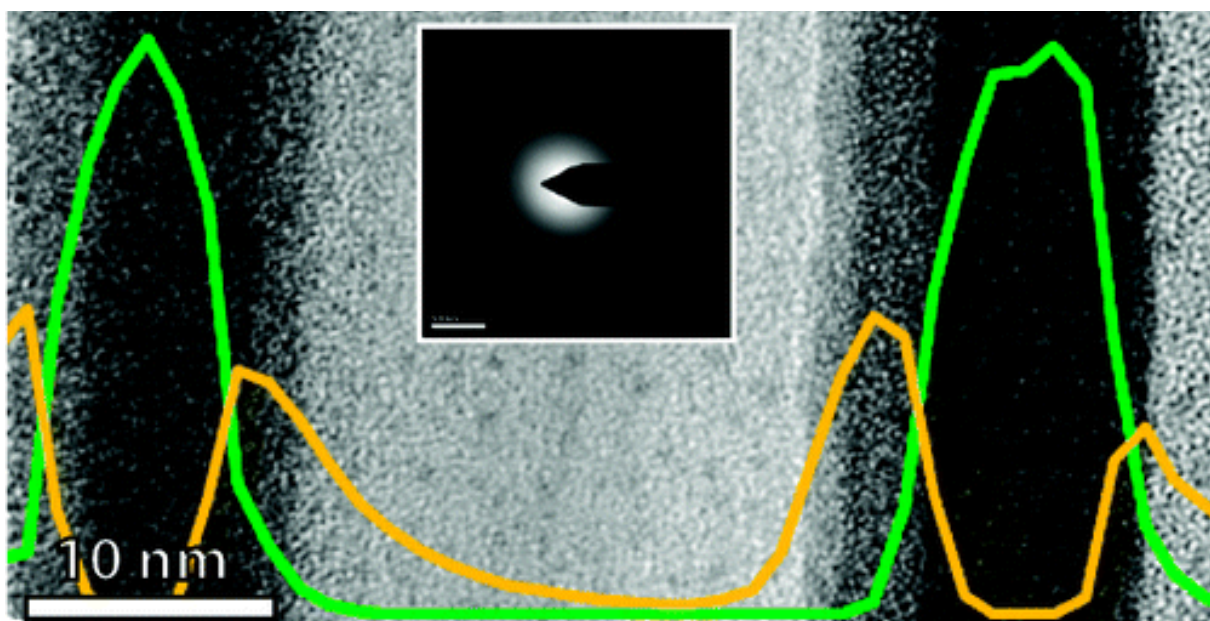


Figure A.1.6. Cover Art detailing XPS profile of Zr(0) and Zr(IV) in green and yellow respectively with inset electron diffraction displaying the amorphousness of the system.

## Appendix A.2

# ADVANCING MIM ELECTRONICS: AMORPHOUS METAL ELECTRODES

E. William Cowell III , Nasir Alimardani , Christopher C. Knutson , John F. Conley Jr. ,  
Douglas A. Keszler , Brady J. Gibbons , and John F. Wager

Published in *Advanced Materials*, **2011**, 23, 74.

Effectively controlling quantum mechanical tunneling through an ultrathin dielectric represents a fundamental materials challenge in the quest for high-performance metal-insulator-metal (MIM) diodes. Such diodes are the basis for alternative approaches to conventional thin-film transistor technologies for large-area information displays, [ 1 , 2 ] various types of hot electron transistors, [ 2–6 ] ultrahigh speed discrete or antenna-coupled detectors, [ 7–14 ] and optical rectennas. [ 15 ] MIM diodes have been fabricated by anodization, [ 1 ] thermal oxidation, [ 8–11 , 14 ] plasma oxidation, [ 10 , 12 , 13 ] or plasma nitridation [ 16 ] of crystalline metal films. Diodes fabricated using these approaches have invariably exhibited poor yield and performance. These problems are to a large extent a consequence of the roughness of the surface of the crystalline metal film, which is often larger than the thickness of the MIM insulator. As a result, the electric field across a MIM device will be highly non-uniform, making the control of quantum mechanical tunneling problematic. In this contribution, we describe the use of an amorphous metal contact as a critical component for circumventing the surface roughness and field uniformity roadblocks that have precluded the realization and utility of MIM electronics for applications requiring high device current rectification ratios (e.g. display applications).

The MIM diode is the fundamental building block of metal-insulator electronics. The device is characterized by a high degree of nonlinearity in its current-voltage characteristics

as a result of a large difference in conductivity between on and off states. The operational theory of this diode, based on Fowler-Nordheim tunneling, has been described in detail by Simmons. [ 17 , 18 ] The probability of quantum mechanical tunneling depends exponentially on the thickness of the insulator between a pair of metal electrodes. Hence, the performance of the diode is critically dependent on the thickness uniformity of the tunnel-dielectric layer across the entire device. Interfacial roughness and dielectric imperfections give rise to alternate conduction mechanisms, e.g. Frenkel Poole emission, that can dominate at low voltages and reduce the device rectification ratio. The inability to create and effectively control a uniform electric field across the whole device area has been the primary limitation in producing reliable MIM devices. Here, we demonstrate that the necessary field control can readily be achieved by integrating the atomically smooth-surface of an amorphous metal electrode with high-quality insulators. This combination provides a rich materials and processing palette for development of MIM electronics, enabling new strategies for device design and fabrication.

Amorphous metals have been primarily investigated as bulk materials, addressing diverse applications that range from micromachines and hinges for digital light processors to golf clubs and transformer cores. [ 19–21 ] They have also been deposited in thin-film form, primarily for study and development of microelectromechanical systems. [ 22–27 ] Relative to crystalline metals, they are more electrically resistive by approximately two orders of magnitude. [ 28 , 29 ] While this resistivity limits their use as interconnects, it is not an impediment to their use as electrodes. To date, however,

there have been no reports involving the use of amorphous metal films as electrodes in electronic devices.

Our investigation of amorphous metal films as electrode materials was stimulated by the smooth surfaces reported for the amorphous metal ZrCuAlNi in thin-film form. [ 25 , 26 ] We hypothesized that the availability of such a smooth surface would provide the basis for a fl at metal-insulator interface, producing an MIM device with a uniform and homogeneous electric field over large areas. Initial characterization of a ZrCuAlNi film deposited via DC sputtering revealed an rms roughness of  $\sim 0.2$  nm with maximum excursions to 1.7 nm in an area of  $5 \mu\text{m} \times 5 \mu\text{m}$  ( Figure A.2.1 a ). For comparison, the rms roughness of a thermally-evaporated crystalline Al film is 5 nm with excursions as high as 70 nm (Figure A.2.1b ); this degree of surface roughness is not surprising given the tendency for elemental metals to crystallize, even when deposited at room temperature. [ 30 ]

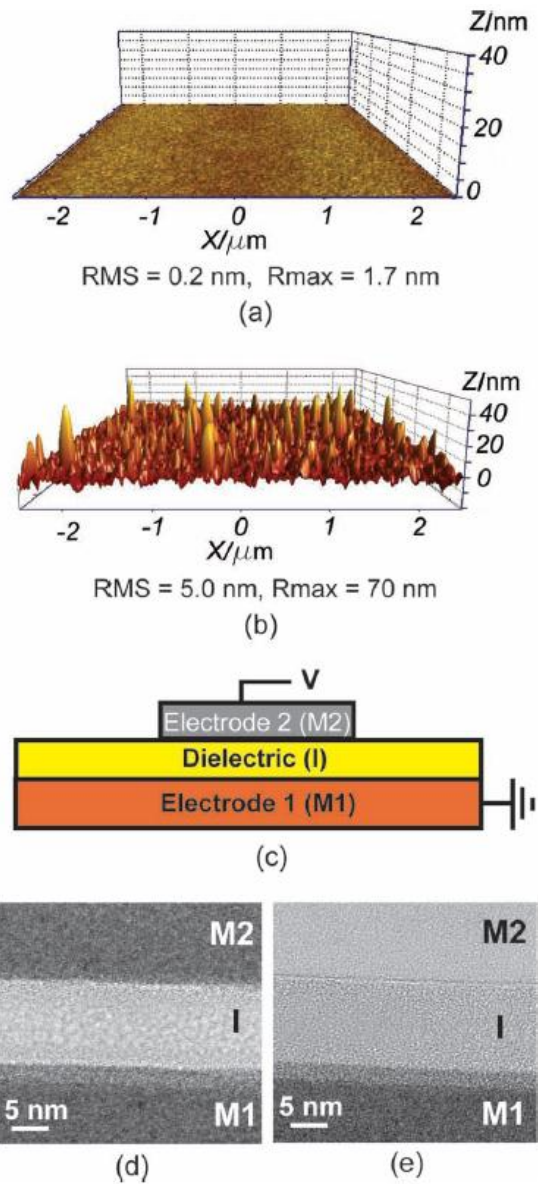
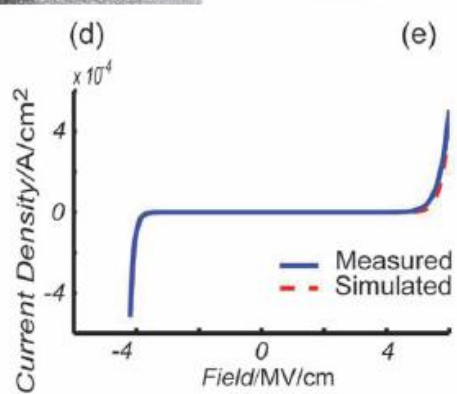
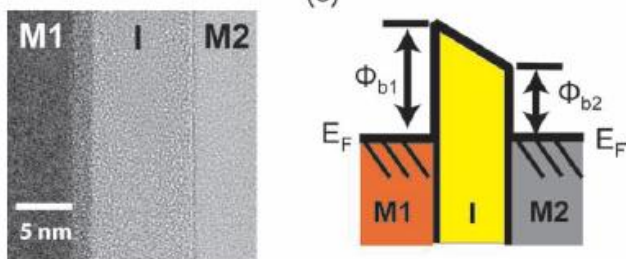
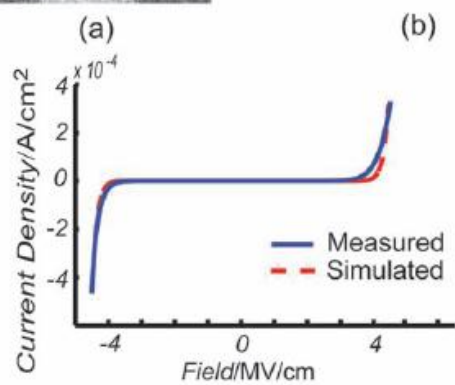
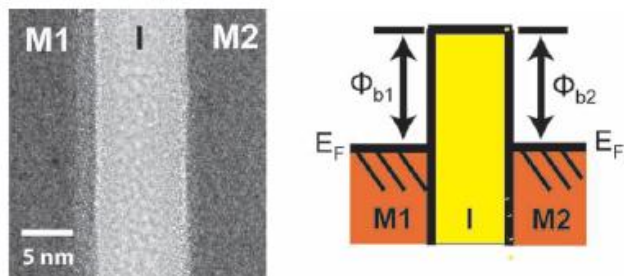


Figure A.2.7. a) An AFM image of the surface of a 100-nm ZrCuAlNi amorphous metal film. b) AFM sectional analysis of the surface of a 150-nm Al blanket. c) Schematic representation of an MIM diode. d) TEM image of an MIM diode; M1 = ZrCuAlNi, I =  $\text{Al}_2\text{O}_3$ , M2 = ZrCuAlNi. e) TEM image of an MIM diode; M1 = ZrCuAlNi, I =  $\text{Al}_2\text{O}_3$ , M2 = Al.

Clearly, the ZrCuAlNi amorphous metal film exhibits a much smoother surface than that of a typical crystalline metal. The initial MIM diodes fabricated for electrical characterization are schematically represented in Figure A.2.1c . The devices are built from a blanket coat of 200 nm of a ZrCuAlNi amorphous metal film electrode (M1) on  $\text{SiO}_2$  , an approximately 10-nm thin film of  $\text{Al}_2\text{O}_3$  produced by atomic-layer deposition (ALD), and upper electrodes (M2) as arrays of 1- $\mu\text{m}$  diameter dots of ZrCuAlNi or Al metal. As seen in TEM images (Figure A.2.1d and e ), the selected materials and processes afford uniform films and well-defined metal/insulator interfaces. Note from Figure A.2.1d and e that a native oxide  $\sim 1.5$  nm thick is present at the M1/insulator interfaces for both MIM diodes. X-ray photoelectron spectroscopy assessment of this native oxide indicates it to be predominantly  $\text{ZrO}_2$  . [ 31 ]

Figure A.2.8. a) TEM image of a symmetric MIM diode fabricated with M1 = ZrCuAlNi amorphous metal film, I = 10 nm Al<sub>2</sub>O<sub>3</sub>, M2 = ZrCuAlNi amorphous metal film. b) Equilibrium energy-band diagram for a symmetric MIM diode. c) Measured and simulated current density-field ( $J-\xi$ ) curves for the MIM diode shown in (a). d) TEM image of an asymmetric MIM diode fabricated with M1 = ZrCuAlNi amorphous metal film, I = 10 nm Al<sub>2</sub>O<sub>3</sub>, M2 = Al. e) Equilibrium energy band diagram for an asymmetric MIM diode. f) Measured and simulated  $J-\xi$  curves for the MIM diode shown in (d). A positive electric field corresponds to application of a positive voltage to electrode M2.



(f)

The MIM diode, constructed using ZrCuAlNi amorphous metal films for both M1 and M2 electrodes, is a symmetric device; the associated equilibrium energy-band diagram is shown in Figure A.2.2b . This diode has equivalent barriers ( $\phi_{b1} = \phi_{b2}$ ) at the metal/insulator interfaces, giving rise to a symmetric current density-applied electric field ( $J$ - $\xi$ ) curve (Figure A.2.2c ). Symmetric MIM diodes with ZrCuAlNi amorphous metal electrodes have been fabricated with yields >70%. (In contrast, we were unable to fabricate even a single working MIM diode when using 10 nm Al<sub>2</sub>O<sub>3</sub> and symmetric evaporated Al electrodes, even though we employed the same high-quality, conformal ALD Al<sub>2</sub>O<sub>3</sub> dielectric.) In the amorphous-metal diodes, negligible current flow is observed until the magnitude of the electric field exceeds 3.5 MV/cm. These devices are quite stable as repeated voltage sweeps reveal no hysteresis. This performance is consistent with the high quality of the individual films and the resulting uniform electric fields. These characteristics are particularly noteworthy, considering the relatively large areas of the individual devices ( $\sim 1 \text{ mm}^2$ ).

In contrast, the MIM diode with ZrCuAlNi as the lower electrode (M1) and Al as the upper electrode (M2) possesses asymmetric barriers ( $\phi_{b1} > \phi_{b2}$ ; Figure A.2.2e ), leading to the asymmetric  $J$ - $\xi$  curve shown in Figure A.2.2f . As seen in Figure A.2.2f , tunneling currents on the order of microamps occur at fields above 4 MV/cm for negative polarity and above 5 MV/cm for positive polarity, confirming the expected asymmetric behavior. The barrier height asymmetry for this device is approximately 0.8 eV, since the work functions of the ZrCuAlNi and Al metal films are measured via Kelvin probe to be 4.8 and 4.0 eV, respectively. These asymmetric MIM diodes possess

desirable yield and performance properties similar to those of the symmetric MIM devices discussed previously, even though the upper Al electrode is crystalline with a normally rough surface (Figure A.2.1b ). The roughness of this surface is not relevant, as the insulator/Al interface is smooth due to the planarity of the ALD  $\text{Al}_2\text{O}_3$ . Thus, it appears that the key to obtaining a high-performance MIM diode is to insure that the initial metal surface is ultra-smooth. The TEM image (Figure A.2.2d ) reveals sharp and uniform interfaces.

Measured  $J - \xi$  curves for symmetric and asymmetric MIM tunnel diodes, as shown in Figure A.2.2c and 2f , can be accurately simulated by using the theory of Simmons, [ 17 , 18 ] confirming that Fowler-Nordheim tunneling indeed dominates at both positive and negative fields. The agreement between measured and simulated  $J - \xi$  curves for the asymmetrical MIM tunnel diode (Figure A.2.2f ) is particularly good. The simulated symmetrical MIM diode  $J - \xi$  curve (Figure A.2.2c ) is less satisfying, since a noticeable deviation occurs for the positive polarity, corresponding to additional or greater than predicted electron tunnel injection from the top  $\text{Al}_2\text{O}_3 / \text{ZrCuAlNi}$  interface. We attribute this discrepancy to the use of DC magnetron sputtering for deposition of the upper ZrCuAlNi electrode. In this process, depositing species have energies on the order of 2–7 eV, [ 30 ] which appears to be sufficient to slightly thin and roughen the tunnel insulator (see Figure A.2.2a ). In contrast, thermal evaporation, a low-energy process that imparts only thermal energy to the  $\text{Al}_2\text{O}_3$  tunnel-barrier surface, is employed in the construction of the upper Al electrode in the asymmetric MIM tunnel diode. Here, a much smaller positive polarity difference between measured and simulated  $J - \xi$  curves

(Figure A.2.2f) is witnessed. The associated TEM image shows the insulator/M2 interface to be pristine (Figure A.2.2d).

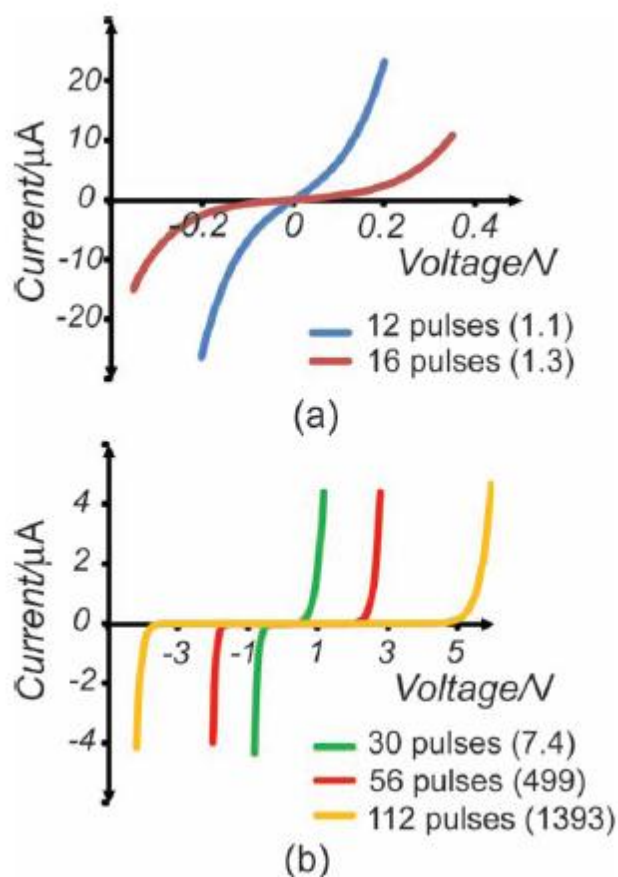


Figure A.2.9. Current-voltage ( $I$ - $V$ ) curves of asymmetric MIM diodes fabricated with M1 = ZrCuAlNi amorphous metal film, I =  $\text{Al}_2\text{O}_3$ , and M2 = Al. a)  $I$ - $V$  characteristics for MIM diodes with ultrathin tunnel barriers ( $< 2$  nm). b)  $I$ - $V$  curves for 30, 56, 112 ALD pulses of  $\text{Al}_2\text{O}_3$ . Asymmetry parameters for devices are given in parentheses. A positive voltage corresponds to application of a positive voltage to electrode M2.

Current-voltage ( $I$ - $V$ ) curves for a series of asymmetric ZrCuAlNi- $\text{Al}_2\text{O}_3$ -Al MIM diodes with variable tunnel-barrier thicknesses are presented in Figure A.2.3. The insulator thickness is specified in terms of ALD pulse cycles, i.e., alternating purge-

separated pulses of trimethylaluminum and deionized water. As a point of reference, 112 pulse cycles has been measured to correspond to an  $\text{Al}_2\text{O}_3$  thickness of approximately 10 nm. At a small number of pulse cycles, the thickness of the ALD-deposited  $\text{Al}_2\text{O}_3$  is difficult to measure. The pulse cycles/thickness relationship becomes less linear as the number of pulse cycles is reduced below 30. In addition, the thickness of the native oxide present on the amorphous metal electrode for the ultrathin deposited layers is an appreciable fraction of the total MIM insulator thickness.

MIM diode applications involving rectification or detection require  $I$ - $V$  curves to be asymmetric, if they are to be operated without an offset bias. [ 11 , 15 ] As shown in Figure A.2.3a , diodes with ultrathin  $\text{Al}_2\text{O}_3$  insulators exhibit nonlinear behavior but very little  $I$ - $V$  curve asymmetry. (For comparison,  $I$ - $V$  asymmetry is quantitatively defined as the ratio of the positive-to-negative polarity current at an electric-field magnitude of 4 MV/cm. The asymmetry evaluated in this manner is specified in parentheses in Figure A.2.3. These  $I$ - $V$  curves are nearly symmetric, because their insulators are so thin that current from direct tunneling across the insulator dominates at very low applied voltages. (Direct tunneling occurs through a trapezoidal barrier, in contrast to Fowler-Nordheim tunneling through a triangular barrier.)  $I$ - $V$  asymmetry is expected to be pronounced only if the insulator is thick enough to stand off significant direct tunneling current up to the onset of Fowler-Nordheim tunneling.

Figure A.2.3b shows that this changeover occurs between 30 and 56 pulse cycles, where the asymmetry abruptly jumps from 7.4 to 499. Direct tunneling occurs at low voltages for all diodes, regardless of the insulator thickness, and it determines the

magnitude of the zero bias resistance. For MIM tunnel diodes fabricated using 112 and 12 ALD pulse cycles, the zero bias resistance is  $>10^{11} \Omega$  and  $20 \text{ k} \Omega$ , respectively.

To extend the functionality of amorphous metal films and to simplify MIM diode fabrication, two approaches were explored, leveraging the direct oxidation of the amorphous metal electrode and the ease of solution processing. First, a blanket amorphous metal electrode was annealed in air to thicken the native Zr(IV) oxide (at  $300 \text{ }^\circ\text{C}$ , a temperature that does not promote crystallization of the amorphous metal). After the anneal, Al electrodes were thermally deposited to complete the structure. A representative  $I$ - $V$  curve for these devices is presented in Figure A.2.4. The  $I$ - $V$  asymmetry of the resulting structure is measured to be 1.2, which is less than that expected from consideration of the differences in electrode work functions. The origin of this discrepancy is under investigation. A second oxidation-based asymmetric MIM diode was fabricated via the incorporation of a solution-deposited aluminum phosphate (AlPO) film [ 32 ] as a portion of the tunnel barrier. An MIM structure was realized by spin coating the AlPO film onto the ZrCuAlNi electrode, annealing in air at  $300 \text{ }^\circ\text{C}$ , and then depositing an Al upper electrode. The device exhibits the onset of significant tunneling currents (Figure A.2.4 ) at voltages higher than those of the devices employing  $\text{Al}_2\text{O}_3$  films produced via ALD. The asymmetry is 0.0015, indicating that the polarity dependence of the current has switched from that seen for the asymmetric diodes fabricated with the  $\text{Al}_2\text{O}_3$  tunnel barriers. We have recently reported significant interdiffusion between the interfaces of ZrCuAlNi and AlPO bilayers in nanolaminated structures. [ 31 ] The presence of the AlPO layer and its interaction with the native

ZrO<sub>2</sub>, formed during annealing, creates an opportunity for controlling the I–V polarity dependence of the MIM diode.

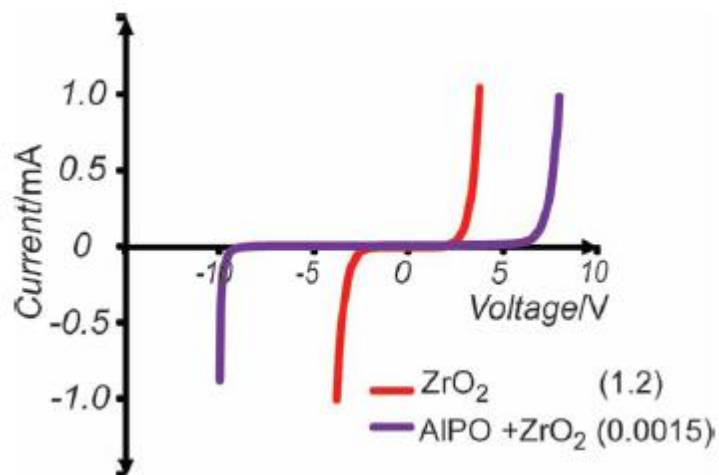


Figure A.2.10. *I*–*V* curves for MIM diodes with M1 = ZrCuAlNi, M2 = Al, and I = ZrO<sub>2</sub> or AlPO + ZrO<sub>2</sub>. The ZrO<sub>2</sub> diode was annealed in air to form the tunnel dielectric. The AlPO + ZrO<sub>2</sub> diode had 10 nm of AlPO deposited onto the surface of the ZrCuAlNi lower electrode and was subsequently annealed in air. Asymmetry parameters for devices are given in parentheses. A positive voltage corresponds to application of a positive voltage to electrode M2.

In summary, high-performance, high rectification ratio MIM diodes employing amorphous metal electrodes have been demonstrated. ZrCuAlNi amorphous metal film lower electrodes have been coupled with high-quality insulators and ZrCuAlNi and Al upper electrodes to produce uniform electric fields for the successful operation of both symmetric and asymmetric diodes. All diodes were fabricated by using relatively low temperatures ( $\leq 300$  °C), rapid DC sputtering of the amorphous metal, and ALD or solution processing for deposition of high-quality insulators. Together, these methods provide opportunities for device fabrication on a variety of substrates, extending to

large areas. In addition, the exceptionally broad compositional space of amorphous metal films provides unique opportunities to modify work functions and tune barrier heights for control of electron tunneling and device operation. Hence, this approach to MIM electronics presents an intriguing new means both for designing very high-performance electronic devices and integrating them across multiple technology platforms.

### **Experimental Section**

*Thin Films* : ZrCuAlNi amorphous metal thin films were deposited onto Si/SiO<sub>2</sub> (100 nm SiO<sub>2</sub>) substrates using DC magnetron sputtering with no intentional substrate heating at a power of 60 W, a pressure of 3 mTorr, and an Ar flow rate of 20 sccm. A 3-inch diameter, 0.25-inch thick vacuum arc-melted metal target (with an atomic composition Zr<sub>40</sub>Cu<sub>35</sub>Al<sub>15</sub>Ni<sub>10</sub>) fabricated by Kamis Inc. was used for all ZrCuAlNi depositions. Atomic layer deposition (ALD) of Al<sub>2</sub>O<sub>3</sub> was carried out in a Picosun SUNALE R-150B ALD reactor using trimethylaluminum (TMA) and de-ionized water at a temperature of 300 °C. The pulse durations for both TMA and water were 0.1 s with a 2-s nitrogen purge between pulses. MIM diode structures were completed by shadow masking ~1 mm diameter top contacts deposited by either thermal evaporation of Al or DC magnetron sputter deposition of ZrCuAlNi films using the deposition parameters described above. The solution-based dielectric depositions were carried out using an aluminum oxide phosphate solution containing a 0.10 M metal concentration at

an aluminum-to-phosphorus ratio of 30:18. [ 32 ] The solution was deposited via spin-coating for 30 s at a speed of 3000 rpm, followed by rapid heating at 300 °C for 1 min on a hotplate in air. Films were annealed in air at 300 °C. Atomic force microscope (AFM) measurements were made using a Digital Instruments 3 instrument with silicon-nitride tips; images were acquired over 5  $\mu\text{m}$  x 5  $\mu\text{m}$  areas. Transmission electron microscopy (TEM) images were obtained with a JEOL 2500 TEM from samples prepared with a Dual Beam FEI 235 focused ion beam. Work function measurements were performed in air by using a KP Technology SKP5050 scanning Kelvin probe with a 2-mm tip calibrated against a gold standard. The work function analysis was carried out over an area of approximately 1 mm x 1 mm. Electrical measurements were performed by using a Hewlett-Packard 4156C semiconductor parameter analyzer. The blanket lower ZrCuAlNi electrode was held at ground potential with bias applied to the upper electrode. A dual-sweep measurement was employed to allow for an assessment of current-voltage curve hysteresis. The magnitude of the applied voltage bias was scaled according to the tunnel-barrier thickness to target maximum current levels in the  $\mu\text{A}$  range.

*Current Density-Electric Field Simulation* : Simulation of current density-electric field ( $J-\xi$ ) curves was performed with Matlab, using the Fowler-Nordheim tunneling equations developed by Simmons. [ 17, 18 ] Optimized fits to measured  $J-\xi$  curves, as shown in Figure A.2.2 , were obtained by using an effective mass between 0.45 to 1.0 of the free electron mass,  $\phi_{\text{bZrCuAlNi}} = 2.2 \pm 0.3$  V,  $\phi_{\text{bAl}} = 1.3 \pm 0.1$  V, and adjusting the insulator thickness.

## References

- [ 1 ] W. den Boer, in *Active Matrix Liquid Crystal Displays*, Elsevier, Amsterdam, **2005**.
- [ 2 ] K. K. Ng , in *Complete Guide to Semiconductor Devices*, 2 nd Edition, Wiley-Interscience, New York, **2002**.
- [ 3 ] J. L. Moll, *IEEE Trans. Electron Devices* **1963**, *10*, 299 .
- [ 4 ] S. M. Sze , in *Physics of Semiconductor Devices*, 1 st Ed, Wiley-Interscience, New York, **1969**.
- [ 5 ] *High-Speed Semiconductor Devices* (Ed: S. M. Sze ), Wiley-Interscience, New York , **1990**.
- [ 6 ] S. M. Sze, K. K. Ng, in *Physics of Semiconductor Devices*, 3 rd Edition, Wiley-Interscience, Hoboken, New Jersey, **2007**.
- [ 7 ] S. P. Kwok, G. I. Haddad, G. Lobov, *J. Appl. Phys.* **1971**, *42*, 554.
- [ 8 ] G. M. Elchinger, A. Sanchez, C. F. Davis, A. Javan, *J. Appl. Phys.***1976**, *47*, 591.
- [ 9 ] M. Heiblum, S. Wang, J. R. Whinnery, T. K. Gustafson, *IEEE J. Quantum Electron.* **1978**, *14*, 159.
- [ 10 ] M. Brunner, H. Ekrut, A. Hahn, *J. Appl. Phys.* **1982**, *53*, 1596.
- [ 11 ] E. N. Grossman, T. Harvey, C. D. Reintsema, *J. Appl. Phys.* **2002**, *91*, 10134.
- [ 12 ] P. C. D. Hobbs, R. B. Laibowitz, F. R. Libsch, *Appl. Optics* **2005**, *44*, 6813.
- [ 13 ] S. Krishnan, E. Stefanakos, S. Bhansali, *Thin Solid Films* **2008**, *516*, 2244 .
- [ 14 ] J. A. Bean, B. Tiwari, G. H. Bernstein, P. Fay, W. Porod *J. Vac. Sci. Technol. B* **2009**, *27*, 11.
- [ 15 ] B. Berland, National Renewable Energy Laboratory Final Report, **2003**, see: <http://www.nrel.gov/docs/fy03osti/33263.pdf>.
- [ 16 ] G. Lewicki, C. A. Mead, *Phy. Rev. Lett.* **1966** , *16*, 939.

- [ 17 ] J. G. Simmons , *J. Appl. Phys.* **1963**, *34*, 1793.
- [ 18 ] J. G. Simmons, *J. Appl. Phys.* **1963**, *34*, 2581.
- [ 19 ] H. Warlimont , *Mater. Sci. Eng. A* **2001** , *304* , 61 .
- [ 20 ] J. Tregilgas, *Adv. Mater. Proc.* **2005**, *163*, 46.
- [ 21 ] A. Greer, E. Ma, *MRS Bull.* **2007**, *32*, 611.
- [ 22 ] S. Hata, K. Sato, A. Shimokohbe, *Proc, SPIE* **1999**, 3892, 97.
- [ 23 ] Y. Liu, S. Hata, K. Wada, A. Shimokohbe, *Jpn. J. App. Phys.* **2001**, *40*, 5382.
- [ 24 ] J. P. Chu, C. T. Liu, T. Mahalingam, S. F. Wang, M. J. O'Keefe, B. Johnson , C. H. Kuo, *Phys. Rev. B* **2004**, *69*, 113410.
- [ 25 ] P. Sharma, W. Zhang, K. Amiya, H. Kimura, A. Inoue, *J. Nanosci.Nanotechnol.* **2005**, *5*, 416.
- [ 26 ] P. Sharma, N. Kaushik, H. Kimura, Y. Saotome, A. Inoue, *Nanotechnology* **2007**, *18*, 035302.
- [ 27 ] F. X. Liu, P. K. Liaw, W. H. Jiang, C. L. Chiang, Y. F. Gao, Y. F. Guan, J. P. Chu, P. D. Rack, *Mater. Sci. Eng. A* **2007**, *468*, 246.
- [ 28 ] N. F. Mott, in *Conduction in Non-Crystalline Materials* , Oxford University Press, Oxford , **1993** .
- [ 29 ] J. Dugdale, in *The Electrical Properties of Disordered Metals*, Cambridge University Press, Cambridge **2005** .
- [ 30 ] M. Ohring, in *Materials Science of Thin Films*, 2nd Ed., Academic Press, San Diego, **2001**.
- [ 31 ] E. W. Cowell III, C. C. Knutson, J. F. Wager, D. A. Keszler, *Appl.Mater.Interfaces* **2010**, *2*, 1811.
- [ 32 ] S. T. Meyers, J. T. Anderson, D. Hong, C. M. Hung, J. F. Wager, D. A. Keszler, *Chem. Mater.* **2007**, *19*, 4023.

## Appendix A.3

### Engineering Anisotropic Dielectric Response Through Amorphous Laminate Structures

E. William Cowell III, Christopher C. Knutson, Nicholas A. Kuhta, William Stickle,  
Douglas A. Keszler, and John F. Wager

**This work has been submitted to *Physica Status Solidi (a)*, 2011**

## Introduction

Dispersion engineering is defined in the context of this contribution as the control of electromagnetic radiation through material dielectric properties. The dawn of dispersion engineering can be traced to early attempts to focus electromagnetic radiation in the optical frequency range. Indeed, evidence exists suggesting crystalline lenses were fabricated by ancient Egyptians.<sup>[1]</sup> A significant advance in dispersion engineering occurred in 13<sup>th</sup> century Italy with the development of spectacles, greatly expanding the reach of the printed word.<sup>[2]</sup>

In modern times, interest in dispersion engineering has been renewed around the concept of negative refraction through isotropic dispersion.<sup>[3]</sup> The mathematical treatment of electromagnetic radiation through Maxwell's equations provided evidence that negative refraction could, for example, produce a perfect lens if a suitable material could be fabricated. The turn of the 20<sup>th</sup> century saw the mathematics describing negative refraction modernized,<sup>[4]</sup> which in turn catalyzed intense efforts to fabricate new materials and measure negative refraction. Most of these studies have been focused on materials structures with a high degree of fabrication complexity. Recognition of laminate material anisotropy provided the breakthrough concept necessary to fabricate materials exhibiting anomalous dispersion<sup>[5, 6]</sup> and to produce precisely measurable dispersion effects. Recent dispersion engineering literature describing anisotropic materials systems exhibiting anomalous dispersion of incident light has increased dramatically since 2002.<sup>[7-13]</sup>

In this contribution, we address dispersion engineering through fabrication and study of new nanolaminates containing thin amorphous-metal and solution-processed-oxide films. We have recently described the materials properties and film interfacial chemistry of these highly regular laminated structures.<sup>[14]</sup> The smooth and pristine interfaces between the amorphous metal and oxide have also enabled the realization of high-performance metal-insulator-metal diodes.<sup>[15]</sup> These findings have prompted us to examine their behavior as a new type of anisotropic dielectric medium.

To appreciate the advances in dispersion engineering enabled by these amorphous composite materials, we first describe the differences between isotropic and anisotropic dispersion. The following discussion of dispersion is focused on non-magnetic materials ( $\mu = 1$ ). Additionally, the materials described are planar in nature and are represented by an abrupt change in index of refraction in the  $z$  direction as light passes into the plane of the material. In planar structures with small out of plane scattering, momentum is conserved to a single plane represented by 2 dimensions. The mathematics used to describe the dispersion effects observed in planar structures are, therefore, presented in two dimensions.

The dielectric response,  $\epsilon$ , of a planar isotropic material that does not exhibit directional dependence is described as

$$k_{xy}^2 + k_z^2 = n^2 \frac{\omega^2}{c^2} = \epsilon \frac{\omega^2}{c^2}, \quad (1)$$

where  $k_{xy}$  is the light's momentum component in the plane of the material,  $k_z$  is the momentum component orthogonal to the material interfaces,  $n$  is the material's index of refraction,  $\omega$  is the angular frequency of the light, and  $c$  is the speed of light in vacuum. The engineered dispersion of incident light is accomplished solely through the modulation of  $\epsilon$ , which is a complex number varying with the frequency of the incident light. As light encounters a change in  $\epsilon$ , as it passes from free space ( $\epsilon=1$ ) to a material with  $\epsilon \neq 1$ , the direction of the light's momentum ( $\vec{K}$ ) changes due to a magnitude change in the  $z$  component of the light's momentum ( $k_z$ ). The Poynting vector ( $\vec{S}$ ) represents the direction of energy flux, and is coincident with  $\vec{K}$  in an isotropic dielectric material. Figure A.3.1(a) illustrates the response of light as it passes into an isotropic dielectric material from air. The described dispersive effect, through the use of isotropic dielectric materials with  $\epsilon \neq 1$ , is the means through which light was manipulated via dispersion engineering by the ancient Egyptians.<sup>[1]</sup>

The dielectric response of layered, anisotropic, dielectric materials has two components;  $\epsilon_{xy}$  in the plane of the material interfaces and  $\epsilon_z$  orthogonal to the plane of the material interfaces. Anisotropic dispersion is exhibited only with  $T_M$  polarized light.  $T_M$  polarization stipulates that the magnetic field vector is parallel to the material

plane as shown in Figure A.3.1(b) and (c). The electric field in  $T_M$  polarized light is influenced by both components of the material dielectric response. Two dielectric response components lead to a dispersion equation

$$\frac{k_x^2}{\epsilon_z} + \frac{k_z^2}{\epsilon_{xy}} = \frac{\omega^2}{c^2}, \quad (2)$$

where  $\epsilon_z$  is the dielectric response orthogonal to the material plane and  $\epsilon_{xy}$  is the dielectric response in the material plane. A condition of anisotropic dispersion is that  $\epsilon_z \neq \epsilon_{xy}$ . Isotropic and anisotropic materials may possess dielectric responses with real components being either positive or negative polarity. A negative real component of a dielectric response is typically indicative of a metallic material in which electromagnetic waves decay due to the fast rearrangement of free charge.

The mathematics describing an anisotropic material possessing two distinct dielectric responses,  $\epsilon_z$  and  $\epsilon_{xy}$ , allow for three distinct dispersion effects based on the polarity of  $\text{Re}(\epsilon_z)$  and  $\text{Re}(\epsilon_{xy})$ . Figure 1(b) illustrates anisotropic, elliptical dispersion which occurs when both  $\text{Re}(\epsilon_z)$  and  $\text{Re}(\epsilon_{xy})$  are positive. Anisotropic, elliptical dispersion separates  $\vec{K}$  and  $\vec{S}$  as light propagates in the anisotropic material. Anisotropic, hyperbolic dispersion, presented in Figure A.3.1(c), occurs when  $\text{Re}(\epsilon_z)$  and  $\text{Re}(\epsilon_{xy})$

possess opposite signs. Negative refraction occurs when  $\text{Re}(\epsilon_z) < 0$  and  $\text{Re}(\epsilon_{xy}) > 0$ , whereas hyperbolic dispersion with positive refraction occurs when  $\text{Re}(\epsilon_z) > 0$  and  $\text{Re}(\epsilon_{xy}) < 0$ . Anisotropic materials fabricated in this research possess measured reflectance characteristic of both anisotropic, elliptical dispersion and hyperbolic dispersion with positive refraction.

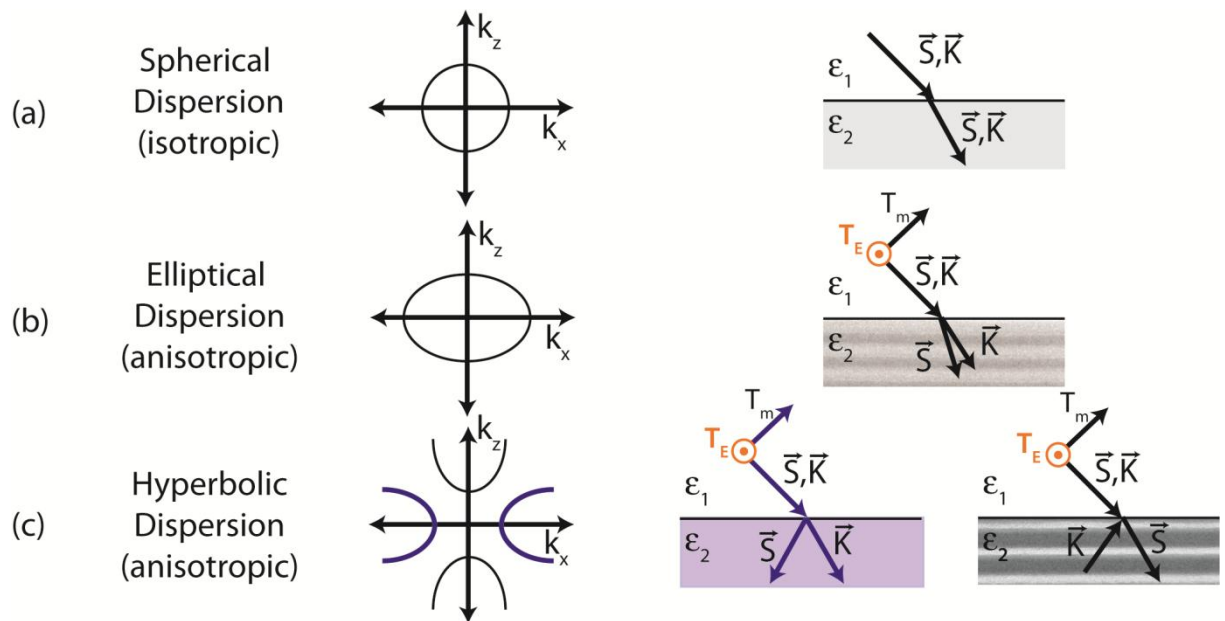


Figure A.3.1. Graphical representation of the mathematical dispersion equations and resulting dispersion of incident light incident on (a) spherical isotropic materials, (b) elliptical anisotropic materials, and (c) hyperbolic anisotropic materials. Laminate structures shown in (b) and (c) are taken from transmission electron microscope (TEM) micrographs of laminate materials fabricated by the authors.

## Results and Discussion

To assess the optical dielectric properties of the amorphous metal/oxide laminates, structures containing ten bilayers were fabricated. Two amorphous metals, ZrCuAlNi

and  $\text{TiAl}_3$ , and amorphous aluminum phosphate oxide (AIPO) were used to fabricate the stacks. The use of two different amorphous metals allows us to attribute differences in dielectric properties to the effects of the amorphous metals.

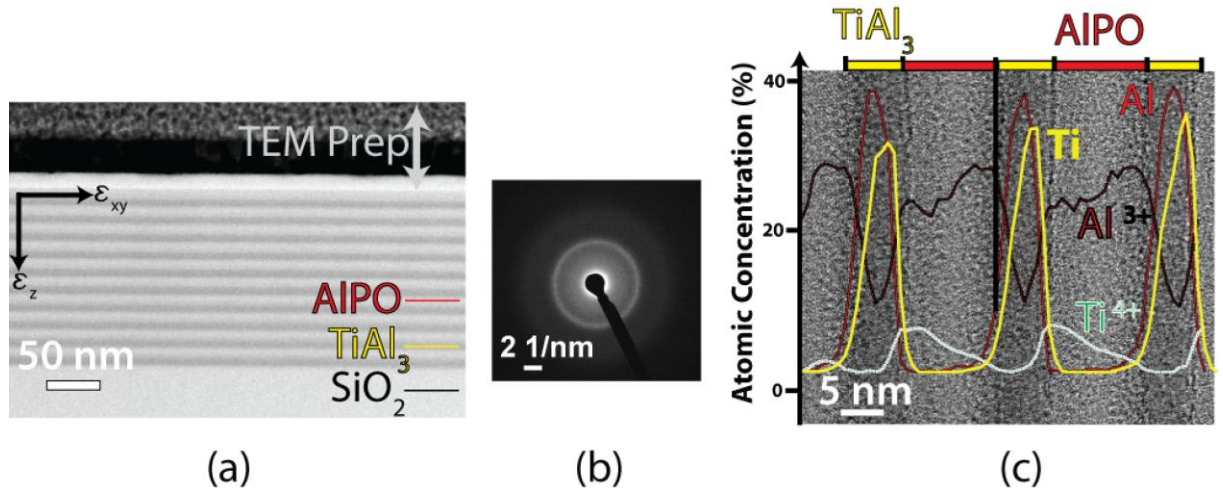


Figure A.3.2. Materials analysis data of an anisotropic, dispersion, laminate material fabricated with  $\text{TiAl}_3/\text{AIPO}$  bilayers. (a) TEM micrograph of a 10 bilayer  $\text{TiAl}_3/\text{AIPO}$  laminate. (b) Electron diffraction pattern of the laminate structure shown in (a). (c) X-ray photoelectron spectroscopy (XPS) depth profile overlaid on a TEM micrograph taken through a laminate fabricated concurrently with the laminate shown in the TEM images.

Materials analysis data for a ten bilayer  $\text{TiAl}_3/\text{AIPO}$  laminate structure are given in Figure A.3.2. As seen in Figure A.3.2(a), highly ordered structures and well-defined interfaces are realized with a bilayer thickness of 16 nm. During the transmission electron microscopy (TEM) imaging, the extent of the TEM sample was inspected for defects. No defects were revealed. Therefore, the image is representative of the laminate across a larger area than shown in the figure. Our overall experience with the laminates

indicates that they are homogeneous over the surface of the substrate. Diffuse rings are observed in the diffraction pattern of Figure A.3.2(b), providing evidence that the laminate is amorphous. X-ray photoelectron spectroscopy (XPS) depth profiling was performed through a laminate fabricated concurrently with the laminate presented in Figure A.3.2(a) to generate the overlaid XPS data shown in Figure A.3.2(c). The image reveals that the bilayer composition profile is faithfully repeated through the structure. The same high level of bilayer material repeatability is observed in ZrCuAlNi/AlPO laminates, as has been previously reported.<sup>[14]</sup> Existing examples of dispersion engineering at optical frequencies via amorphous materials (glass lenses) have been successful, in part, because of the ease and reproducibility of amorphous material systems. The extension of dispersion engineering through amorphous laminate materials benefits from the same amorphous fabrication advantages. Precisely repeated bilayer thicknesses and stoichiometries are essential for the realization of high quality metamaterials.

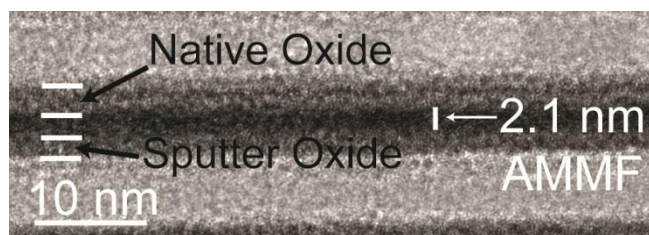


Figure A.3.3. TEM micrograph of ZrCuAlNi/AlPO laminate illustrating lower limit of amorphous metal layer thickness. The oxide layer on top of the ZrCuAlNi layers is a native oxide. The oxide layer on the bottom of the ZrCuAlNi is formed through the sputter deposition of the ZrCuAlNi onto the AlPO layer. The thickness of the continuous ZrCuAlNi layer is 2.1 nm.

Amorphous metal films, as presented in Figure A.3.3, have been deposited via DC magnetron sputtering as ultra-smooth, homogenous films with a minimum thickness of 2 nm. Oxidation of an amorphous metal film deposited via sputtering occurs at interfaces above and below the film.<sup>[14]</sup> Below the film, the energy of sputter deposition supplies the driving force of oxidation, creating the sputter oxide shown in Figure A.3.3. The native oxide, on top of the deposited film, occurs when the film is exposed to ambient oxygen as substrates are processed using the solution deposition of amorphous oxide films. Both the sputter oxide and native oxide of amorphous metal films are repeatable in thickness, when deposition process conditions are consistent, as revealed via the XPS profile shown Figure A.3.2(c). Repeatable oxidation leads to repeatable thin film thicknesses, which allows for the use of amorphous metal films in anisotropic dielectric laminate materials. Amorphous oxide films, deposited via solution processing, have minimum thicknesses less than 3 nm.<sup>[16]</sup> The minimum bilayer thickness (i.e., thickness of amorphous metal and amorphous oxide films) is limited by the oxidation of the amorphous metal, and is on the order of 10 nm. Laminates fabricated with bilayers of 10 nm thickness satisfy the quasi-static condition for light in the deep UV regime, i.e.,  $\leq 193$  nm.

Effective medium theory predicts spatially averaged values of a laminate structure's dielectric response when the bilayer thickness of the laminate is significantly smaller than the wavelength of incident light.<sup>[9]</sup> Under this condition of bilayer thickness, a

quasi-static state is established, where the incident light is affected by the average dielectric responses of the laminate material. The spatial averaging of distinct, isotropic dielectric responses of amorphous metals and oxides into two anisotropic dielectric responses defines  $\varepsilon_z$  and  $\varepsilon_{xy}$  for  $T_M$  polarized light as

$$\varepsilon_z = \frac{\varepsilon_m \varepsilon_o (d_m + d_o)}{\varepsilon_m d_o + \varepsilon_o d_m}, \text{ and} \quad (3)$$

$$\varepsilon_{xy} = \frac{d_m \varepsilon_m + d_o \varepsilon_o}{d_m + d_o}. \quad (4)$$

$\varepsilon_m$  and  $d_m$  are the dielectric response and film thickness, respectively, of the amorphous metal layer, and  $\varepsilon_o$  and  $d_o$  are the dielectric response and film thickness, respectively, of the amorphous oxide layer.

Effective medium theory modeling of ZrCuAlNi/AIPO and TiAl<sub>3</sub>/AIPO laminates reveals the anisotropic dielectric responses,  $\varepsilon_z$  and  $\varepsilon_{xy}$ , of the two laminate materials. Effective medium modeling employs dielectric responses calculated through the use of ellipsometry reflectance data collected from bulk amorphous metal and AIPO films. The

ellipsometry data are gathered using linearly polarized  $T_M$  light of wavelengths between 300 and 1500 nm and incident angles between 20 and 80° at 5 degree increments. The dielectric responses of optically thick amorphous metal samples and AIPO films are calculated using a nonlinear least squares fit of the reflectance data at each wavelength across the 13 unique angular measurements. The thickness of each layer is also input into the model. The calculated anisotropic dielectric responses of the laminates, as well as the calculated isotropic dielectric responses of the amorphous metals and oxide are presented in Figure A.3.4. The shaded yellow region above 600 nm in Figure A.3.4(a) and below 350 nm in Figure A.3.4(b) are frequency ranges where  $T_M$  polarized incident light exhibits anisotropic hyperbolic dispersion with positive refraction. The remainder of the measured frequencies exhibit anisotropic elliptical dispersion.

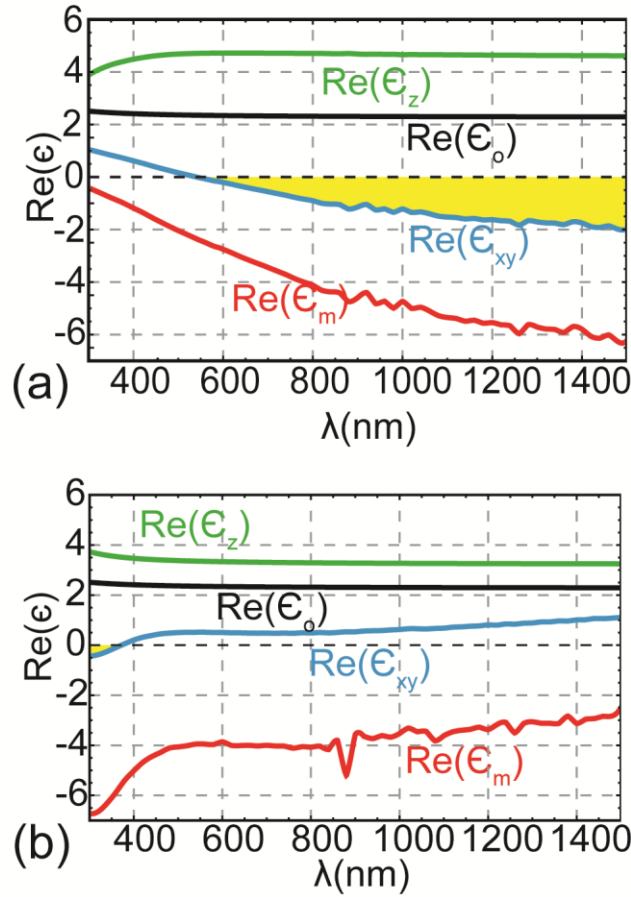


Figure A.3.4. Real components of the complex, isotropic amorphous metal and AlPO dielectric responses along with effective, anisotropic dielectric responses of laminate (a) ZrCuAlNi/AlPO and (b) TiAl<sub>3</sub> structures. Red is the bulk, isotropic dielectric response of the amorphous metal ( $\epsilon_m$ ), black is the isotropic AlPO dielectric response ( $\epsilon_o$ ), blue is the xy-plane dielectric response ( $\epsilon_{xy}$ ), and green is the z (propagation direction) dielectric response ( $\epsilon_z$ ).

The distinct, anisotropic dielectric responses of the two amorphous metal/oxide laminates illustrates the ability to engineer dispersion characteristics based on the bulk dielectric responses of the individual layers. Through investigations into the dielectric responses of different amorphous layer materials, a toolbox of material components is

created. Increased diversity of the available toolbox materials will directly increase the breadth of performance achievable with anisotropic dispersion materials.

The impact of the laminate metal/dielectric thickness ratio on  $\text{Re}(\epsilon_{xy})$  is illustrated in Figure A.3.4. Equation 4 reveals the magnitude of  $\text{Re}(\epsilon_{xy})$  to be thickness scaled values of  $\text{Re}(\epsilon_m)$  and  $\text{Re}(\epsilon_o)$ . Decrease of the metal/dielectric thickness ratio moves  $\text{Re}(\epsilon_{xy})$  in a positive direction, i.e., shifts  $\text{Re}(\epsilon_{xy})$  up. Conversely, an increase of the metal/dielectric thickness ratio will move  $\text{Re}(\epsilon_{xy})$  in a negative direction, i.e., shift  $\text{Re}(\epsilon_{xy})$  down.

The data presented in Figure A.3.4 illustrate the described modulation of  $\text{Re}(\epsilon_{xy})$  through the use of different metal/dielectric ratios. The metal/dielectric thickness ratio in the measured ZrCuAlNi/AlPO laminate is 1:1. As expected from Eq. 4,  $\text{Re}(\epsilon_{xy})$  is seen to be the arithmetical mean of  $\epsilon_m$  and  $\epsilon_o$ . The ratio of metal-to-dielectric thickness in the measured TiAl<sub>3</sub>/AlPO laminate is lower, i.e., less metal. Therefore, Figure A.3.4(b) places  $\text{Re}(\epsilon_{xy})$  closer to the dielectric response of AlPO than to the dielectric response of TiAl<sub>3</sub>. Modulating  $\text{Re}(\epsilon_{xy})$  at a specific wavelength is accomplished through simply changing the layer thickness to change the metal/dielectric ratio. Therefore, anisotropic dispersion materials can be engineered to possess specific dispersion characteristics as required by targeted applications.

The control of  $\text{Re}(\epsilon_z)$  is not as simple as the control of  $\text{Re}(\epsilon_{xy})$ . Equation 3 contains the multiplication of two complex responses,  $\epsilon_m$  and  $\epsilon_o$ . Therefore, modulation of  $\text{Re}(\epsilon_z)$  is influenced by the imaginary components of the bulk material dielectric response as well as layer thickness.  $\text{Re}(\epsilon_z)$  is modulated in a negative direction by minimizing the amorphous metal loss and/or increasing the real component of the oxide dielectric response. The selection of amorphous materials and the scaling of layer thicknesses, therefore, enables precise control of the anisotropic dielectric responses,  $\text{Re}(\epsilon_{xy})$  and  $\text{Re}(\epsilon_z)$ , of amorphous laminate structures.

Alignment between measured and modeled reflectance data from a laminate structure provides an assessment of laminate structure metal/dielectric thickness ratio. The inputs into the laminate structure reflectance model, as described by Eq. 3 and Eq. 4, are the dielectric response and thickness of the laminate component layers and the silicon/silicon dioxide substrate layers. These values are employed in a transfer matrix calculation to model the reflectance expected from the air/laminate interface. The reflectance of the laminate structures is also measured via ellipsometry at wavelengths between 300 and 1500 nm and at angles of incidence between 20 and 80° at 5 degree increments. The calculated anisotropic dielectric response of the laminate structure is determined with the bulk dielectric responses and the layer thicknesses via Eq. 4. The alignment between the measured and modeled data is used as a confirmation of the metal-to-dielectric thickness ratio, and therefore serves as a metrology tool for the

fabrication of laminates exhibiting anisotropic dielectric response. The metric through which measurement-to-model alignment is evaluated is defined as

$$\text{Normalized Error}\% = \left( \sum_{\lambda=300-1500\text{nm}} \frac{R_{meas} - R_{model}}{R_{meas}} \right) \times 100, \quad (5)$$

where  $R_{meas}$  is the measured reflectance value and  $R_{model}$  is the modeled reflectance value at a specific wavelength. The normalized error metric provides a single value across all wavelengths (300 to 1500 nm) at each angle of incidence.

By changing the metal and dielectric thicknesses input to Eq. 4, the modeled reflectance is changed, which, in turn, changes the normalized error. The change in normalized error with respect to metal/dielectric ratio is presented in Figure A.3.5. The metal/dielectric ratio at which the normalized error data is equal to zero is the convergence point of the model and measurement data, and represents the best estimate of actual metal/dielectric ratio. Figure A.3.5(a) is comprised of data from a ZrCuAlNi/AlPO laminate, while Figure A.3.5(b) is comprised of data from a TiAl<sub>3</sub>/AlPO laminate. Normalized error data from both laminate structures behave similarly with respect to metal/dielectric ratio. For dielectric rich ratios, the modeled reflectance data are of lesser magnitude (less predicted reflectance) than the

measurements suggest. Therefore, the normalized error metric is positive for dielectric-rich metal/dielectric ratios.

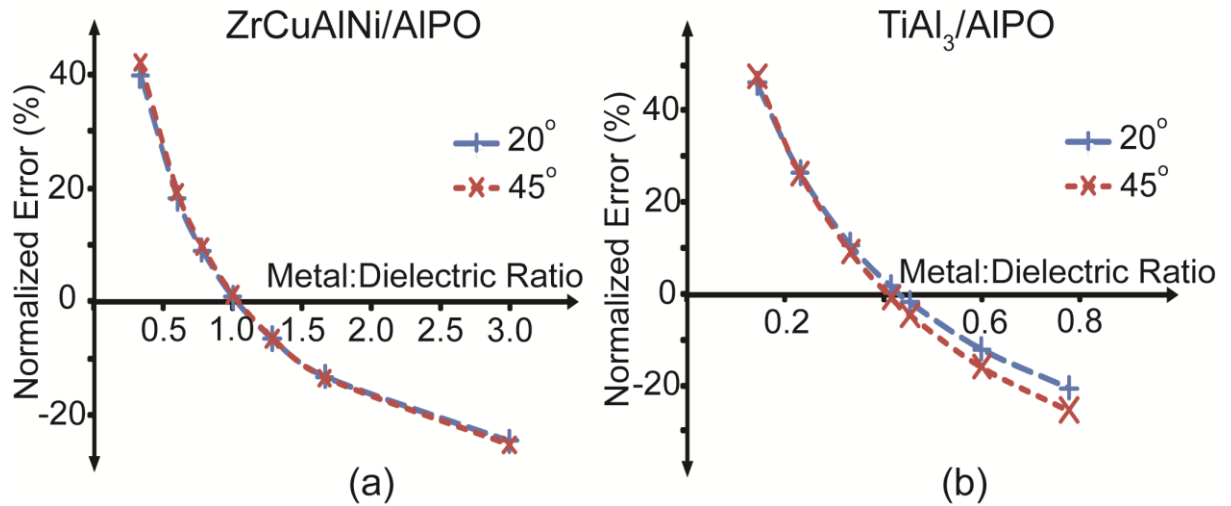


Figure A.3.5. Normalized measured to modeled error versus metal/dielectric ratio of reflectance data collected using  $T_M$  polarized light with laminates fabricated with bilayers comprised of (a) ZrCuAlNi/AlPO and (b) TiAl<sub>3</sub>/AlPO.

Conversely, for metal-rich ratios, the model data predict more reflectance than measured, leading to a negative normalized error. Both conditions are consistent with expected higher reflection from metals and lower reflection from oxide dielectrics.

As noted above, the processing steps lead to oxidation of the amorphous-metal film, which diminishes the effective thickness of the metal. The normalized error analysis, combined with the XPS profile data through the laminate structures, provides insight into the un-oxidized elemental metal content required for an amorphous metal film to behave as a metal. At un-oxidized metal content equal to or greater than the level determined through effective medium modeling, the amorphous metal film possesses the measured bulk metallic dielectric response. An XPS depth profile for a

ZrCuAlNi/AlPO laminate structure is represented in Figure A.3.6(a). The horizontal green and black lines, representing metal and oxide film thickness, respectively, are exactly the same length.

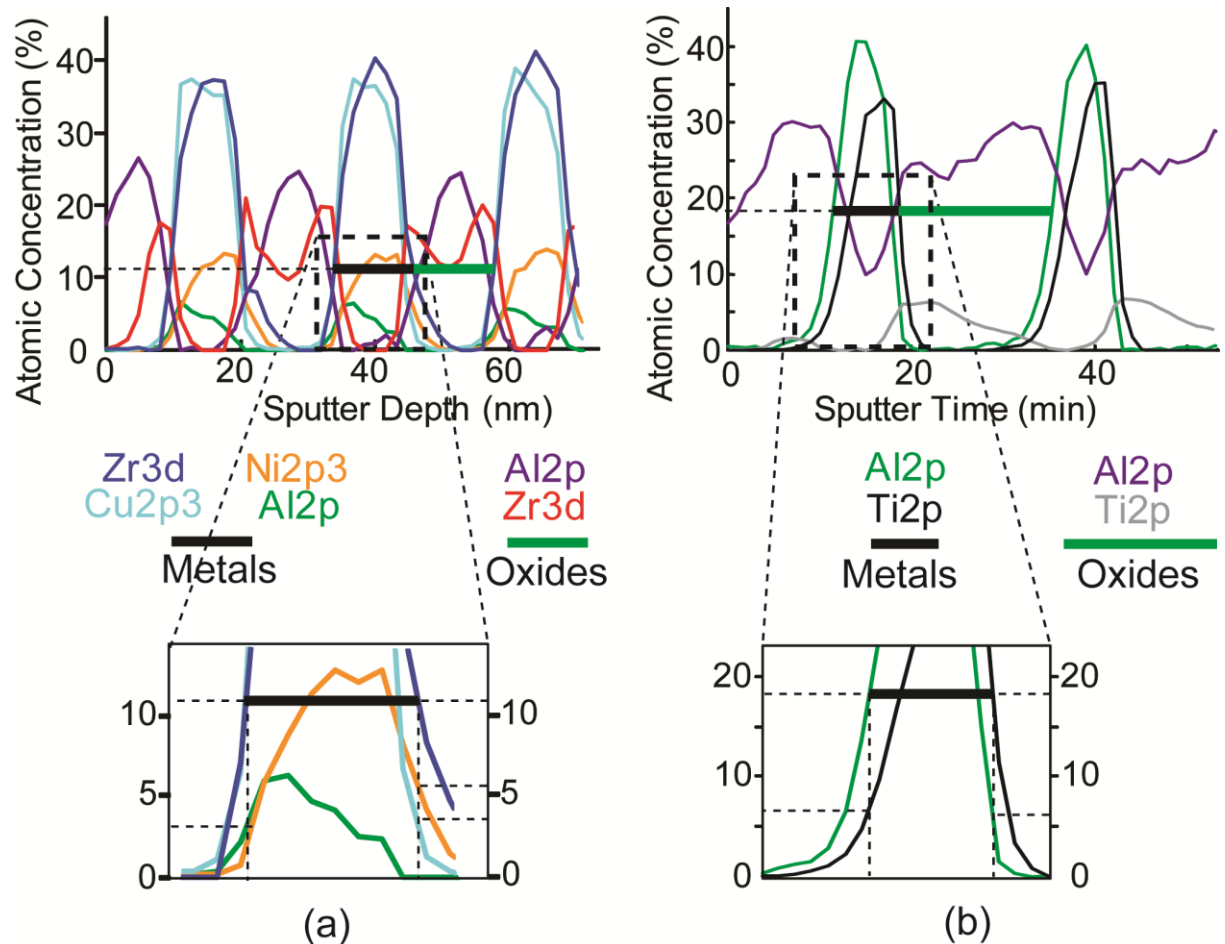


Figure A.3.6. XPS depth profiles taken through amorphous metal/oxide laminate structures. The solid green bars represent the thickness of metallic layers, while the solid black bars represent the thickness of oxide layers. The length of the bars have been scaled relative to each other to align with the metal/dielectric ratios that create the best model fit between measured and modeled reflectance data. The lower plots are magnified portions of the full plots (from dashed area), used to estimate un-oxidized metal content at modeled metal/dielectric ratios. (a) XPS data from a ZrCuAlNi/AlPO laminate structure, (b) XPS profile data from a  $\text{TiAl}_3$  laminate structure.

The normalized error zero crossing predicts a 1:1 thickness ratio of metal to dielectric. The total metal content is approximated by adding the atomic concentration of the four metal constituent XPS signals (Zr3d, Cu2p3, Al2p, and Ni2p3) at the interfacial location determined by the equivalently scaled horizontal lines. Using this methodology, the total metal content is estimated as 20% . The ZrCuAlNi film behaves as a metal when 20% of the elemental components remain unoxidized.

The initial analysis of XPS data collected from the ten bilayer  $\text{TiAl}_3/\text{AlPO}$  laminate revealed metal-to-oxide ratios that were not in alignment with the expected ratios based on deposition rate characterization. The amorphous metal depositions had targeted thicknesses of 8 nm, which would have produced 16 nm bilayers with equal proportions of metal and oxide similar to the ZrCuAlNi/AlPO laminate. The XPS analysis presented in Figure A.3.6(b) shows the unoxidized metal to be 31% of bilayer thickness instead of 50% . TEM analysis confirms that the XPS profiles provided an accurate metal/oxide thickness ratio in the laminate, as illustrated by the overlay of XPS and TEM data in Figure A.3.2(c). The observed reduction of un-oxidized metal thickness is consistent with observations across a variety of amorphous metal/oxide laminates. As discussed, oxidation of the amorphous metal occurs at interfaces on both sides of the amorphous metal layers. The interface created through the deposition of amorphous metal onto the AlPO layer contains oxides of  $\text{Ti}^{4+}$  and  $\text{Al}^{3+}$  created with the energy supplied from the sputter deposition. The interface on top of the amorphous metal layers contains a native oxide comprised of  $\text{Ti}^{4+}$  and  $\text{Al}^{3+}$  which is formed through the exposure of the

amorphous metal layers to air during sample transport from the sputter tool to the spin coater. The  $\text{TiAl}_3$  formed a thicker native oxide layer than the  $\text{ZrCuAlNi}$  native oxide, which reduced the metal/dielectric ratio of the laminate bilayers.

The ability to precisely measure a material's relevant characteristics is a requirement for a materials platform to be suitable for high volume manufacturing. Whereas the material analysis presented in Figure 2 is precise, the use of TEM imaging and XPS depth profiling is not an ideal metrology tool in high volume manufacturing due to the complexity of the analysis. Ellipsometry, however, has been widely employed in semiconductor manufacturing processes to evaluate dielectric thin film thicknesses throughout the semiconductor industry's untiring pursuit of Moore's Law.<sup>[17]</sup> An investigation into ellipsometry as a precise dispersion measurement technique for amorphous metal/oxide laminates shows that reflectance data easily evaluates anisotropic dispersion, and serves as the basis for effective medium theory based modeling. The characterization of thin-film amorphous metal/oxide laminates through ellipsometry, materials analysis, i.e., XPS and TEM, and effective medium modelling provides a robust picture of the predicted anisotropic optical dielectric response of amorphous metal/oxide laminates.

## **Conclusions**

In summary, we have demonstrated the ability to precisely control and measure the anisotropic dispersion characteristics of amorphous metal/oxide laminate materials.

Through the modulation of the individual layer bulk dielectric responses and thicknesses, we are able to predict the anisotropic dispersion responses with respect to incident light wavelength and angle through the use of effective medium modeling. The alignment between material analysis and ellipsometry measurements taken on fabricated laminate composites comprised of  $\text{TiAl}_3$  or  $\text{ZrCuAlNi}$  amorphous metal and amorphous  $\text{AlPO}$  dielectric bilayers confirm that scanning spectroscopic ellipsometry is a sensitive metrology tool able to monitor metal/dielectric ratio. Precise control of a laminate metal/dielectric ratio coupled with the differing dispersion responses of the two materials allows the resulting anisotropic dispersion to be engineered. The use of simple fabrication techniques, DC magnetron sputtering and aqueous solution deposition, illustrates the utility of amorphous metal/oxide laminates as a dispersion engineering platform that may be employed in large-area, low-temperature applications. Further development of the reported dispersion engineering platform will expedite the achievement of widespread anisotropic dispersion applications.

## **Experimental Section**

The amorphous metal thin films were deposited using three-inch vacuum-arc-melted multipcomponent metal targets purchased from Kamis Inc. with stoichiometric compositions of  $\text{Zr}_{40}\text{Cu}_{35}\text{Al}_{15}\text{Ni}_{10}$  and  $\text{Ti}_{25}\text{Al}_{75}$ . DC magnetron sputtering was employed at a power of 60 W, a pressure of 3 mTorr, and a 20 sccm flow of Ar gas. To

investigate the lower thickness limit of deposited amorphous metal films below 10 nm, the deposition power was lowered to 30 W with the remaining parameters held constant.

Aluminum oxide phosphate (AlPO) solution precursors for the amorphous oxide layers were prepared as previously described by Meyers et al. [18] to a 0.1 M concentration of aluminum with nitric acid as the strong acid. An aluminum to phosphate ratio of 5:3 was chosen for all films. The solution was spin-coated onto the AMMF at a speed of 3000 RPM for a duration of 30 s, followed by a treatment at 300 °C for 1 min on a hotplate under ambient atmospheric conditions. All samples were prepared on 1 inch x 1 inch coupons of thermally oxidized silicon prepared by Hewlett Packard's campus in Corvallis.

X-ray Photoelectron Spectroscopy (XPS) measurements were performed in a Physical Electronics Quanterra Scanning ESCA Microprobe with a focused monochromatic Al K $\alpha$  X-ray (1486.7 eV) source for excitation. The X-ray beam used was a 40 W, 200  $\mu$ m X-ray beam spot at the sample. The sputter depth profile data were acquired at grazing incidence with the samples at < 20° relative to the detector. The binding energy (BE) scale was calibrated using the Cu 2p<sub>3/2</sub> feature at 932.62  $\pm$  0.05 eV and Au 4f at 83.96  $\pm$  0.05 eV. The ion gun used in this system was a standard Quanterra ion gun, and the sputter depth profiles were acquired using a 1 KeV argon-ion beam rastered over a 3 mm x 3 mm area. To minimize charging artifacts, the XPS data were collected with 1 eV, 20  $\mu$ A electrons and low-energy Ar<sup>+</sup> ions. The XPS data were reduced using a linear least squares procedure to differentiate the oxidation states of the materials [19].

The atomic concentrations were calculated using relative sensitivity factors that were not corrected to reflect any preferential sputtering of the materials during the analysis.

The samples for TEM analysis were coated with carbon (vacuum evaporator, 30 sec) and iridium (sputtered, 2.5 min) as protective masks. Cross-section samples were then prepared using a standard focused ion beam (FIB) in situ lift out process in an FEI BualBeam 235 system. The FIB preparation involved patterning of a 1  $\mu\text{m}$  thick membrane using a 30 kV  $\text{Ga}^+$  ion beam after which the sample was transferred to a copper-grid using a micromanipulator inside the FIB system. Once attached to the copper grid, the membrane was further milled to an electron transparent thickness ( $< 100$  nm). The preparation was completed by milling both sides of the sample with a 5 kV  $\text{Ga}^+$  ion beam at a glancing angle of  $6^\circ$ . TEM and electron diffraction analysis was performed in a JEOL JEM2500SE analytical TEM/STEM employing a 200 kV accelerating voltage.

The artistic overlays onto TEM images were completed by utilizing raw image files from the JEOL JEM25500SE TEM. The scale bars from the raw image files were copied and separated from the original images into separate layers using Adobe Photoshop. Image cropping and rotation was then performed with the copied scale bar remaining unchanged. XPS data was then overlaid upon the images and relatively sized for effect. The data was intuitively overlaid to clearly demonstrate the congruency of the measurements taken. Added dimension bars were measured by calibrating pixel

dimensions using the copied original scale bar. Original images are attached as supplementary information.

Ellipsometry measurements were performed using a J.A. Woollam variable angle spectroscopic ellipsometer (VASE). Incident light was generated by a wide spectrum xenon light source, and polarized to  $T_E$  and  $T_M$  polarizations using a linear polarizer. Reflectance measurements of both  $T_E$  and  $T_M$  incident light were recorded at wavelengths between 300 nm and 1500 nm and incident angles between  $20^\circ$  and  $80^\circ$  at 5 degree increments. The dielectric responses of optically thick samples were calculated using a non-linear least squares fit of the reflectance data at each wavelength across the 13 unique angular measurements.

## References

- [1] J. Enoch, L. Vasudevan, *Ophthalmic and Physiological Optics*, **2000**, *20*, 126.
- [2] Willach, R. *The Long Route to the Invention of the Telescope*(American Philosophical Society, Philadelphia, **2008**).
- [3] V. Vesal'go, *Sov. Phys. Usp.*, **1968**, *10*, 509.
- [4] J. Pendry, *Phys. Rev. Lett.*, **2000**, *85*, 3966.
- [5] I. Lindell, S. Ilvonen, *J. of Electromagn. Waves and Appl.*, **2002**, *16*, 303.
- [6] V. Podolskiy, E. Narimanov, *Phys. Rev. B*, **2005**, *71*, 201101.
- [7] A. Hoffman, L. Alekseyev, S. Howard, K. Franz, D. Wasserman, V. Podoldkiy, E. Narimanov, D. Sivco, C. Gmachl, *Nature Mater.*, **2007**, *6*, 946.
- [8] M. Noginov, Y. Barnakov, G. Zhu, T. Tumkur, H. Li, E. Narimanov, *Appl. Phys. Lett.*, **2009**, *94*, 151105.
- [9] J. Elser, V. Podolskiy, I. Salakhutdinov, I. Avrutsky, *Appl. Phys. Lett.*, **2007**, *90*, 191109.
- [10] J. Valentine, S. Zhang, T. Zentgraf, E. Ulin-Avila, D. Genov, G. Bartal, X. Zhang, *Nature*, **2008**, *345*, 376.
- [11] S. Burgos, R. DeWaele, A. Polman, A. Atwater, *Nature Mater.*, **2010**, *9*, 407.
- [12] S. Xiao, U. Chettiar, A. Kildishev, V. Drachev, V. Shalaev, *Opt. Lett.*, **2009**, *19*, 3478.
- [13] G. Eleftheriades, K. Balmain, *Negative Refraction Metamaterials: Fundamental Principles and Applications* Ch.10 (John Wiley & Sons, Inc., Hoboken, **2005**).
- [14] E. W. Cowell, C. Knutson, D. A. Keszler, J. F. Wager, *ACS Appl. Mater. Interfaces*, **2**, 1811.
- [15] E. W. Cowell, N. Alimardani, C. Knutson, J. F. Conley, D. A. Keszler, B. Gibbons, J. F. Wager, *Adv. Mater.*, **2010**, *23*, 74.

- [16] J. Anderson, C. L. Munsee, C. M. Hung, T. M. Phung, G. S. Herman, D. C. Johnson, J. F. Wager, D. A. Keszler, *Adv. Func. Mat.*, **2007**, *17*, 2117.
- [17] G. Moore, *Electronics*, **1965**, *38*, 114.
- [18] S. T. Meyers, J. T. Anderson, D. Hong, C. M. Hung, J. F. Wager, D. A. Keszler, *Chem. Mater.*, **2007**, *19*, 4023.
- [19] W. F. Stickle, in *Surface Analysis by Auger and X-Ray Photoelectron Spectroscopy*, (Eds: D. Briggs and J. Grant), IM Publications, Chichester, West Sussex, UK, **2003** pp. 377-398

Appendix B.1.

TUNABLE DIELECTRIC THIN FILMS BY AQUEOUS, INORGANIC  
SOLUTION-BASED PROCESSING

Matti Alemayehu, John Evan Davis, Milton Jackson, Brian Lessig, Logan Smith, Jon  
David Sumega, Chris Knutson, Matt Beekman, David C. Johnson, and Douglas A.  
Keszler

Published in *Solid State Sciences*, **2011**.

## Introduction

In the wake of the semiconductor industry's transition to larger wafer sizes along with continued decrease in device size, the necessity for an alternate means of energy efficient and high-throughput deposition of high-performance dielectric materials has arisen. Dielectric materials that have controlled relative permittivity,  $k$ , are needed such that desired capacitance values can be realized in sub-micron-scale devices without issues of areal coverage tied to vacuum-chamber size. Characteristics that must be addressed include: thermodynamic stability, film morphology, interface quality, compatibility with current or projected materials to be used in processing metal-oxide-semiconductor devices, and reliability [1].

It has recently been demonstrated that issues of poor reliability, high cost of production, and chemical and material loss as waste may be attenuated by the incorporation of inorganic metal-based compounds in aqueous solution to produce high-performance dielectric materials *via* prompt inorganic condensation [2-4]. This approach provides a green alternative for the fabrication of gate dielectrics as they are readily deposited at room temperature under ambient conditions, are processed at relatively low temperatures, and avoid harsh solvents as well as expensive vacuum processing. Thin film layers can be spin coated onto substrates after minimal wafer preparation, producing smooth, uniform, and dense films with minimal waste. Moreover, film thickness can be manipulated by changing the metal concentration within the solution and by sequentially depositing multiple layers.

Promising interface characteristics of these amorphous metal oxide-based films prompted us to explore the possibility of synthesizing multilayer thin films with tunable dielectric properties. Two different systems, aluminum oxide phosphate  $\text{Al}_2\text{O}_{3-3x}(\text{PO}_4)_{2x}$  (AlPO) and hafnium oxide sulfate  $\text{HfO}_{2-x}(\text{SO}_4)_x$  (HafSO<sub>x</sub>), were chosen due to their exceptional individual dielectric characteristics and reported  $k$  values near 5 and 9-12, respectively [3,4]. By multi-coat deposition of the individual components by spin coating, two-component multi-layer thin films were prepared and characterized by X-ray reflectivity (XRR), scanning electron microscopy (SEM), and AC and DC electrical measurements. We have found that relative permittivity values between those previously reported for the two individual materials are obtained by simply adjusting the thickness ratio of the two distinct metal oxide-based components in dielectric thin films of approximately constant total film thickness.

## **2. Experimental**

### **2.1 Preparation of Solutions**

The composition and concentration of precursor solutions were chosen in order to produce a thickness per deposited layer of approximately 50 nm per coat for both material systems. An aluminum oxide phosphate (AlPO) precursor solution was synthesized by dissolving  $\text{Al}(\text{OH})_3$  powder (Alfa Aesar) in a solution of concentrated 68-70%  $\text{HNO}_3$  and 85%  $\text{H}_3\text{PO}_4$ . An Al:N:P = 5:10:3 molar ratio was utilized for this study because it resides well within the range cited to provide the desired amorphous-film characteristics *via* spin coating [3]. The resulting solution was then diluted to a

metal concentration of 0.60 M with 18.2 M $\Omega$ -cm H<sub>2</sub>O. The solution was stirred on a hot plate at 80-90°C for 24 hrs to completely dissolve the Al(OH)<sub>3</sub>. Complete dissolution of the Al(OH)<sub>3</sub> was confirmed by negligible scattering of visible HeNe laser light passed through the solution.

An aqueous hafnium oxide chloride solution with a total metal concentration of 1.00 M was produced by dissolving HfOCl<sub>2</sub> powder (Alfa Aesar) in 18.2 M $\Omega$ -cm H<sub>2</sub>O. Similarly, concentrated H<sub>2</sub>SO<sub>4</sub> was diluted to a 0.60 M concentration. 5-mL aliquots of the HfOCl<sub>2</sub> solution and of the sulfuric acid solutions were combined to give a metal concentration of 0.50 M and a Hf:S ratio of 5:3. Fresh solutions were prepared immediately prior to spin coating because of the observed propensity of this system to polymerize over the time period of a few hours.

## 2.2 Film Deposition

Six-inch Sumco, MOD-2 degenerately doped (n-type, resistivity less than 0.004  $\Omega$ -cm) <100> silicon wafers were cleaved into 2.54 cm  $\times$  2.54 cm coupons and then cleaned in a sonication bath of 5% Contrad-70 solution in 18.2 M $\Omega$ -cm H<sub>2</sub>O at 45°C for 30 min prior to coating. Solution precursors were deposited via spin coating, carried out at 3000 rpm for 30 s on a Laurell Technologies WS-400-6NPP-Lite spin coater. Multilayer films were fabricated by sequential layer deposition. All HafSO<sub>x</sub> layers were deposited first, followed by deposition of the appropriate number of AlPO layers. Each layer was cured on a hotplate at 450°C for 60 s prior to applying the next layer in order to prevent dissolution of the previously deposited layer; a final anneal was performed at

450°C in a Neytech QEX furnace for one hour with a 20°C min<sup>-1</sup> ramp rate. Each film contained a total of six layers, resulting in a total film thickness of nearly 300 nm.

### 2.3 Film Characterization

Films for XRR analysis were processed in parallel with devices to ensure thicknesses were consistent such that measured dielectric constants would be accurately measured. Films of AlPO and HafSO<sub>x</sub> processed from precursors with concentrations of 0.60 M and 0.50 M respectively were examined with XRR measurements to determine the relationship between thickness and number of layers deposited. XRR data were collected using a Bruker D8 Discover equipped with a Göbel mirror and modeled using the REFS Mercury simulation software (Bede Scientific Ltd.) in order to extract layer thicknesses [5]. Secondary electron SEM images of films and devices were taken using a ZEISS Ultra-55 Scanning Electron Microscope.

### 2.5 Device Fabrication and Electrical Characterization

Metal-insulator-insulator-metal (MIIM) devices were fabricated by layering HafSO<sub>x</sub> and ALPO onto a degenerate Si coupon as described above. Successive coats of ALPO were deposited atop layers of HafSO<sub>x</sub> such that the bottom electrode was consistently coated with HafSO<sub>x</sub> except in the case of the pure-AlPO dielectric. Layers of AlPO and HafSO<sub>x</sub> were applied with the previously specified curing step between applications of each layer. Circular aluminum (Alfa Aesar, 99.99%) top contacts (area of 1.0 mm<sup>2</sup>) were deposited by thermal evaporation in a Polaron thermal evaporation

apparatus and patterned via shadow-mask. Schematics of the fabrication process and general device structure are shown in Figure B.1.1. A back contact was achieved by scratching through the film and making electrical contact to the Si substrate with indium solder. Impedance was measured with an Agilent 4284A precision LCR meter at 10 kHz, 10 mV amplitude, and no DC bias.

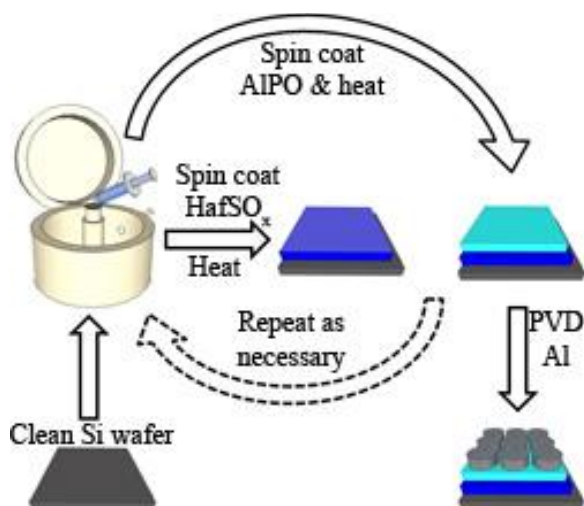


Figure B.1.1: Schematic process flow for production of capacitors via aqueous solution-processing.

## Results and Discussion

Single-layer and multilayer films were evaluated with XRR to determine the total thickness of the multilayer devices. This method allows for modeling of additive film thicknesses and also accounts for potential effects of interdiffusion and minor interfacial redissolution from successive layer depositions. Due to the complexity of the XRR patterns produced by the multilayer specimens, the data were analyzed with the aid of computer modeling.

To ascertain the relationship between the number of layers deposited and the total film thickness, single component films with varying number of layers were

deposited and characterized by specular XRR. XRR is sensitive to spatial variations in electron density along the out-of-plane direction that are present in the dielectric film. The data were modeled as a stack of layers in which the X-ray indices of refraction, surface roughness, and thicknesses for the individual layers were used as adjustable parameters to produce the best fit to the data. Consequently, the total film thickness can be extracted. The presence of an interfacial region between the layers was modeled as a thin layer (less than 1 nm in thickness) of slightly higher X-ray index of refraction. This produces Bragg-like diffraction that was observed in the experimental data. As an example, Figure B.1.2a shows experimental and simulated XRR data for a four-layer HafSO<sub>x</sub> film; good agreement between the experimental and simulated data is achieved. As indicated in the inset to Figure B.1.2a, a linear relationship between the total film thickness and the number of layers deposited was observed, indicating a thickness of  $44 \pm 5$  nm per deposited layer.

In the case of the single component multilayer AlPO films, film thickness determination from XRR data was unsuccessful, primarily due to the relatively small difference between the indices of refraction of the AlPO film and the underlying native SiO<sub>2</sub> layer, resulting in relatively weak Kiessig fringes. Attempts to model the XRR data for the multi-component (HafSO<sub>x</sub> + AlPO) films in order to simultaneously determine the individual layer and total film thicknesses were also unsuccessful. Slight differences in the nature of the interfaces between the layers and/or slightly non-uniform indices of refraction can result in XRR patterns of significant complexity.

However, the thickness of the AlPO component in the stacks could be straightforwardly determined in the case of the two component films.

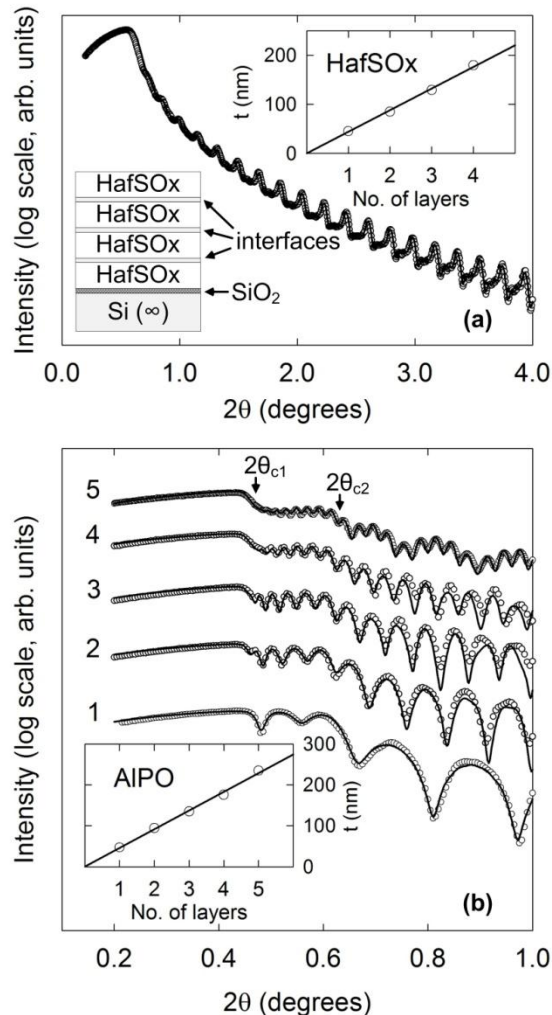


Figure B.1.11: (a) Experimental XRR data collected on a HafSOx film containing four layers (coats). The solid line is a simulated fit to the data, using the model shown schematically in the lower left inset. Upper right inset: Total film thickness,  $t$ , vs. the number of layers deposited for single component HafSOx films. Lower right inset: Schematic of the model used to fit the XRR data. (b) Experimental XRR data ( $\circ$ , intensity offset for clarity) collected from two component AlPO-HafSOx films; the number of AlPO layers in each film is indicated to the left of each data set. The solid lines are simulated fits to the data, using a “two-layer” model of AlPO-HafSOx-SiO<sub>2</sub>-Si.  $2\theta_{c1}$  and  $2\theta_{c2}$  indicate the critical angles corresponding to the air-AlPO and AlPO-HafSOx interfaces, respectively. Inset: AlPO component thickness,  $t$ , vs. the number of AlPO layers deposited.

Since the AlPO component is significantly less optically dense than HafSO<sub>x</sub>, two critical angles for total reflection are observed in the XRR patterns,  $\theta_{c1}$  and  $\theta_{c2}$ , corresponding to the air-AlPO and AlPO-HafSO<sub>x</sub> interfaces, respectively. In the angular range between  $2\theta_{c1}$  and  $2\theta_{c2}$ , the observed interference fringes (Figure B.1.2b) arise solely from the thickness of the AlPO layer, since in this angular range the X-ray beam is completely reflected at the AlPO-HafSO<sub>x</sub> interface. In this case the XRR data were fit to a model representing a single uniform AlPO layer on top of a single uniform HafSO<sub>x</sub> layer, where the AlPO layer thickness was adjusted to best fit the data in the angular region  $2\theta_{c1} < 2\theta < 2\theta_{c2}$ . As shown in the inset to Figure B.1.2b, a linear relationship between the AlPO component thickness and the number of deposited layers was observed, indicating a thickness of  $46 \pm 6$  nm per deposited layer.

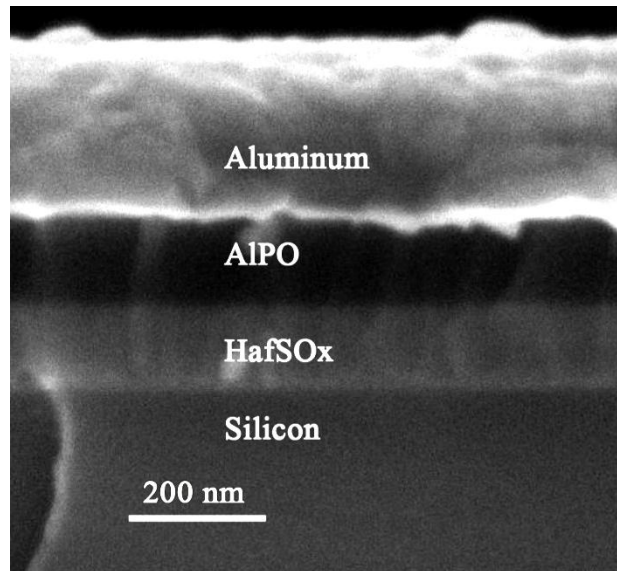


Figure B.1.3: Cross-sectional SEM images of AlPO/HafSO<sub>x</sub> thin film device.

Cross-sectional SEM imaging (Figure B.1.3) of a MIIM structure containing three AlPO layers and three HafSO<sub>x</sub> layers confirmed that the layers exhibit smooth morphology. Due to the significant difference in electron density, the individual AlPO and HafSO<sub>x</sub> components are clearly discernable, confirming the multilayer structure remains post-thermal processing. Although minor tilt was used in order to improve the quality of the acquired SEM images, the resulting thickness measurements are in agreement with those obtained from the XRR data.

MIIM capacitors with various HafSO<sub>x</sub>:AlPO thickness ratios were fabricated, as discussed above, by varying the number of coats of each component material. This approach allowed rapid fabrication and testing of devices with seven HafSO<sub>x</sub> to AlPO thickness ratios to determine how the effective dielectric constant changed as a function of stack sequence. The capacitors were tested for their relative dielectric constant,  $k$ , and loss tangent,  $\tan\delta$ . A minimum of five MIIM capacitors in each coupon were tested to give a mean and standard deviation.

Initial testing of a blank wafer with ohmic contacts confirmed negligible capacitive contributions to the measurement due to the substrate, native oxide layer, and electrical contacts. The thickness characterization can in principle be obtained very accurately from XRR for simple structures. However, as discussed above, XRR measurements of the six-layer devices are not readily interpreted, therefore the simplest stacking sequences were used in order to generate the thicknesses of components and discern the effects of multiple coats on thickness. The largest source of uncertainty in our measurement originates in the determination of the component-layer and total-film

thicknesses, and was statistically propagated through the calculations from the linear fits to the data shown in insets in Figure B.1.2a and b.

The effective relative dielectric constant,  $k$ , for each multi-layer film was calculated from the measured device capacitance,  $C$ , as  $k = Ct_{\text{total}}/\epsilon_0A$ , where  $A$  is the active device area,  $t_{\text{total}}$  is the total film thickness, i.e.  $t_{\text{total}} = t_{\text{HafSOx}} + t_{\text{AlPO}}$ , and  $\epsilon_0$  is the permittivity of free space. These data are plotted in Figure B.1.4 as a function of the HafSOx thickness fraction,  $t_{\text{HafSOx}}/t_{\text{total}}$ . Relative dielectric constants ranging between  $4.6 \pm 0.3$  for pure AlPO and  $9.5 \pm 0.3$  for pure HafSOx were obtained. The values obtained for the single-component films are in very good agreement with those previously reported [3, 4]. Measured  $\tan\delta$  values for all devices did not exceed 2%, while measured breakdown voltages and leakage current densities were also in good agreement with those previously reported for the individual components [3, 4].

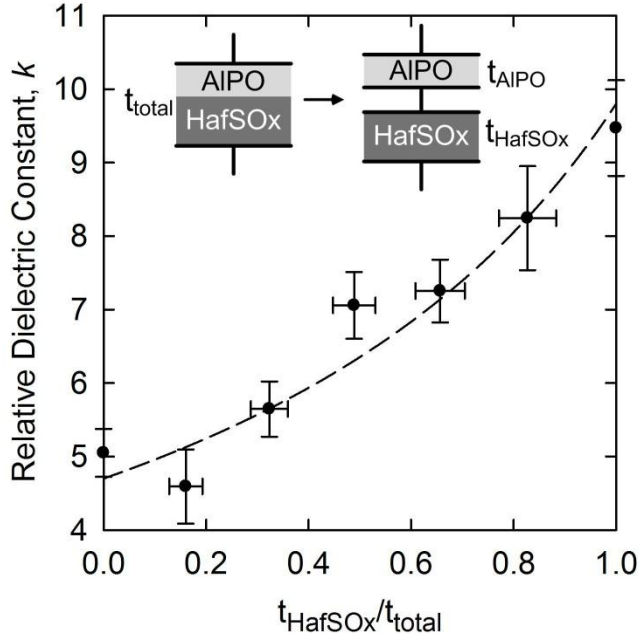


Figure B.1.4: Relative dielectric constant,  $k$ , as a function of the HafSOx thickness fraction. Error bars represent  $\pm 2\sigma$  uncertainty in the calculated values. The dashed line is a calculation based on the simple two-dielectric capacitor model (inset) discussed in the text.

The simplest model that may be used to describe our devices comprises a parallel plate capacitor partially filled with a uniform AlPO dielectric of thickness  $t_{\text{AlPO}}$  and partially filled with a uniform HafSOx dielectric of thickness  $t_{\text{HafSOx}}$ . In this case, the total capacitance,  $C$ , can be equivalently represented by two capacitors electrically in series, so that

$$\frac{1}{C} = \frac{1}{C_{\text{AlPO}}} + \frac{1}{C_{\text{HafSOx}}}, \quad (1)$$

where  $C_{\text{AlPO}} = Ak_{\text{AlPO}}\epsilon_0/t_{\text{AlPO}}$  and  $C_{\text{HafSOx}} = Ak_{\text{HafSOx}}\epsilon_0/t_{\text{HafSOx}}$ . The effective dielectric constant predicted from this model is therefore given by

$$\frac{1}{k} = \frac{t_{\text{AlPO}}}{t_{\text{total}}} \frac{1}{k_{\text{AlPO}}} + \frac{t_{\text{HafSO}_x}}{t_{\text{total}}} \frac{1}{k_{\text{HafSO}_x}}. \quad (2)$$

We fit our data (dashed line in Fig. 4) to this model, with resulting fitted values of  $k_{\text{AlPO}} = 4.7$  and  $k_{\text{HafSO}_x} = 9.8$ , again in good agreement with the previously published values [3, 4]. In spite of its simplicity, this model describes the observed trend in the data relatively well. The observed deviations may be due to interfacial and/or other effects not captured by the simple model of only two homogeneous dielectric materials. For example, the number of each individual interface type, e.g. AlPO-AlPO, AlPO-HafSO<sub>x</sub>, or HafSO<sub>x</sub>-HafSO<sub>x</sub>, was not held constant in the devices studied. Such aspects are of interest for future investigation of the detailed dielectric behavior of these solution deposited inorganic nanolaminated, multilayer films.

## Conclusions

We have reported a simple and novel method for creating tunable dielectric thin films by prompt inorganic condensation from aqueous solution. The film thickness can be predictably controlled by varying the molarity of the AlPO and HafSO<sub>x</sub> solutions, as well as repeated sequential deposition by spin coating. The potential utility of these materials includes ease of manufacture without the need for sophisticated vacuum deposition equipment. Significantly, we demonstrate that any relative dielectric constant between 5 and 10 can be selected as needed for the application. Films of desired

thickness can in principle be specifically made for a range of applications. We expect the approach can be applied generally to other materials systems, providing a simple and inexpensive fabrication route for devices that require insulating layers with specific dielectric properties.

## References

- [1] G. D. Wilk, R. M. Wallace, and J. M. Anthony, *J. Appl. Phys.* 89 (2001) 5243.
- [2] D. A. Keszler, J. T. Anderson, S. T. Meyers, *Oxide dielectric films for active electronics in Solution Processing of Inorganic Materials*, ed. D. Mitzi, pp. 109-129 (2009).
- [3] S. T. Meyers, J. T. Anderson, D. Hong, C. M. Hung, J. F. Wager, and D. A. Keszler, *Chem. Mater.* 19 (2007) 4023.
- [4] J. T. Anderson, C. L. Munsee, C. M. Hung, T. M. Phung, G. S. Herman, D. C. Johnson, J. F. Wager, and D. A. Keszler, *Adv. Funct. Mater.* 17 (2007) 2117.
- [5] M. Wormington, C. Panaccione, K. Matney, and D. Bowen, *Philos. Trans. R. Soc. London A* 357 (1999) 2827-2848.

## Appendix B.2

### **A STATE-OF-THE-ART, LABORATORY-INTENSIVE, GUIDED-INQUIRY- BASED GRADUATE RESEARCH COURSE**

Chris Knutson, Matt Beekman, David C. Johnson, and Douglas A. Keszler

This is prepared for submission to the *Journal of Chemical Education*.

## Introduction

The primary thrust of the research institution is to prepare students to do research as both professors and members of industry.<sup>1</sup> It is important to recognize this fact; and it is also of utmost consequence to acknowledge that the types of preparation for research offered to students need to evolve with students as they progress in their educations. While cookie-cutter, expository labs are common in most entry-level chemistry courses, the pre-set labs do not offer much in terms of the higher-order cognitive training required for graduate-level research.<sup>2</sup>

Many institutions offer guided-inquiry classes to their upperclassmen, and some institutions have started adopting this for freshman classes with varied issues associated with the method.<sup>3,3-5</sup> Sadly, many of the guided-inquiry-based classes do not tackle cutting-edge research as the classes require definite outcomes in order to be graded evenly across large numbers of students. The standard guided-inquiry classes only begin to scratch the surface of the research experience because they only require students to independently develop means of carrying out a historically accomplished task.<sup>6</sup>

By adjusting the focus of guided inquiry to students who have already completed a degree, many of the problems historically associated with guided inquiry in a laboratory setting may be avoided.<sup>3,7</sup> Students enter the class with a predetermined skill set and knowledge of the subject allowing them to formulate more complete questions and actively search for answers. Basic laboratory techniques and scientific literacy are already present and can be called upon for assignments. It can be argued that students at

the post-baccalaureate level are in the perfect phase of education for guided-inquiry-based classes.

Guided-inquiry has historically been the basis for the majority of graduate education, specifically in doctoral programs. Professors act as advisors and facilitate the research of their students who in turn must actively inquire about common practices in the field and develop new means of solving new problems. As the graduate students progress through their degrees, produce theses and approach doctoral or even postdoctoral levels they must make another drastic transition.

The final transition into industry or academia often lacks any guidance or formal training. There is very little support for the graduate student becoming a professor, researcher or project manager. In most cases it is simply assumed that the PhD will quickly transition between the role of research assistant to researcher or professor due to the already-proven intelligence. While there are many organizations forming to provide support in this transition, there are few instructional opportunities covering how to handle this transition for students at this point in their careers.

Multiple recent studies have shown that graduates are more employable, successful in their respective programs and ultimately capable of teaching when given the opportunity to teach as well as training and mentorship in teaching.<sup>8-12</sup> Peer-level instruction has also been shown to be useful in the presentation of chemical-laboratory information<sup>7</sup>, so the opportunity to pair graduates at disparate levels in a learning environment has the opportunity to be a very successful medium for instruction and learning.

We have designed a class in an attempt to tackle two major transitional periods in scientific education by associating post-baccalaureate students with doctoral students reaching the end of their programs. By associating the two groups and choosing pertinent topics of study, much of the research culture of our given institution was transferred to the incoming graduate students while the doctoral students learned about running a research laboratory. Many of the issues involved with graduate teaching of guided-inquiry classes<sup>5</sup> were avoided by utilizing the expertise of the doctoral student through deliberate laboratory project choices.

The course was designed as part of the NSF phase-1 Center for Green Materials Chemistry (CGMC), therefore projects in inorganic solution processing were chosen for the students. This was a perfect fit for the modernization and greening of curriculum as proposed by the NSF.<sup>13,14</sup> Post-baccalaureate students were offered the class as an extension of a conventional semiconductor-processing curriculum and as an extension of a polymer-chemistry curriculum. These seemingly diverse preparations are both utilized in the field of inorganic solution processing of thin-film device components specific to the CGMC.<sup>15-18</sup> The course was offered in CAMCOR, the Center for the Advancement of Materials Characterization of Oregon, a shared, open-user facility. CAMCOR contains extensive characterization equipment that was available for the course, and remains available for the students after they have graduated from their respective programs.

The teachers of the class were chosen such that they were at the end of their doctoral and post-doctoral educations and interested in doing academic research instruction. The teachers were tasked with establishing a curriculum, a syllabus, tests, evaluation criteria and a grading rubric for the class. Teachers were also tasked with leading class discussion, budgeting equipment, ordering supplies and acquiring classroom facilities. These tasks were chosen to acclimate the future collegiate educators to their future duties in an environment with strong mentoring from their advisors. Attention to these factors has been shown to be an effective means of preparing graduates for successful teaching and research<sup>8-11</sup>, making this an opportunity for professional growth and increased employability.

The class's primary project was designed by a graduate student and a post-doctoral research associate working for the center such that it would fit three major criteria. First, the class would have to do new research pertinent to the CGMC. Incorporating research as a model for education is an excellent method of defining problems and methods of seeking solutions for incoming students.<sup>19</sup> This method offers the dual incentive of learning how to deal with research problems and offers on-the-job training for a grade. The skills gleaned from these exercises carry real world weight to the student and utilize higher cognitive development which increases retention of the information presented.

Secondly, the class was designed to address major criteria of graduate education in materials science within the course framework. Recent work by Ellis et. al. shows this method to be a promising method to increase both interest in and retention of materials presented in coursework.<sup>6</sup> Training of students on necessary instrumentation for future

research was incentivized scholastically and made into a peer-based activity with clear review of performance and understanding. This method removed the responsibility for training from other members of the graduate students' respective research groups and offered the student the ability to report information taken from pertinent instrumentation with confidence, even as amateur researchers.

Third, the class offered the students a rare opportunity for both a grade and a publication-quality report on nanolaminated dielectrics. This method allows for comprehensive coverage of the responsibilities of a researcher to the amateurs which has shown to be a useful method of successful education.<sup>6</sup> While the third criterion is a lofty goal, it is common pedagogical knowledge that setting high goals is a common predecessor for success in a student population. The course was also designed such that further objectives of the NSF were addressed.

### **Course Objectives for Post-Baccalaureate Students**

There are many important skills associated with successful research, and many quirks that are specific to scientific research in particular that are not common in other fields. The class addressed eight major objectives associated with the success of researchers at the graduate level. The objectives of the class were to:

1. Introduce the students to group research dynamics by imitating a research-group format.
2. Introduce the students to new technology through guided reading assignments.

3. Use guided inquiry to establish standardized, best-practice laboratory standard operating procedures in small groups.
4. Expose students to diverse characterization techniques, allowing them to train-in on the equipment, and having students address issues of operating experiments in shared facilities.
5. Create a technology-transfer situation between small groups of students reminiscent of transferring technology from a research lab to a company.
6. Utilize peer review in grading of presentations and formulation of manuscripts.
7. Fabricate structures that illustrate a comprehensive use of the technology in a test-product format.
8. Write a manuscript-style article about the research carried out in the class.

Further discussion of the methods involved in the inclusion of each specific objective will now be addressed.

### **Introducing students to group research dynamics**

The research group is an integral part of the graduate-level research experience that is rarely addressed in undergraduate laboratory courses. Traditional laboratory classes tend to pair students for individual experiments and characterizations that take little more than hours to carry out<sup>2</sup>; while graduate research often generates projects shared between students for weeks, months and even years. Productive insights, project standardization and ultimately success of projects are often contingent upon open communication within research groups.

This class utilized the group meeting format both because it is the prevalent format of cooperative communication in graduate study, and because the students came from different backgrounds which offered mutually-beneficial insights. By starting each class period with a group presentation, best practices were standardized via thoughtful inquisition of the presenter and ultimately the group. Individual and group learning were utilized and the class organizers were given opportunity to use guiding inquisition to direct experimentation as is common within the true research format.

**Introducing the students to new technology through guided reading assignments.**

This class had no formal text, as true research typically has no formal text. Samples of literature<sup>15-18</sup> were provided to the students as a starting point for investigation. Quizzes were also prepared based upon the initial literature offered. This literature allowed the students to standardize experiments to previously published results and offered procedural starting points. The literature also gave examples of pertinent characterization techniques as well as representation of data in publication-quality figures. Students were able to utilize the Meyers et al. and Anderson et al. papers to formulate solutions, the Jiang et al. paper as a proof of concept of solution-processed nanolamination and the Munsee thesis as a basis for electrical characterization. Further inquiry-based literature searching about the state-of-the-art in other deposition methods was encouraged for the final report of the class with the purpose being two-fold:

First, students would realize the differences between the CGMC's core technologies and those of prevalent industry and research. Secondly, students would be able to develop a comprehensive introduction to their final written report for the class in which they could compare and contrast common thin-film processing technologies in rigor and cost.

These exercises allowed the students to frame their research in reference to state-of-the-art methods in the community as well as build their understanding of the subject matter and place themselves firmly into the technological community under investigation.

**Using guided inquiry to establish standardized, best-practice laboratory standard operating procedures in small groups.**

With some literature background, students could then formulate hypotheses, procedures and practices. There were many issues in which standardization was necessary for group success including but not limited to: solution formulations, wafer preparation, spin-coater settings, dielectric-testing frequencies, device sizes and characterization techniques. The group was allowed to decide how to use a limited budget to plan instrument usage as well as produce art for a paper. The course instructors were encouraged to offer some guidance about budgetary and time-based concerns if the students were not addressing those limitations much like in real research situations.

Guided inquiry also generated a streamlined equipment scheduling and training regimen amongst the students. When given the problem of deciding on training and organizing training, the students quickly went about defining roles for themselves and

taking on responsibilities for those roles. Instrumentation utilization was facilitated by students readily asking each other about previous training from preceding courses and then organizing themselves accordingly. Small group work allowed for concurrent scheduling via guidance of the inquiry into training and device scheduling at the CAMCOR facility.

**Exposing students to diverse characterization techniques, allowing them to train-in on the equipment, and having students address issues of operating experiments in shared facilities.**

The CAMCOR facility has: scanning electron microscopes, focused-ion beam milling, transmission electron microscopes, atomic-force microscopes, X-ray reflectivity and diffraction tools as well as capable electronic probe stations that were all available to the class. The students in the class were required to have training in order to access and use the various tools available to them. The facility operates such that one must get training in order to access instrumental calendars, or one must schedule with the facility's technicians in order to carry out characterizations on one's materials.

Each student in the class was required to formulate a Power-Point presentation about one of the characterization techniques available at the CAMCOR facility. The presentations included the fundamentals of the measurement, the cost of the measurement and the sample preparation used in order to obtain the best measurement for the project. The presentations were peer reviewed as will be discussed in a later section of this contribution. The questions that were used to guide the peer review were

formulated based upon past-research experiences that the teachers of the course have had with testing facilities. Grades were assessed upon the class's reactions to these questions.

Students had to schedule instrument time for the preceding-listed characterizations within the budget of the class which was set at one thousand dollars. The students naturally used the group meeting to streamline testing, organize their calendars around other users of the facility and discuss parallel processing of samples for the characterizations to minimize budgetary impacts and maximize effectiveness.

**Creating a technology-transfer situation between small groups of students reminiscent of transferring technology from a research lab to a company.**

Technology transfer between research groups and industrial partners or investors is the preeminent issue of turning successful research into marketable technology. Programs have been developed by NSF initiatives to train students on how to do this effectively<sup>20</sup>, yet these programs do not gainfully compel students to effectively transfer laboratory technologies amongst each other. The class offers incentive in the form of accredited grades and the opportunity to publish dependent on peer review. It is very difficult to effectively imprint the issues inherent in technology transfers upon students without actual hands-on laboratory examples and compelling study of specific problems.

Students in the class were required to do a technology transfer exercise based upon solution processing. The exercise involved a standardization of thickness versus concentration profiles for two different solution-processed dielectrics. The class was

split into two groups. Each group was given a system to study. Each group had to generate a thickness vs. concentration profile for its respective system with each person generating a point for the plot with error bars. When each group had delivered its curve to the instructor, it was the job of each group to teach the other group to process the alternate film in such a way as to reproduce the thickness vs. concentration plot within the standard deviation of the first.

The exercise gave the students first-hand knowledge about the issues that arise with technology transfer and the possible subjectivity of standardization. Anecdotal evidence indicates that students did not actually understand the gravity of this task upon reading the syllabus, however found the task to be the most difficult assignment in the course. This first-hand experience had a profound effect on the class's communication skills with regards to technology transfer and generation of standard operating procedures.

### **Utilizing peer review in grading and formulation of manuscripts.**

As previously discussed, the class relied heavily upon peer review. In a well-functioning research group there should be discourse. Properly managed discourse among graduate-level students is a driving force for great research. As a research institution, we want to produce skilled skeptics who are capable of defending good ideas with logic, and evaluating the scientific ideas of others fairly.

There was a class project in which each student in the class gave a ten-minute presentation about a characterization technique present in CAMCOR, as previously mentioned. Each member of the class was graded by the rest of the class as well as the teachers. Criteria for grading included:

1. Were the principles of the measurement clearly defined?
2. Was the applicability of the technique to the project demonstrated clearly?
3. Would you be likely to commission this person to have these tests done on your samples?

Students were encouraged to ask questions until they felt comfortable that the listed criteria were addressed. Only one student ultimately refused to take part in the exercise by assigning full scores to the rest of the class. The student was later questioned about it and did not see the practice as abnormal. Further peer review by the same student reflected the same pattern. The other five members of the class consistently ranked each other within the same ranges as the teachers ranked them.

Students were also encouraged to evaluate the artistic representation of the data in a pass-around format. Students were encouraged to generate a method of internet file-sharing to produce a manuscript. The syllabus planned for literature reviews to progress into discussions of how to write each section by the end of the second week of coursework. The group was encouraged to work cohesively to generate and edit data. The class organized its own common database and regularly self-reviewed. Five of the six students actively participated in the review of the data and the production of the manuscript while the final student minimally participated.

Finally, participation grades were assessed via peer review. Each member of the class got to assign numerically scaled grades to all other members of the class pertaining to five criteria. Criteria for participation grades included:

Did the individual provide regular and pertinent input during group discussions?

Did the individual listen and consider the ideas of others during decision making?

Did the individual exhibit professionalism and respect for his/her colleagues?

Did the individual contribute significantly to the overall success of the group?

Would you seek out this individual for future collaboration?

We believed that these questions were important reflections of research interests; however, other questions may be used in future iterations of the class to promote positive future behaviors in research. The most important anecdotal findings from this exercise were that this peer review consistently reflected the disdain for the minimally-participating student with even the student who assigned full credit to all on presentations docking the minimally-participating student points on reliability-related criteria. Nobody expressed interest in collaboration with the minimally-participating student for future work.

**Fabricate structures that illustrate a comprehensive use of the technology in a test-product format.**

The class centered on making thin-film capacitors by utilizing solution-processed dielectrics generated by the CGMC. Students were guided to produce dielectric films on highly-doped silicon, characterize the films and finally use thermal evaporation to deposit aluminum top electrodes. The final stage of the class was comprised of testing the devices. Students were encouraged to share experience from their previous classes in the fabrication and characterization of the devices.

The device format forced students to study surface-preparation methods, film-characterization techniques and technological material integration into devices. The format allowed students to study a new technology from birth to application; offering not only a chemistry experience but also a familiarity with the engineering of useful devices with the technology. Most chemistry-class experiences are limited to material preparation and characterization, but not device engineering. By utilizing an engineering step, students got to branch away from chemistry into an engineering environment and utilize skills not usually tapped in chemistry laboratories.

Students expressed great interest and fulfillment from having worked with a system from chemical concepts through final application and testing. Having a final application for the chemistry acted as a motivation for the students, and having both devices and initial characterizations allowed students to observe exactly why the material characteristics that they were attempting to foster were important in final applications. We believe that this method is very similar to the methods employed by

Dr. Patricia Hill who uses artwork as her final product to inspire non-chemistry students to learn the chemistry inherent to art with great success.<sup>21</sup> Utilizing this method builds interest in the engineering-interested students by displaying utility in their field while simultaneously displaying the utility of chemistry in the field of electrical engineering.

Future iterations of the class could utilize the same processes to create dielectric mirrors<sup>7</sup>. The technology is not limited to electronics but may be used to interest physics students who study optics and sonic media. The CGMC solution-processing template has the ability to tailor projects to the physics and optics communities as well. The thrust of the class can be drastically changed by utilizing the same laboratory equipment and a variety of easily-employed, minor alterations to course literature and syllabi.

### **Writing a manuscript-style article about the research carried out in the class.**

The students were compelled to write a manuscript-style article about the findings of the class. Surprisingly, the students were able to accomplish this lofty goal in the three-week time period. Online document sharing was set up by the students and active production and review were undertaken immediately by all but one member of the class. The manuscript was written, reviewed by the majority of the class and finally submitted to the instructors. Instructors were then tasked with peer-reviewing the article and pass it back to the students. With minor grammatical and graphical adjustment, the article was submitted to the journal Solid State Sciences and published.<sup>22</sup>

## **Conclusions**

Course reviews indicated that a majority of the students enjoyed the guided-inquiry-based experience at this level of education and directly equated the experience to an internship-type experience for research. Students recognized the utility and philosophy of the research in both assessment and their own reviews of the class. They performed well with technology transfer exercises, process integration assessments and writing. The shortened time period of the class was difficult for both the instructors and the students, however, there were few complaints in the course reviews. The class effectively introduced students to open-user production and characterization facilities. Students had a fruitful exercise in discovery that has carried over to successful internships for four of the students and also proven useful to two students who went directly to work in chemical fields.

The instructors of the class gained valuable experience teaching at the graduate-level and managing a small research group with a designated goal. Instructors also gained career experience in generating curriculum, quizzes, tests, readings and grades that has proven useful in their respective career paths. The instructors have validation of ability in teaching and doing cutting edge research with a small group of graduate students with varied backgrounds. All of these aspects of the class have proven helpful to each of the instructors in the process of seeking post-doctoral employment in academic roles with one of the instructors accepting a professorial position at a 4-year undergraduate institute and another accepting the position of lecturer at a university. Specific instances from the class were able to be referenced during interviews for these

positions, allowing the instructors to prove themselves knowledgeable about teaching endeavors.

The success of the guided-inquiry technique was directly related to the abilities and expertise within the subject matter of the students and instructors. Technology transfer was successfully carried out between groups of students, and also between instructors and students. This class was a successful introduction to the realities of employment both in the private sector for the post-baccalaureate students as well as an introduction to academic employment for the cerca-doctoral student instructors.

We believe that similar programs can and should be implemented at the graduate level across disciplines. The underlying problems that the course addressed, those of training capable faculty and graduate students, as well as the methods have wonderful potential to revolutionize graduate education in the United States as well as the world. By utilizing active apprenticeship models and learning through doing exercises for both disparate levels, both groups of people involved learned valuable lessons about research, group dynamics and leadership that will carry through to their chosen careers.

## References

- (1) Gonzalez, C. *Science* **2001**, *293*, 1624-1626.
- (2) Domin, D. S. *Journal of Chemical Education* **1999**, *76*, 543.
- (3) Kurdziel, J. P.; Turner, J. A.; Luft, J. A.; Roehrig, G. H. *Journal of chemical education* **2003**, *80*, 1206.
- (4) Furtak, E. M. *Sci. Ed.* **2006**, *90*, 453-467.
- (5) Kirschner, P. A.; Sweller, J.; Clark, R. E. *Educational psychologist* **2006**, *41*, 75-86.
- (6) Ellis, A. B.; Widstrand, C. G.; Nordell, K. J. *Journal of Chemical Education* **2001**, *78*, 1044.
- (7) Tien, L. T.; Roth, V.; Kampmeier, J. A. *J. Res. Sci. Teach.* **2002**, *39*, 606-632.
- (8) Stewart, K. K.; Lagowski, J. J. *Journal of Chemical Education* **2003**, *80*, 1362.
- (9) Lees, D.; Learning; Centre, T. S. N. G. *Graduate employability-literature review*; LTSN Generic Centre, 2002.
- (10) Boyle, P.; Boice, B. *Innovative Higher Education* **1998**, *22*, 157-179.
- (11) Prieto, L. R.; Altmaier, E. M. *Research in Higher Education* **1994**, *35*, 481-497.
- (12) Herrington, D. G.; Nakhleh, M. B. *Journal of chemical education* **2003**, *80*, 1197.
- (13) Ware, S. A. *Pure and applied chemistry* **2001**, *73*, 1247-1250.
- (14) Collins, T. J. *Journal of chemical education* **1995**, *72*, 965.
- (15) Munsee, C. Characterization of solution-based inorganic semiconductor and dielectric materials for inkjet printed electronics. EECS, Oregon State University: Corvallis, OR, 2005.
- (16) Jiang, K.; Zakutayev, A.; Stowers, J.; Anderson, M. D.; Tate, J.; McIntyre, D. H.; Johnson, D. C.; Keszler, D. A. *Solid State Sciences* **2009**, *11*, 1692-1699.
- (17) Meyers, S. T.; Anderson, J. T.; Hong, D.; Hung, C. M.; Wager, J. F.; Keszler, D. A. *Chem. Mater.* **2007**, *19*, 4023-4029.

- (18) Anderson, J. T.; Munsee, C. L.; Hung, C. M.; Phung, T. M.; Herman, G. S.; Johnson, D. C.; Wager, J. F.; Keszler, D. A. *Adv. Funct. Mater.* **2007**, *17*, 2117-2124.
- (19) Desai, K. V.; Gatson, S. N.; Stiles, T. W.; Stewart, R. H.; Laine, G. A.; Quick, C. M. *Advances in physiology education* **2008**, *32*, 136.
- (20) CCI Research to Innovation Workshop (R2I) Home  
<http://www.invention2venture.org/r2i/> (accessed Jul 6, 2011).
- (21) Millersville University - Chemistry in Art.
- (22) Alemayehu, M.; Davis, J. E.; Jackson, M.; Lessig, B.; Smith, L.; Sumega, J. D.; Knutson, C.; Beekman, M.; Johnson, D. C.; Keszler, D. A. *Solid State Sci.* **2011**.